Abstracts

Chapter 2: Photocatalytic turnover of CO_2 under visible light by Re(I) naphthalimide complexes in tandem with a sacrificial donor

Increased levels of atmospheric, anthropogenic CO_2 and rapid consumption of fossil fuels present major challenges for society and prompts the development of new potent catalysts that can absorb visible light to reduce greenhouse gasses[1,2]. The photocatalytic reduction of CO_2 using rhenium(I) has been demonstrated but suffers from low turnover. Herein, we describe a [$Re(CO)_3$(1-(1,10)phenanthroline-5-(4-nitro-naphthalimide))Cl] (**Re5-PAN**) photocatalyst, which when combined with the sacrificial donor 1,3-dimethyl-2-phenyl-2,3-dihydro-1*H*-benzo[*d*]imidazole, results in selective production of formic acid and a high turnover number of 533 and turnover frequency of 356 h^{-1}. Single-crystal X-ray diffraction and DFT studies are discussed as well as a preliminary look at a series of next-generation Re(I) catalysts with modified ligand conjugation.

Chapter 3: Synthesis, Characterization, and Imaging of Fluoroplatin: a Pro-drug for Fluorescence Detection of Aquated Cisplatin

Nausea and emesis are common side effects of cancer chemotherapy; however, their physiological origins and pathways are often unknown. Cisplatin has been used in chemotherapy since 1978 but the ability to track its localization and assay its transcriptional effects has been hampered by its lack of fluorescence. Herein, we synthesized and characterized a Pt (IV) pro-probe, 6,8-difluoro-7-hydroxy-4-methylcoumarin-cis-diamminehydroxyplatinum(IV)dichloro ester (**1**). In a reducing environment, **1** formed the aquated products of intracellular cisplatin, as evidenced by ^{1}H and ^{195}Pt NMR, IR, high resolution mass spectroscopy, and fluorescence spectroscopy. Live-cell imaging supported accumulation of the probe in the nucleus of HEK-293 cells at one hour. This pro-probe will allow for visual validation of cisplatin uptake in tissues, which can then be used for studies including single cell RNA sequencing transcriptomics to better understand the physiological pathways of cisplatin-induced side effects and/or function.

Chapter 4: Rapid, green disulfide bond formation in water using the corrin dicyanocobinamide

Peptide chemists seek rapid methods combined with facile purification when producing disulfide bonds post solid-phase synthesis. Current methods typically require long reaction times of up to two days, can result in side-products from over-oxidation and/or degradation, require organic solvents, and/or require challenging purification. Herein, we describe a rapid, green, and facile oxidation of a series of peptides with up to three disulfide bonds. The method was conducted in aqueous solution, in air, utilizing the biocompatible corrin ring-containing compound dicyanocobinamide, and offers reaction times under 1 hour with simple one step removal of the catalyst.

Small molecule and peptide redox reactions using rare and earth abundant metal complexes

by

Alyssa Spear

M.Phil., Syracuse University, 2021

B.S., Baldwin Wallace University, 2019

Dissertation

Submitted in partial fulfillment of the requirements for the degree of Doctor of Philosophy in Chemistry.

Syracuse University

June 2023

Table of Contents

List of Figures

List of Schemes

List of Tables

List of Abbreviations

5-HT_3	5-hydroxytryptamine 3
ACN	acetonitrile
ACN-d3	deuterated acetonitrile
AP	*area postrema*
AUC	area under the curve
AVP	vasopressin
B_{12}	vitamin B_{12}, cyanocobalamin
BIH	1,3-dimethyl-2-phenyl-2,3-dihydro-1H-benzo[d]imidazole
Cbi	dicyanocobinamide
CCK-8	Cell Counting Kit 8
CO_2RR	CO_2 reduction reaction
Cy-5	cyanine 5
DAPI	4’,6-diamidino-2-phenylindole
DCM	dichloromethane
DMEM	Dulbecco's Modified Eagle Medium
DMSO	dimethyl sulfoxide
DNA	deoxyribonucleic acid
ET-1	endothelin 1
FT-IR	Fourier transform infrared
GC	gas chromatography
GSH	glutathione
HBSS	Hank's Balanced Salt solution
HEK-293	human embryonic kidney cells
HEPES	N-2-hydroxyethylpiperazine-N'-2-ethanesulfonic acid
HRMS	high resolution mass spectrometry
NHS	*N*-hydroxysuccinimide
NMR	nuclear magnetic resonance

NTS	*nucleus tractus solitarius*
OT	modified oxytocin with an azido-lysine at position 8
PBS	phosphate buffered saline
RNA	ribonucleic acid
RP-HPLC	reverse-phase high performance liquid chromatography
snRNAseq	single nuclei RNA sequencing
SST	somatostatin
TDA	Tamm-Dancoff Approximation
TEA	triethylamine
TFA	trifluoroacetic acid
TMS	tetramethylsilane
TN	turnover number
TOF	turnover frequency
ToF	time of flight
UV	ultraviolet

Chapter 1. Introduction

1.1 Greenhouse gas: CO_2

Increased levels of atmospheric, anthropogenic CO_2 and rapid consumption of fossil fuels require the development of new technologies and strategies in the pursuit of sustainable energy and climate preservation. CO_2 is the major anthropogenic climate modifier with an abundance of 415.7 +/- 0.2 ppm versus a preindustrial abundance of 278.3 ppm[2]. The natural carbon cycle redistributes the emitted CO_2 into a variety of sinks such as terrestrial ecosystems and ocean carbon reservoirs. These sinks, however, are sensitive to changes in the atmospheric abundance such that any deliberate removal of CO_2 will be offset by outgassing from the sinks[1]. Moreover, the CO_2 removal processes (incorporation into forest biomass, circulation into the deep ocean, and silicate weathering) range in timescale from decades to millennia, making CO_2 a long-lived greenhouse gas whose accumulation is irreversible in human timescales[3]. Consequently, it is of the upmost importance to develop tools to accelerate the removal of CO_2 from the carbon cycle.

1.2 Metal catalysis are powerful CO_2 reducers

One strategy to tackle the large abundance of CO_2 is the use of metal catalysts to reductively convert the greenhouse gas into fuels and feedstocks, primarily CO[4,5]. The CO_2 reduction reaction (CO_2RR) can be executed by electrocatalytic or photocatalytic means. The source of electrons for these two processes differ with electrocatalysis deriving electrons from an external electric field and photocatalysis from photonic excitation. Consequently, photocatalytic systems require a photosensitizer either coordinated to the catalytic metal

center or homogenously dissolved in solution with the catalyst. Despite differences in electron source, both systems typically reduce CO_2 molecules into C_1 products, such as CO, methanol, and formate. CO_2 reduction into formate is a particularly appealing method for carbon utilization due to its ease of transportation and storage, high energy density, and as a favorable candidate for hydrogen storage[6,7].

1.2.1 Rhenium tricarbonyl scaffold

Despite interest in producing the liquid C_1 product, formate, it has been historically reported as an undesired side product in low to no yields in molecular homogenous rhenium(I) catalytic systems and prompted the development of a catalyst to fill this niche[8–14]. A rhenium tricarbonyl photocatalyst for CO_2RR was first reported in the form of $Re(bipy)(CO)_3Cl$ in 1983[15] (**Figure 1-1**). It was an improvement on prior work with $Ru(bipy)_3^{2+}/Co^{II}$ both in catalytic activity and as a single component system, $Re(bipy)(CO)_3Cl$ acting as both a photosensitizer and catalyst. The rhenium(I) tricarbonyl core is a useful framework for catalytic rhenium complexes, retaining a kinetically inert d^6 electron configuration and allowing mono-, bi-, and tridentate ligand binding modes. Chemical synthesis is facile from commercially available halidopentacarbonylrhenium(I) via a reflux in water to the air-stable triaquatricarbonylrhenium(I) precursor molecule[16,17].

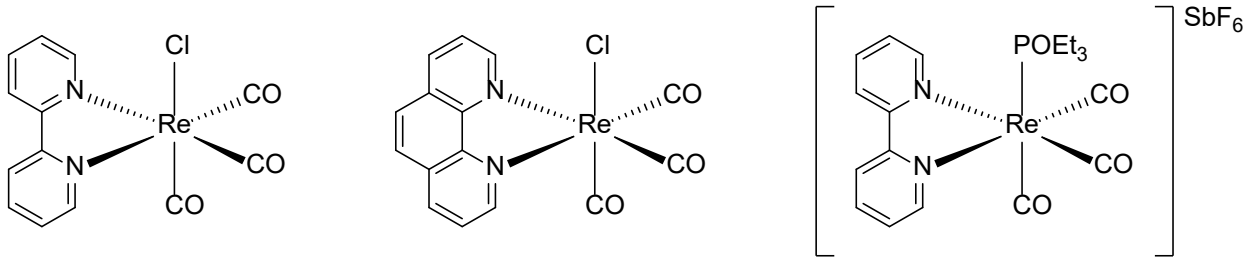

Figure 1-1. Early examples of $Re(CO)_3$ single component catalysts[15–17]

1.2.2 Homogenous versus heterogenous catalysts

Catalytic systems are often described as either heterogenous or homogeneous, each with advantages and disadvantages. Heterogenous systems typically house the catalyst in the solid phase and the substrate and product in the liquid phase while homogenous systems house all components in one phase, often the liquid phase. While heterogenous catalysis is favored in chemical industry due to ease of purification and catalyst recyclability, the low concentration and numerous types of active sites hinders development and molecular optimization of these systems. Conversely, the study of homogenous catalytic constructs allows for better definition of the active sites, obtaining structure-activity relationships, and ultimately the ability to describe a mechanism.

1.2.3 Solar photoactivation

A key requirement for the present catalytic system is activation by renewable electricity and/or solar energy. The most intense wavelength of visible light generated by the sun is blue light (~450 nm). Therefore, was ensured that the catalyst can absorb blue light by exciting the system with a blue UV lamp (LED, 12 W, 450-460 nm). Many photocatalytic rhenium molecular catalysts absorb in the UV range, making them inapt for translation as solar catalysts.

1.2.4 Sacrificial electron donors

Frequently in the above-mentioned systems, sacrificial electron donors are needed to regenerate the catalyst and turnover the cycle. Commonly, triethylamine (TEA) and triethanolamine (TEOA) are added to the main reaction solvent or serve as the main reaction solvent themselves. Interestingly, TEA not only serves as an electron donor, but a hydrogen donor and the mechanism of formate production via hydrogen atom transfer and CO_2 insertion into the metal hydride has been described[18]. 1,3-dimethyl-2-phenyl-2,3-dihydro-1H-benzo[d]imidazole (BIH) has also been utilized as a sacrificial electron donor in photocatalytic systems due to its strong reductive activity[19]. BIH was synthesized and employed as a two electron, one hydrogen donor comparatively to the classic TEA.

1.2.5 Turnover numbers and frequencies

One metric used to compare the activity and efficiency of these catalytic systems is by calculating turnover numbers (TN) and frequencies (TOF) defined by the equations below.

$$TN = \frac{[CO_2 \text{ reduction product}]}{[\text{Catalyst}]}$$

$$TOF = \frac{TN}{\text{time}}$$

1.2.6 Inconsistencies in experimental conditions and reporting

The literary body on homogenous catalysis is quite inconsistent in terms of comparative or descriptive details regarding catalyst concentration, substrate concentration, reaction volume, reaction time, stirring, heat, light source, wattage, distance from target, and other

parameters can influence TN and TOF; consequently, all such parameters are described throughout this work.

1.3 Rhenium tricarbonyl scaffold requires tuning for selectivity

Since the development of the first single-component rhenium (I) tricarbonyl photocatalyst, the photosensitizing ligand has been expanded on to improve on various facets of catalytic activity. The fluorochromes notably act as electron acceptors after excitation and subsequent metal to ligand charge transfer (MLCT). An enhanced ability to delocalize the excited electron not only expands light absorptivities farther in to the red but increases the excited-state lifetime of the catalytic species[20]. Conjugated ligands offer a range of excitation and emission profiles as well as reduction potentials depending on the degree of conjugation and donor strength of substituents[21,22]. Considering the reduction potentials required for various reduced CO_2 products may also guide catalyst tuning towards selectivity, in this case, towards formate/formic acid (**Table 1-1**).

Table 1-1. CO_2 Reduction Potentials[4]

Reaction	$E^{\circ\prime}$ (V) vs SCE[a]
$CO_2 + 2H^+ + 2e^- \rightarrow HCO_2H$	-0.85
$CO_2 + 2H^+ + 2e^- \rightarrow CO + H_2O$	-0.77

[a] $E^{\circ\prime}$ potentials are reported at pH 7.

1.4 Naphthalimide photosensitizing ligands

The naphthalimide fluorophore has been utilized in a variety of contexts as a photosensitizer capable of participating in photoinduced electron transfer (PET) and multiple electron transfer (MET) processes[23]. Naphthalimide derivatives are well reported with modifications at both the imide and 4-position of the naphthalene with recent applications as DNA "light switches"[24] and GSH fluorescent probes[25]. The following ligands incorporate naphthalimide to aid the rhenium center in catalysis.

1.4.1 1-(1,10)-phenanthroline-5-(4-nitro-naphthalimide) (5-PAN)

5-PAN utilizes 1,10-phenanthroline to tether the naphthalimide to the rhenium center while also preserving conjugation throughout the ligand (**Figure 1-2**). The phenanthroline provides two donor sites for coordination thus enhancing the chelate effect and the complex stability. The 4-position of the naphthalimide incorporates a nitro group as an electron withdrawing group.

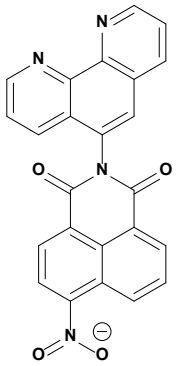

Figure 1-2. Structure of 1-(1,10)-phenanthroline-5-(4-nitro-naphthalimide)

1.5 Cisplatin activity and structure

Cis-diaminedichloroplatinum (II), or cisplatin, has been used as a chemotherapeutic agent since its approval by the U.S. Food and Drug Administration in 1978. The mechanism of action of cisplatin upon cellular uptake is triggered by the lower intercellular concentration of chloride (~4-12 mM) relative to bloodstream (~100 mM), which results in hydrolysis of cisplatin into a variety of partially and fully hydrolyzed species that can crosslink with DNA, preferentially at N_7 of purine bases[26–28]. The binding of cisplatin into DNA leads to recruitment of repair machinery, but ultimately the DNA damage may initiate oxidative stress and pro-apoptotic pathways[27,29,30]. A host of analogs, probes, and pro-drugs have been developed in recent years to improve cellular uptake, solubility, half-life, target selectivity, as well as to introduce fluorescent tags and co-drug delivery[31–38]. Herein, we aim to utilize a Pt(IV) based complex with bound fluorophore to address a lack of knowledge of the physiological pathways of common side effects of chemotherapy, specifically nausea and emesis, that are linked to areas of the hindbrain, namely, the *area postrema* (AP) and *nucleus tractus solitarius* (NTS).

1.6 Cisplatin-induced nausea and emesis

While the signal cascade of emesis is well researched[39], cell type-specific patterns of gene expression associated with cisplatin-induced emesis have not been described. 5-hydroxytryptamine$_3$ (5-HT_3) receptor antagonists, a class of drug known as 'setrons', have been studied as anti-emetic drugs for chemotherapy, however patients still experience acute and chronic nausea, a process that has yet to be understood and clinically addressed[40,41]. These side effects, amongst others (*i.e.*, malaise, cardiotoxicity, hepatotoxicity) are understudied in terms

of gene expression and reduce quality of life and maximum tolerated dose of treatment[42]. Therefore, there is a need to uncover these pathways, for example by unearthing differentially expressed genes (DEGs) in the AP-NTS as a first step in understanding cisplatin-induced nausea and emesis.

In Chapter 3, the synthesis and characterization of a Pt(IV) pro-probe, 6,8-difluoro-7-hydroxy-4-methylcoumarin-cis-diamminehydroxyplatinum(IV)dichloro ester (**1**) is reported. For the purpose of real-time imaging and assessing cellular uptake, the blue emitting coumarin-based fluorophore was introduced at a Pt(IV) axial position (**Scheme 3-1**). Finally, cellular uptake and cytotoxicity was assessed, and the applicability of **1** as a tool for verifying localization in specific cells *in vivo* and *ex vivo* was explored.

1.7 Solid phase peptide synthesis

1.7.1 Disulfide bonds are essential for peptide structure and activity

Solid-phase peptide synthesis (SPPS) is an indispensable tool for chemists to produce milligram to gram scale amounts of peptides and study their structure-activity relationships (SARs) to generate derivatives or analogues for new targeted therapeutics[43]. Select multi-cysteine containing peptides require an extra synthetic step to achieve final three-dimensional structure, which influences their biological function and/or stability[44–46]. The oxidation of a pair of cysteine residues to form a cystine produces a covalent bond and decreases the configurational entropy of the folded peptide. This process can be achieved via air oxidation[47], use of dimethyl sulfoxide (DMSO)[48], hydrogen peroxide[49], iodine[50], or ferricyanide[51], to name a few[44,52,53]. Many of the methods, however, require long reaction times, produce dimers, involve

environmentally harmful organic solvents (which also limit hydrophilic peptide solubility), or result in modification of sensitive amino acid side chains (Tyr, Met, or Trp)[54,55].

1.7.2 Limitations of DMSO

Within our own lab we have frequently required an aqueous based method to produce correct disulfide bonds post-SPPS, one that also allows facile purification. We have routinely used 10% aqueous DMSO but aim to move away from the polar aprotic solvent, which has slow reaction times and is not amenable to translation from in vitro to in vivo work in many pharmaceutical environments. Though DMSO has been used ubiquitously as a solvent for small hydrophobic drugs and as a control vehicle for a variety of biomedical studies, questions have been called on the suitability of the solvent in these contexts. DMSO has been reported to be cytotoxic at low doses (2-5%) in rat retinas[56], alter behavior in aquatic species[57], and inactivate platinum-based drugs[58]. It may also mask solubility issues that manifest when moving into saline or buffered aqueous solutions when moving to *in vivo* studies.

1.8 Cyanocobalamin and dicyanocobinamide

Cobinamide is a commercially available cobalamin (vitamin B_{12}) precursor shown in **Figure 1-3**. The truncated species dicyanocobinamide (Cbi) was explored for catalytic disulfide bond formation in peptides.

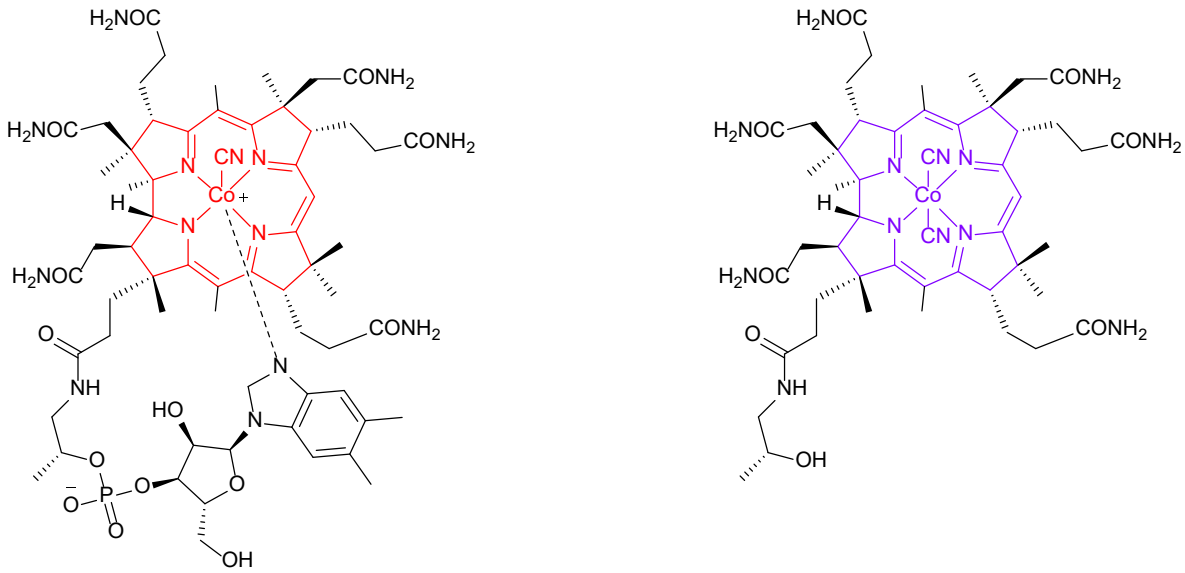

Figure 1-3. Cyanocobalamin (left) and dicyanocobinamide (right)

1.8.1 Structure

The structure of B_{12} incorporates a cobalt metal center, a conjugated corrin ring involving 14 π electrons, and a nucleotide loop containing a α-D-ribofuranose-3-phosphate and terminal 2,3-dimethylbenzimidazole (DMBZ) that can axially coordinate to the Co. Conversely, Cbi lacks the nucleotide and both axial positions are occupied by cyano ligands resulting in an altered ligand environment and purple color.

1.8.2 Reactivity

The cobalt center of B_{12} can access three oxidation states giving rise to electrophilic, radical, and nucleophilic behavior each with different ligand-accepting capabilities and reduction potentials with influence from its 2,3-dimethylbenzimidazole base-on/-off forms[59] and modification to the corrin macrocycle[60]. A number of excellent reviews and perspectives are available on B_{12} chemistry[61–66], with recent interest in applications ranging from

dicarbofunctionalization of bromoalkenes[67] to transition metal analogues for the study of B_{12}-dependant processes[68] to regioselective ring opening of epoxides[69]. In contrast, we have a limited understanding of Cbi, which has been primarily studied as an antidote for cyanide poisoning[70–73] or as a scavenger for other poisons like methyl mercaptan[74] or hydrogen sulphide[75]. Over the course of the 1960s to 1980s, cobalamins and cobinamides were shown to oxidize simple thiols such as 2-mercaptoethanol and dithioerythritol. Of note was the observation that Cbi catalysed the aerobic oxidation orders of magnitude faster than B_{12} (191 and 0.003 s^{-1}, respectively)[76]. Despite these long-known reports, no one has developed a method for disulfide bond oxidation via Cbi to prepare functional peptides.

1.9 Disulfide bond formation in peptides catalyzed by Cbi

The peptides used in Chapter 4 have a mix of lengths and amounts of cysteines so as to test the versatility of Cbi catalysis of disulfide oxidation (**Figure 1-4**). Regioselectivity of disulfide bonding in cysteine-rich peptides presents a challenge for oxidation methods due to the possibility of scrambling and subsequent misfolding. Herein, the utilization of Cbi to catalyze the air-oxidation of the peptides is described with fast reaction times, in water, with facile purification, and with discussion of regioselectivity.

Oxytocin (**OT**)	CYIQNCPK*G-NH_2
Vasopressin (**AVP**)	CYFQNCPRG-NH_2
Somatostatin (**SST**)	AGCKNFFWKTFTSC-NH_2
Endothelin 1 (**ET-1**)	CSCSSLMDKECVYFCHLDIIW-NH_2
***Tr*CART-1**	IPRCDVGERCALKHGPRIG-NH_2
***Tr*CART-2**	IPRCDVGERCALKHGPRIGRLCDCL-NH_2
***Tr*CART-3**	IPRCDVGERCALKHGPRIGRLCDCLRGAACNTFFLRCL-NH_2

Figure 1-4. The sequences and disulfide bond connections of peptides screened (K* = azido lysine).

1.10 References

(1) IPCC. *Climate Change 2021: The Physical Science Basis. Contribution of Working Group I to the Sixth Assessment Report of the Intergovernmental Panel on Climate Change*; Masson-Delmotte, V., P. Zhai, A. Pirani, S.L. Connors, C. Péan, S. Berger, N. Caud, Y. Chen, L. Goldfarb, M.I. Gomis, M. Huang, K. Leitzell, E. Lonnoy, J. B. R., Matthews, T.K. Maycock, T. Waterfield, O. Yelekçi, R. Yu, and B. Z., Eds.; Cambridge University Press: Cambridge, UK and New York, NY, USA, 2021. https://doi.org/10.1017/9781009157896.

(2) WMO. *Greenhouse Gas Bulletin: The State of Greenhouse Gases in the Atmosphere Based on Global Observations through 2021*; 2021.

(3) IPCC. *Global Warming of 1.5°C. An IPCC Special Report on the Impacts of Global Warming of 1.5°C above Pre-Industrial Levels and Related Global Greenhouse Gas Emission Pathways, in the Context of Strengthening the Global Response to the Threat of Climate*

Change,; Masson-Delmotte, V., P. Zhai, H.-O. Pörtner, D. Roberts, J. Skea, P.R. Shukla, A. P., W. Moufouma-Okia, C. Péan, R. Pidcock, S. Connors, J.B.R. Matthews, Y. Chen, X. Zhou, M.I. Gomis, E. Lonnoy, T. Maycock, M. Tignor, and T., Waterfield, Eds.; Cambridge University Press: Cambridge, UK and New York, NY, USA, 2018. https://doi.org/10.1017/9781009157940.

(4) Morris, A. J.; Meyer, G. J.; Fujita, E. Molecular Approaches to the Photocatalytic Reduction of Carbon Dioxide for Solar Fuels. *Acc. Chem. Res.* **2009**, *42* (12), 1983–1994. https://doi.org/10.1021/ar9001679.

(5) Takeda, H.; Ishitani, O. Development of Efficient Photocatalytic Systems for CO2 Reduction Using Mononuclear and Multinuclear Metal Complexes Based on Mechanistic Studies. *Coord. Chem. Rev.* **2010**, *254* (3–4), 346–354. https://doi.org/10.1016/j.ccr.2009.09.030.

(6) Mellmann, D.; Sponholz, P.; Junge, H.; Beller, M. Formic Acid as a Hydrogen Storage Material-Development of Homogeneous Catalysts for Selective Hydrogen Release. *Chemical Society Reviews*. Chem Soc Rev July 21, 2016, pp 3954–3988. https://doi.org/10.1039/c5cs00618j.

(7) Eppinger, J.; Huang, K. W. Formic Acid as a Hydrogen Energy Carrier. *ACS Energy Lett.* **2017**, *2* (1), 188–195. https://doi.org/10.1021/ACSENERGYLETT.6B00574.

(8) Rotundo, L.; Grills, D. C.; Gobetto, R.; Priola, E.; Nervi, C.; Polyansky, D. E.; Fujita, E. Photochemical CO 2 Reduction Using Rhenium(I) Tricarbonyl Complexes with Bipyridyl-Type Ligands with and without Second Coordination Sphere Effects.

ChemPhotoChem **2021**, *5* (6), 526–537. https://doi.org/10.1002/cptc.202000307.

(9) Takeda, H.; Koike, K.; Inoue, H.; Ishitani, O. Development of an Efficient Photocatalytic System for CO2 Reduction Using Rhenium(I) Complexes Based on Mechanistic Studies. *J. Am. Chem. Soc.* **2008**, *130* (6), 2023–2031. https://doi.org/10.1021/ja077752e.

(10) Koike, K.; Hori, H.; Ishizuka, M.; Westwell, J. R.; Takeuchi, K.; Ibusuki, T.; Enjouji, K.; Konno, H.; Sakamoto, K.; Ishitani, O. Key Process of the Photocatalytic Reduction of CO2 Using [Re(4,4'-X2-Bipyridine)(CO)3PR3] + (X = CH3, H, CF3; PR3 = Phosphorus Ligands): Dark Reaction of the One-Electron-Reduced Complexes with CO2. *Organometallics* **1997**, *16* (26), 5724–5729. https://doi.org/10.1021/om970608p.

(11) Shakeri, J.; Farrokhpour, H.; Hadadzadeh, H.; Joshaghani, M. Photoreduction of CO2 to CO by a Mononuclear Re(i) Complex and DFT Evaluation of the Photocatalytic Mechanism. *RSC Adv.* **2015**, *5* (51), 41125–41134. https://doi.org/10.1039/c5ra02002f.

(12) Liang, H.-P.; Acharjya, A.; Anito, D. A.; Vogl, S.; Wang, T.-X.; Thomas, A.; Han, B.-H. Rhenium-Metalated Polypyridine-Based Porous Polycarbazoles for Visible-Light CO 2 Photoreduction. *ACS Catal.* **2019**, *9* (5), 3959–3968. https://doi.org/10.1021/acscatal.8b04032.

(13) Morimoto, T.; Nakajima, T.; Sawa, S.; Nakanishi, R.; Imori, D.; Ishitani, O. CO 2 Capture by a Rhenium(I) Complex with the Aid of Triethanolamine. *J. Am. Chem. Soc.* **2013**, *135* (45), 16825–16828. https://doi.org/10.1021/ja409271s.

(14) Hawecker, J.; Lehn, J.; Ziessel, R. Photochemical and Electrochemical Reduction of

Carbon Dioxide to Carbon Monoxide Mediated by (2,2?-Bipyridine)Tricarbonylchlororhenium(I) and Related Complexes as Homogeneous Catalysts. *Helv. Chim. Acta* **1986**, *69* (8), 1990–2012. https://doi.org/10.1002/hlca.19860690824.

(15) Hawecker, J.; Lehn, J.-M.; Ziessel, R. Efficient Photochemical Reduction of CO 2 to CO by Visible Light Irradiation of Systems Containing Re(Bipy)(CO) 3 X or Ru(Bipy) 3 2+ –Co 2+ Combinations as Homogeneous Catalysts. *J. Chem. Soc., Chem. Commun.* **1983**, No. 9, 536–538. https://doi.org/10.1039/C39830000536.

(16) Wei, L.; Banerjee, S. R.; Levadala, M. K.; Babich, J.; Zubieta, J. Complexes of the Fac-{Re(CO)3}+ Core with Tridentate Ligands Derived from Arylpiperazines. *Inorganica Chim. Acta* **2004**, *357* (5), 1499–1516. https://doi.org/10.1016/j.ica.2003.11.027.

(17) Lazarova, N.; James, S.; Babich, J.; Zubieta, J. A Convenient Synthesis, Chemical Characterization and Reactivity of [Re(CO) 3(H 2O) 3]Br: The Crystal and Molecular Structure of [Re(CO) 3(CH 3CN) 2Br]. *Inorg. Chem. Commun.* **2004**, *7* (9), 1023–1026. https://doi.org/10.1016/j.inoche.2004.07.006.

(18) Agarwal, J.; Johnson, R. P.; Li, G. Reduction of CO 2 on a Tricarbonyl Rhenium(I) Complex: Modeling a Catalytic Cycle. *J. Phys. Chem. A* **2011**, *115* (13), 2877–2881. https://doi.org/10.1021/jp111342r.

(19) Tamaki, Y.; Koike, K.; Morimoto, T.; Ishitani, O. Substantial Improvement in the Efficiency and Durability of a Photocatalyst for Carbon Dioxide Reduction Using a Benzoimidazole Derivative as an Electron Donor. *J. Catal.* **2013**, *304*, 22–28.

https://doi.org/10.1016/j.jcat.2013.04.002.

(20) Boyde, S.; Strouse, G. F.; Jones, W. E.; Meyer, T. J. The Effect on MLCT Excited States of Electronic Delocalization in the Acceptor Ligand. *J. Am. Chem. Soc.* **1990**, *112* (20), 7395–7396. https://doi.org/10.1021/ja00176a049.

(21) Ashley, D. C.; Jakubikova, E. Tuning the Redox Potentials and Ligand Field Strength of Fe(II) Polypyridines: The Dual π-Donor and π-Acceptor Character of Bipyridine. *Inorg. Chem.* **2018**, *57* (16), 9907–9917. https://doi.org/10.1021/acs.inorgchem.8b01002.

(22) Anjali, B. A.; Suresh, C. H. Electronic Effect of Ligands: Vs. Reduction Potentials of Fischer Carbene Complexes of Chromium: A Molecular Electrostatic Potential Analysis. *New J. Chem.* **2018**, *42* (22), 18217–18224. https://doi.org/10.1039/c8nj04184a.

(23) Koper, M. T. M. Theory of Multiple Proton-Electron Transfer Reactions and Its Implications for Electrocatalysis. *Chem. Sci.* **2013**, *4* (7), 2710–2723. https://doi.org/10.1039/c3sc50205h.

(24) Ryan, G. J.; Gunnlaugsson, T.; Quinn, S. J. Hook, Line, and Sinker! Spectroscopic Studies of Bi-Modular Mono- and Bis-1,8-Naphthalimide-Ru(Bpy)3-Conjugates as DNA “Light Switches.” *Inorg. Chem.* **2022**, *61* (31), 12073–12086. https://doi.org/10.1021/acs.inorgchem.2c00064.

(25) Zhang, F.; Chen, F.; Shen, R.; Chen, Y. X.; Zhao, Z.; Zhang, B.; Fang, J. Naphthalimide Fluorescent Skeleton for Facile and Accurate Quantification of Glutathione. *Anal. Chem.* **2023**, *95* (9), 4301–4309. https://doi.org/10.1021/acs.analchem.2c04098.

(26) Jung, Y.; Lippard, S. J. Direct Cellular Responses to Platinum-Induced DNA Damage. *Chem. Rev.* **2007**, *107* (5), 1387–1407. https://doi.org/10.1021/cr068207j.

(27) Pinto, A. L.; Lippard, S. J. Binding of the Antitumor Drug Cis-Diamminedichloroplatinum(II) (Cisplatin) to DNA. *Biochim. Biophys. Acta - Rev. Cancer* **1985**, *780* (3), 167–180. https://doi.org/10.1016/0304-419X(85)90001-0.

(28) Baik, M.-H.; Friesner, R. A.; Lippard, S. J. Theoretical Study of Cisplatin Binding to Purine Bases: Why Does Cisplatin Prefer Guanine over Adenine? *J. Am. Chem. Soc.* **2003**, *125* (46), 14082–14092. https://doi.org/10.1021/ja036960d.

(29) Roberts, J. J.; Thomson, A. J. The Mechanism of Action of Antitumor Platinum Compounds. *Prog. Nucleic Acid Res. Mol. Biol.* **1979**, *22* (C), 71–133. https://doi.org/10.1016/S0079-6603(08)60799-0.

(30) Eastman, A. The Formation, Isolation and Characterization of DNA Adducts Produced by Anticancer Platinum Complexes. *Pharmacol. Ther.* **1987**, *34* (2), 155–166. https://doi.org/10.1016/0163-7258(87)90009-X.

(31) Johnstone, T. C.; Suntharalingam, K.; Lippard, S. J.; C. Johnstone, T.; Suntharalingam, K.; J. Lippard, S.; Johnstone, T. C.; Suntharalingam, K.; Lippard, S. J.; C. Johnstone, T.; et al. The Next Generation of Platinum Drugs: Targeted Pt(II) Agents, Nanoparticle Delivery, and Pt(IV) Prodrugs. *Chem. Rev.* **2016**, *116* (5), 3436–3486. https://doi.org/10.1021/acs.chemrev.5b00597.

(32) Lee, V. E. Y.; Lim, Z. C.; Chew, S. L.; Ang, W. H. Strategy for Traceless Codrug Delivery with

Platinum(IV) Prodrug Complexes Using Self-Immolative Linkers. *Inorg. Chem.* **2021**, *60* (3), 1823–1831. https://doi.org/10.1021/acs.inorgchem.0c03299.

(33) Pathak, R. K.; Marrache, S.; Choi, J. H.; Berding, T. B.; Dhar, S. The Prodrug Platin- A : Simultaneous Release of Cisplatin and Aspirin. *Angew. Chemie* **2014**, *126* (7), 1994–1998. https://doi.org/10.1002/ange.201308899.

(34) Spector, D. V; Pavlov, K. G.; Akasov, R. A.; Vaneev, A. N.; Erofeev, A. S.; Gorelkin, P. V; Nikitina, V. N.; Lopatukhina, E. V; Semkina, A. S.; Vlasova, K. Y.; et al. Pt(IV) Prodrugs with Non-Steroidal Anti-Inflammatory Drugs in the Axial Position. *J. Med. Chem.* **2022**, *2022*, 8244. https://doi.org/10.1021/acs.jmedchem.1c02136.

(35) Chu, Y.-H.; Sibrian-Vazquez, M.; Escobedo, J. O.; Phillips, A. R.; Dickey, D. T.; Wang, Q.; Ralle, M.; Steyger, P. S.; Strongin, R. M. Systemic Delivery and Biodistribution of Cisplatin in Vivo. *Mol. Pharm.* **2016**, *13* (8), 2677–2682. https://doi.org/10.1021/acs.molpharmaceut.6b00240.

(36) Spector, D. V.; Erofeev, A. S.; Gorelkin, P. V.; Vaneev, A. N.; Akasov, R. A.; Ul'Yanovskiy, N. V.; Nikitina, V. N.; Semkina, A. S.; Vlasova, K. Y.; Soldatov, M. A.; et al. Electrochemical Detection of a Novel Pt(IV) Prodrug with the Metronidazole Axial Ligand in the Hypoxic Area. *Inorg. Chem.* **2022**, *61* (37), 14705–14717. https://doi.org/10.1021/acs.inorgchem.2c02062.

(37) Khoury, A.; Sakoff, J. A.; Gilbert, J.; Scott, K. F.; Karan, S.; Gordon, C. P.; Aldrich-Wright, J. R. Cyclooxygenase-Inhibiting Platinum(IV) Prodrugs with Potent Anticancer Activity. *Pharmaceutics* **2022**, *14* (4), 787. https://doi.org/10.3390/pharmaceutics14040787.

(38) Chen, Y.; Wang, Q.; Li, Z.; Liu, Z.; Zhao, Y.; Zhang, J.; Liu, M.; Wang, Z.; Li, D.; Han, J. Naproxen Platinum(<scp>iv</Scp>) Hybrids Inhibiting Cycloxygenases and Matrix Metalloproteinases and Causing DNA Damage: Synthesis and Biological Evaluation as Antitumor Agents *in Vitro* and *in Vivo*. *Dalt. Trans.* **2020**, *49* (16), 5192–5204. https://doi.org/10.1039/D0DT00424C.

(39) Andrews, P. L. R.; Horn, C. C. Signals for Nausea and Emesis: Implications for Models of Upper Gastrointestinal Diseases. *Auton. Neurosci.* **2006**, *125* (1–2), 100–115. https://doi.org/10.1016/j.autneu.2006.01.008.

(40) Herrington, J. D.; Kwan, P.; Young, R. R.; Lagow, E.; Lagrone, L.; Riggs, M. W. Randomized, Multicenter Comparison of Oral Granisetron and Oral Ondansetron for Emetogenic Chemotherapy. *Pharmacotherapy* **2000**, *20* (11), 1318–1323. https://doi.org/10.1592/phco.20.17.1318.34894.

(41) Morrow, G. R.; Andrews, P. L. R.; Hickok, J. T.; Stern, R. Vagal Changes Following Cancer Chemotherapy: Implications for the Development of Nausea. *Psychophysiology* **2000**, *37* (3), 378–384. https://doi.org/10.1111/1469-8986.3730378.

(42) Florea, A.-M.; Büsselberg, D. Cisplatin as an Anti-Tumor Drug: Cellular Mechanisms of Activity, Drug Resistance and Induced Side Effects. *Cancers (Basel).* **2011**, *3* (1), 1351–1371. https://doi.org/10.3390/cancers3011351.

(43) Góngora-Benítez, M.; Tulla-Puche, J.; Albericio, F. Multifaceted Roles of Disulfide Bonds. Peptides as Therapeutics. *Chem. Rev.* **2014**, *114* (2), 901–926. https://doi.org/10.1021/cr400031z.

(44) Fass, D.; Thorpe, C. Chemistry and Enzymology of Disulfide Cross-Linking in Proteins. *Chem. Rev.* **2018**, *118* (3), 1169–1198. https://doi.org/10.1021/ACS.CHEMREV.7B00123.

(45) Habermann, E. Apamin. *Pharmacol. Ther.* **1984**, *25* (2), 255–270. https://doi.org/10.1016/0163-7258(84)90046-9.

(46) Hoover, D. M.; Chertov, O.; Lubkowski, J. The Structure of Human β-Defensin-1. *J. Biol. Chem.* **2001**, *276* (42), 39021–39026. https://doi.org/10.1074/jbc.M103830200.

(47) Sandberg, B. E. B.; Ragnarsson, U. SOLID PHASE SYNTHESIS OF APAMIN, THE PRINCIPAL NEUROTOXIN IN BEE VENOM*. *Int. J. Pept. Protein Res.* **2009**, *11* (3), 238–245. https://doi.org/10.1111/j.1399-3011.1978.tb02844.x.

(48) Tam, J. P.; Wu, C.-R.; Liu, W.; Zhang, J.-W. Disulfide Bond Formation in Peptides by Dimethyl Sulfoxide. Scope and Applications. *J. Am. Chem. Soc* **1991**, *113*, 6657–6662.

(49) Sidorova, M. V.; Molokoedov, A. S.; Az'muko, A. A.; Kudryavtseva, E. V.; Krause, E.; Ovchinnikov, M. V.; Bespalova, Z. D. The Use of Hydrogen Peroxide for Closing Disulfide Bridges in Peptides. *Russ. J. Bioorganic Chem.* **2004**, *30* (2), 101–110. https://doi.org/10.1023/B:RUBI.0000023093.05123.31.

(50) Reddy, K. M. B.; Kumari, Y. B.; Mallikharjunasarma, D.; Bulliraju, K.; Sreelatha, V.; Ananda, K. Large Scale Solid Phase Synthesis of Peptide Drugs: Use of Commercial Anion Exchange Resin as Quenching Agent for Removal of Iodine during Disulphide Bond Formation. *Int. J. Pept.* **2012**, *2012*, 1–8. https://doi.org/10.1155/2012/323907.

(51) Moore, G. Influence of the Peptide-Chain Length on Disulphide-Bond Formation in

Neurohypophysial Hormones and Analogues. *Biochem. J.* **1978**, *173* (2), 403–409. https://doi.org/10.1042/bj1730403.

(52) Laps, S.; Satish, G.; Brik, A. Harnessing the Power of Transition Metals in Solid-Phase Peptide Synthesis and Key Steps in the (Semi)Synthesis of Proteins. *Chem. Soc. Rev.* **2021**, *50* (4), 2367–2387. https://doi.org/10.1039/D0CS01156H.

(53) He, R.; Pan, J.; Mayer, J. P.; Liu, F. Stepwise Construction of Disulfides in Peptides. *ChemBioChem* **2020**, *21* (8), 1101–1111. https://doi.org/10.1002/cbic.201900717.

(54) Shi, T.; Berglund, J.; Elding, L. I. Reduction of Trans-Dichloro- and Trans-Dibromo-Tetracyanoplatinate(IV) by L-Methionine. *J. Chem. Soc. Dalt. Trans.* **1997**, *49* (12), 2073–2078. https://doi.org/10.1039/a608507e.

(55) Ma, D.; Sun, J.; Shen, S.; Chen, H.; Xu, W.; Wang, Y.; Song, C.; Shi, T.; Huo, S. Deprotection of S-Acetamidomethyl and 1,3-Thiazolidine-4-Carbonyl Protecting Groups from Cysteine Side Chains in Peptides by Trans -[PtX 2 (CN) 4] 2– : One-Pot Regioselective Synthesis of Disulfide Bonds. *J. Org. Chem.* **2022**, *87* (2), 1470–1476. https://doi.org/10.1021/acs.joc.1c02793.

(56) Galvao, J.; Davis, B.; Tilley, M.; Normando, E.; Duchen, M. R.; Cordeiro, M. F. Unexpected Low-dose Toxicity of the Universal Solvent DMSO. *FASEB J.* **2014**, *28* (3), 1317–1330. https://doi.org/10.1096/fj.13-235440.

(57) Huang, Y.; Cartlidge, R.; Walpitagama, M.; Kaslin, J.; Campana, O.; Wlodkowic, D. Unsuitable Use of DMSO for Assessing Behavioral Endpoints in Aquatic Model Species.

Sci. Total Environ. **2018**, *615*, 107–114. https://doi.org/10.1016/j.scitotenv.2017.09.260.

(58) Hall, M. D.; Telma, K. A.; Chang, K.-E.; Lee, T. D.; Madigan, J. P.; Lloyd, J. R.; Goldlust, I. S.; Hoeschele, J. D.; Gottesman, M. M. Say No to DMSO: Dimethylsulfoxide Inactivates Cisplatin, Carboplatin, and Other Platinum Complexes. *Cancer Res.* **2014**, *74* (14), 3913–3922. https://doi.org/10.1158/0008-5472.CAN-14-0247.

(59) Lexa, D.; Saveant, J. M. Electrochemistry of Vitamin B12. I. Role of the Base-on/Base-off Reaction in the Oxidoreduction Mechanism of the B12r-B12s System. *J. Am. Chem. Soc.* **1976**, *98* (9), 2652–2658. https://doi.org/10.1021/ja00425a039.

(60) Brenig, C.; Mosberger, L.; Baumann, K.; Blacque, O.; Zelder, F. Redox-Neutral Syntheses and Electrochemical Studies of 10-Bromo-Substituted Light-Stable Antivitamin B 12 Candidates. *Helv. Chim. Acta* **2021**, *104* (8), 26–28. https://doi.org/10.1002/hlca.202100067.

(61) Wdowik, T.; Gryko, D. C–C Bond Forming Reactions Enabled by Vitamin B 12 –Opportunities and Challenges. *ACS Catal.* **2022**, *12* (11), 6517–6531. https://doi.org/10.1021/acscatal.2c01596.

(62) Shimakoshi, H.; Hisaeda, Y. Electrochemistry and Catalytic Properties of Vitamin B12 Derivatives in Nonaqueous Media. *Curr. Opin. Electrochem.* **2018**, *8*, 24–30. https://doi.org/10.1016/J.COELEC.2017.12.001.

(63) Tahara, K.; Pan, L.; Ono, T.; Hisaeda, Y. Learning from B12 Enzymes: Biomimetic and Bioinspired Catalysts for Eco-Friendly Organic Synthesis. *Beilstein J. Org. Chem. 14232*

2018, *14* (1), 2553–2567. https://doi.org/10.3762/BJOC.14.232.

(64) Zelder, F. Modified Vitamin B12 Derivatives with a Peptide Backbone for Biomimetic Studies and Medicinal Applications. *J. Porphyr. Phthalocyanines* **2018**, *22* (07), 535–541. https://doi.org/10.1142/S108842461830001X.

(65) Dereven'kov, I. A.; Salnikov, D. S.; Silaghi-Dumitrescu, R.; Makarov, S. V.; Koifman, O. I. Redox Chemistry of Cobalamin and Its Derivatives. *Coord. Chem. Rev.* **2016**, *309*, 68–83. https://doi.org/10.1016/j.ccr.2015.11.001.

(66) Giedyk, M.; Goliszewska, K.; Gryko, D. Vitamin B 12 Catalysed Reactions. *Chem. Soc. Rev.* **2015**, *44* (11), 3391–3404. https://doi.org/10.1039/C5CS00165J.

(67) Smoleń, S.; Wincenciuk, A.; Drapała, O.; Gryko, D. Vitamin B12-Catalyzed Dicarbofunctionalization of Bromoalkenes Under Visible Light Irradiation. *Synthesis (Stuttg).* **2021**, *53* (09), 1645–1653. https://doi.org/10.1055/s-0040-1706602.

(68) Kieninger, C.; Wurst, K.; Podewitz, M.; Stanley, M.; Deery, E.; Lawrence, A. D.; Liedl, K. R.; Warren, M. J.; Kräutler, B. Replacement of the Cobalt Center of Vitamin B12 by Nickel: Nibalamin and Nibyric Acid Prepared from Metal-Free B12 Ligands Hydrogenobalamin and Hydrogenobyric Acid. *Angew. Chemie - Int. Ed.* **2020**, *59* (45), 20129–20136. https://doi.org/10.1002/ANIE.202008407.

(69) Potrząsaj, A.; Musiejuk, M.; Chaładaj, W.; Giedyk, M.; Gryko, D. Cobalt Catalyst Determines Regioselectivity in Ring Opening of Epoxides with Aryl Halides. *Cite This J. Am. Chem. Soc* **2021**, *143*, 9368–9376. https://doi.org/10.1021/jacs.1c00659.

(70) Broderick, K. E.; Potluri, P.; Zhuang, S.; Scheffler, I. E.; Sharma, V. S.; Pilz, R. B.; Boss, G. R. Cyanide Detoxification by the Cobalamin Precursor Cobinamide. *Exp. Biol. Med.* **2006**, *231* (5), 641–649. https://doi.org/10.1177/153537020623100519.

(71) Broderick, K. E.; Balasubramanian, M.; Chan, A.; Potluri, P.; Feala, J.; Belke, D. D.; McCulloch, A.; Sharma, V. S.; Pilz, R. B.; Bigby, T. D.; et al. The Cobalamin Precursor Cobinamide Detoxifies Nitroprusside-Generated Cyanide. *Exp. Biol. Med.* **2007**, *232* (6), 789–798.

(72) Dereven'Kov, I. A.; Salnikov, D. S.; Makarov, S. V.; Surducan, M.; Silaghi-Dumitrescu, R.; Boss, G. R. Comparative Study of Reaction of Cobalamin and Cobinamide with Thiocyanate. *J. Inorg. Biochem.* **2013**, *125*, 32–39. https://doi.org/10.1016/J.JINORGBIO.2013.04.011.

(73) Lee, J.; Mahon, S. B.; Mukai, D.; Burney, T.; Katebian, B. S.; Chan, A.; Bebarta, V. S.; Yoon, D.; Boss, G. R.; Brenner, M. The Vitamin B12 Analog Cobinamide Is an Effective Antidote for Oral Cyanide Poisoning. *J. Med. Toxicol.* **2016**, *12* (4), 370–379. https://doi.org/10.1007/s13181-016-0566-4.

(74) Hendry-Hofer, T. B.; Ng, P. C.; McGrath, A. M.; Soules, K.; Mukai, D. S.; Chan, A.; Maddry, J. K.; White, C. W.; Lee, J.; Mahon, S. B.; et al. Intramuscular Cobinamide as an Antidote to Methyl Mercaptan Poisoning. *Inhal. Toxicol.* **2021**, *33* (1), 25–32. https://doi.org/10.1080/08958378.2020.1866123.

(75) Ng, P. C.; Hendry-Hofer, T. B.; Garrett, N.; Brenner, M.; Mahon, S. B.; Maddry, J. K.; Haouzi, P.; Boss, G. R.; Gibbons, T. F.; Araña, A. A.; et al. Intramuscular Cobinamide

versus Saline for Treatment of Severe Hydrogen Sulfide Toxicity in Swine. *Clin. Toxicol.* **2019**, *57* (3), 189–196. https://doi.org/10.1080/15563650.2018.1504955.

(76) Jacobsen, D. W.; Troxell, L. S.; Brown, K. L. *Catalysis of Thiol Oxidation by Cobalamins and Cobinamides: Reaction Products and Kinetics*; 1984; Vol. 23, pp 2017–2025. https://doi.org/10.1021/bi00304a021.

Chapter 2. Photocatalytic turnover of CO_2 under visible light by Re(I) naphthalimide complexes in tandem with a sacrificial donor

Work in this chapter was conducted by the author unless otherwise noted. Crystals grown by the author were submitted to Dr. Max Nanao at the European Synchrotron Radiation Facility or Dr. William Brennessel at the University of Rochester for X-ray crystallography. DFT was performed by Dr. Sarah Dampf and Professor Tim Korter at Syracuse University. Quantum yield experiments were conducted by Dr. Derek Case (Doyle group, Syracuse University). Gas chromatography was performed with the assistance of Dr. Robson Schuarca and Professor Jesse Bond at Syracuse University. The author assisted with the collection of CV data conducted by Dr. Adam Henwood of Trinity College (Dublin, Ireland). The work reported in this chapter resulted in the following peer-reviewed publications:

- **Spear, A.**; Case, D. R.; Henwood, A. F.; Nanao, M.; Dampf, S.; Korter, T. M.; Gunnlaugsson, T.; Zubieta, J.; Doyle, R. P. [$Re(CO)_3$(5-PAN)Cl], a Rhenium(i) Naphthalimide Complex for the Visible Light Photocatalytic Reduction of CO_2. *Dalt. Trans.* **2021**, *50* (10), 3479–3486. https://doi.org/10.1039/D0DT04116E.
- **Spear, A.**; Schuarca, R. L.; Bond, J. Q.; Korter, T. M.; Zubieta, J.; Doyle, R. P. Photocatalytic Turnover of CO_2 under Visible Light by [$Re(CO)_3$(1-(1,10) Phenanthroline-5-(4-Nitro-Naphthalimide))Cl] in Tandem with the Sacrificial Donor BIH. *RSC Adv.* **2022**, *12* (9), 5080–5084. https://doi.org/10.1039/D1RA08261B.

2.1 Synthesis of $Re(H_2O)_3(CO)_3]X$, 5-PAN, and $[Re(CO)_3$(5-PAN)X] (X=Cl or Br)

The synthetic schemes for $[Re(H_2O)_3(CO)_3]X$, 5-PAN, and $[Re(CO)_3$(5-PAN)X] (X=Cl or Br) are shown in **Scheme 2-1** with detailed synthetic methodology and characterizations provided in Chapter 5.

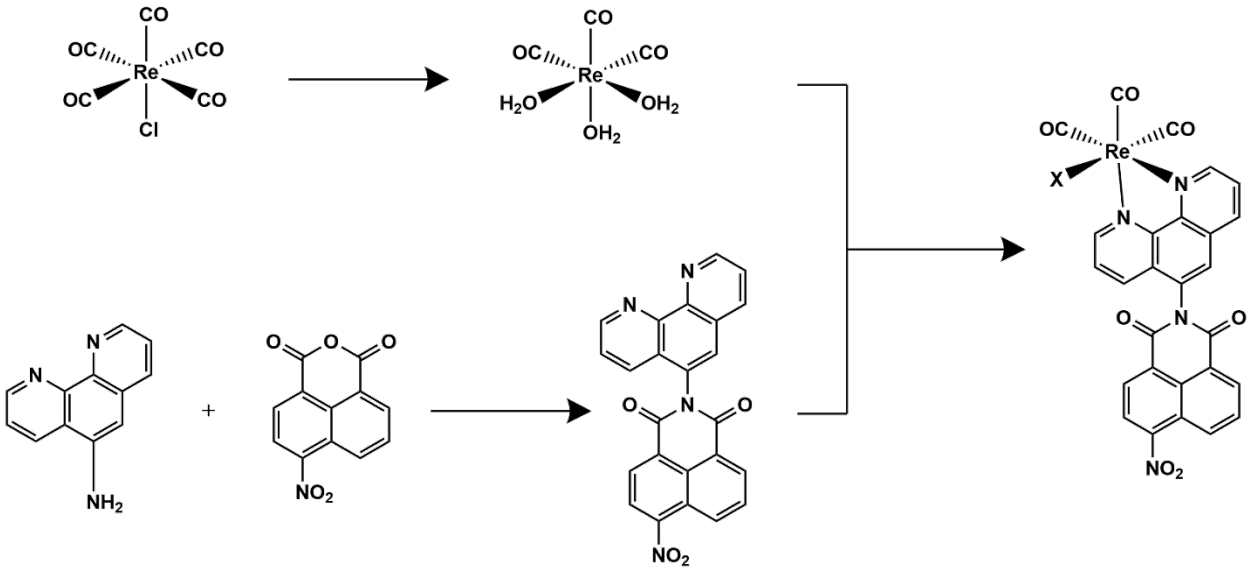

Scheme 2-1. Syntheses of $[Re(H_2O)_3(CO)_3]X$, 5-PAN, and $[Re(CO)_3$(5-PAN)X] (X = Cl or Br)

2.2 Solid state structure of $[Re(CO)_3$(5-PAN)X] (X = Cl or Br)

Solid-state structure of $[Re(CO)_3$(5-PAN)X] was obtained to facilitate DFT studies. Single-crystal X-ray diffraction analysis revealed that the catalyst crystallizes in the triclinic space group P1 with two molecules in the unit cell, one catalyst and one toluene solvate molecule. Diffraction quality crystals were only obtained from a mix of $[Re(CO)_3$(5-PAN)Cl] and $[Re(CO)_3$(5-PAN)Br]; thus the six-coordinate, octahedral rhenium center includes a disordered halido ligand

comprised of Br : Cl, 0.80 : 0.20. The CO ligands a facially coordinated, and the ligand, 5-PAN, is coordinated to the rhenium center in a bidentate fashion at N1 and N2 (**Figure 2-1**). Detailed description of the structure is included in the appendix (Appendix A).

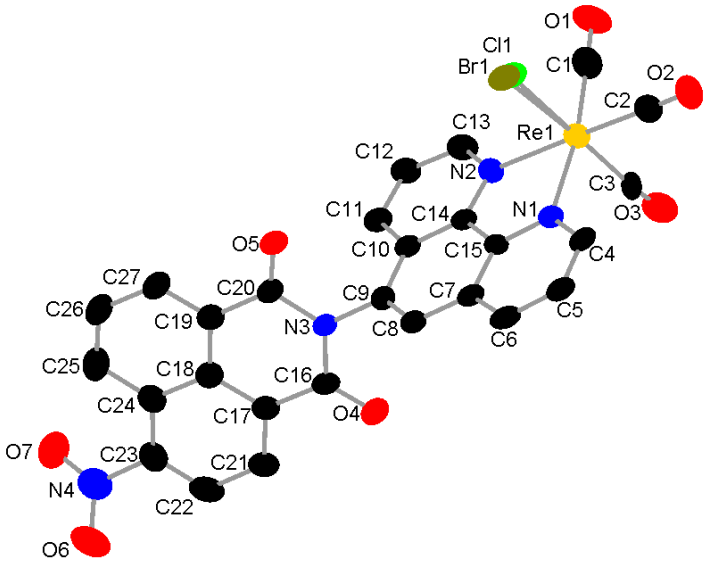

Figure 2-1. Single-crystal X-ray diffraction structure of a mixture of $[Re(CO)_3(5\text{-PAN})Cl]$ and $[Re(CO)_3(5\text{-PAN})Br]$. H-atoms and toluene solvent molecule are omitted for clarity. Structure deposited as CCDC # 2086581.

Direct coordination of chloride to the rhenium center was also supported by Raman spectroscopy and DFT. As was previously reported by *McAllister et al.*, the Raman frequency of the Re–Cl bond is observed in the far infrared region at 292 cm^{-1} [77]. This same Raman frequency was observed upon in-house analysis, and the subsequent Re–Cl bond of $[Re(CO)_3(5\text{-PAN})Cl]$ was also observed at 280 cm^{-1} – a slight shift to lower frequency as a result of the coordination of the electron-withdrawing 5-PAN (**Figure 2-2**); a trend also observed by *Kalläne et al.*[78]. This shift to lower vibrational frequencies was also support by in-house DFT conducted *in silico* (**Figure 5-21**).

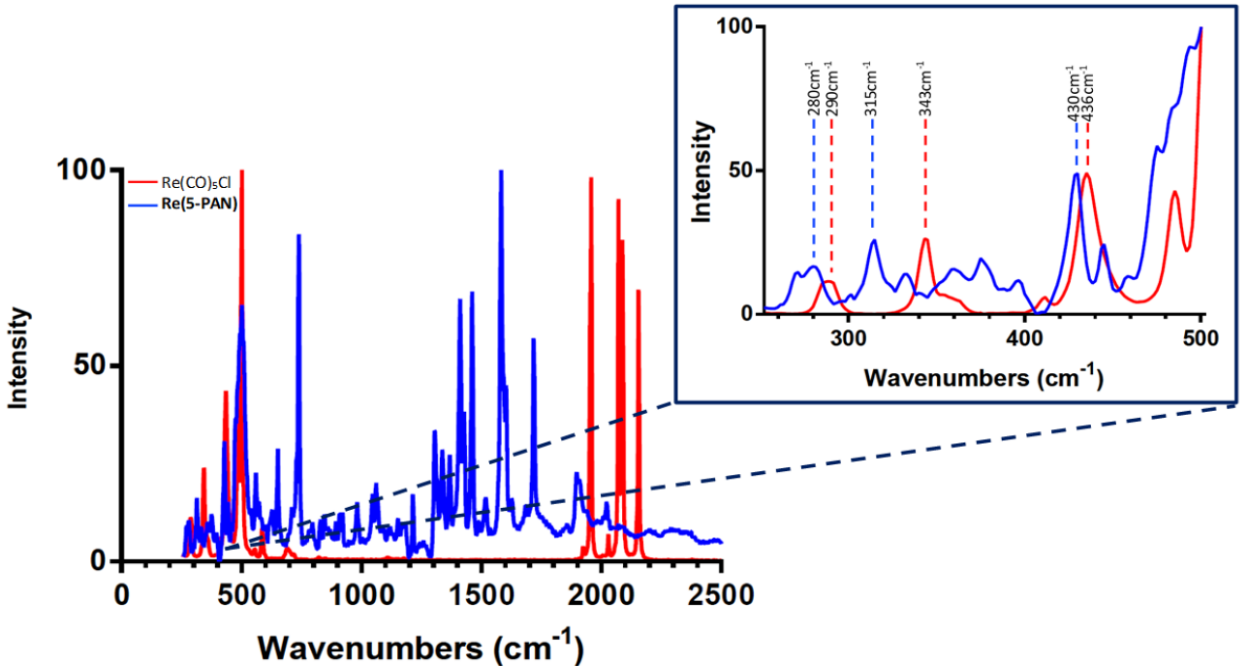

Figure 2-2. Raman spectra of starting material $Re(CO)_5Cl$ (red) and $[Re(CO)_3(5\text{-PAN})Cl]$ (Re(5-PAN), blue) highlighting the solid-state rhenium-chloride bonds at 290 and 280 cm^{-1}, respectively. In the case of $[Re(CO)_3(5\text{-PAN})Cl]$, the Raman spectrum showed a significant fluorescence background with well-defined Raman peaks on top of this. An approximate polynomial baseline representing the fluorescence interference was subtracted from the final data shown here. See also DFT calculations in **Figure 5-21**.

2.3 Density functional theory

The full geometry optimization yielded a final structure that was in good agreement with the X-ray diffraction results described herein for $[Re(CO)_3(5\text{-PAN})Cl]$. The Tamm-Dancoff approximation (TDA) simulation yielded a predicted UV/VIS spectrum that matched well with the experimental data (**Figure 2-3**), indicating the high quality of the calculated orbitals energies and participating states. Of particular interest to the photocatalytic behavior are the four transitions with non-zero oscillator strength in the 400 to 500 nm region. These singlet

transitions are detailed in **Table 2-1** and the strongest transition, HOMO-1 → LUMO+1, is visualized in **Figure 2-4**. Other transitions are visualized in **Table 5-2**.

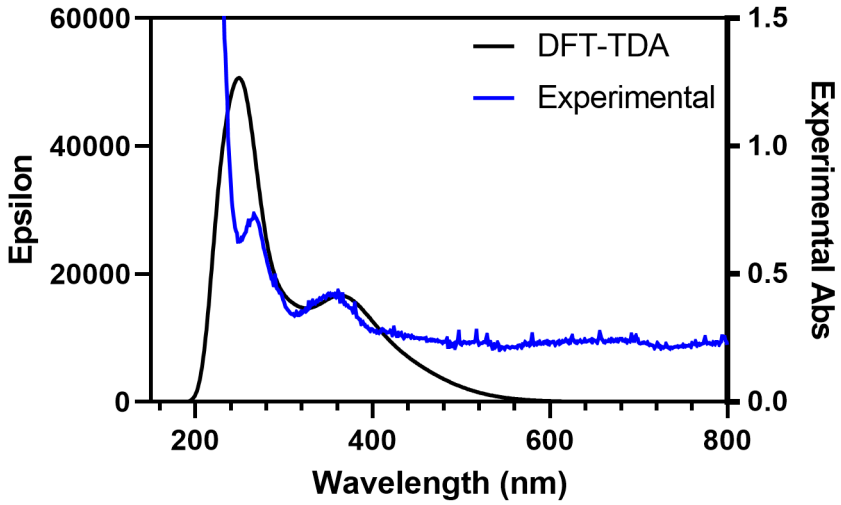

Figure 2-3. Overlay of DFT-TDA (black) and experimental absorbance spectrum of $[Re(CO)_3(5\text{-}PAN)Cl]$ (blue).

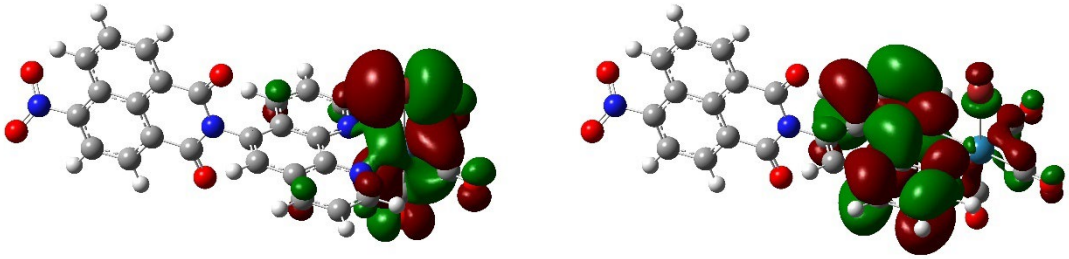

Figure 2-4. Orbital density plots for HOMO-1 → LUMO+1. The trend in these excitations is a migration of electron density from the Re atom to the ligand.

Table 2-1. Singlet transitions of $[Re(CO)_3(5\text{-PAN})Cl]$

Excitation Wavelength (nm)	Oscillator strength (f)	Main Participating Orbitals and Percentage Contributions
470.63	0.0016	HOMO → LUMO+1 (99%)
446.59	0.0680	HOMO-1 → LUMO+1 (90%) HOMO → LUMO+2 (8%)
426.62	0.0345	HOMO-1 → LUMO+1 (8%) HOMO → LUMO+2 (90%)
416.46	0.0172	HOMO-1 → LUMO+2 (98%)

2.4 Cyclic voltammetry on $[Re(CO)_3(5\text{-PAN})Cl]$

Cyclic voltammetry (CV) was undertaken to discern the energies of the HOMO and LUMO of the complex, which is crucial for understanding its capacity to perform as a photocatalyst. The CV traces of 5-PAN and $[Re(CO)_3(5\text{-PAN})Cl]$ in acetonitrile and DMF are given in **Figure 2-5**, and the relevant parameters obtained for the electrochemical experiments are summarized in **Table 2-2**. The CV trace for 5-PAN exhibits two reversible reduction waves and a third reduction wave close to the solvent window. $[Re(CO)_3(5\text{-PAN})Cl]$ also exhibits two reversible reduction waves at modestly cathodically shifted potentials with respect to the ligand. This small shift is due to the charged metal ion which inductively withdraws electron density from the ligand, making it more capable of accepting electrons when coordinated to the metal. There is also a third, more anodically shifted, reversible reduction wave.

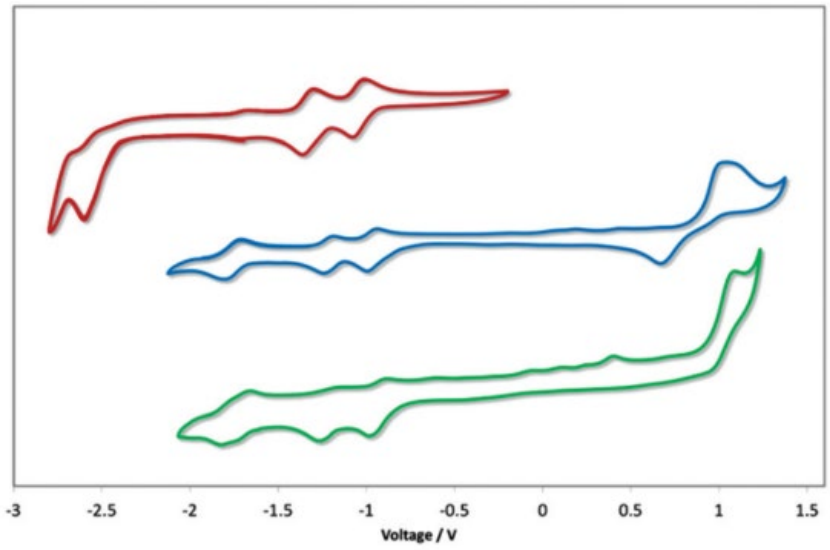

Figure 2-5. Cyclic voltammograms of 5-PAN in acetonitrile (red, top), $[Re(CO)_3(5\text{-PAN})Cl]$ in acetonitrile (blue, middle), and $[Re(CO)_3(5\text{-PAN})Cl]$ in DMF (green, bottom).

No oxidation of 5-PAN was observed, but $[Re(CO)_3(5\text{-PAN})Cl]$ did exhibit a complex multi-electron oxidation process [$E_{pc(ox)}$ = +0.84 V] that is probably irreversible given the offset in potential of the return wave is too large for a typical reversible process. The oxidation potential and its irreversible nature is similar to other rhenium complexes reported in the literature [$E_{1/2(ox)}$ = ca. +0.70–1.0 V][79,80] although it is somewhat different from the structurally similar complex $[Re(CO)_3(phen)(Cl)]$ (Re(phen)), for which the first irreversible oxidation is cathodically shifted in ACN [$E_{pa(ox)}$ = +1.03 V][81]. The multiple reduction processes observed for both 5-PAN and $[Re(CO)_3(5\text{-PAN})Cl]$ arises from the presence of the individual phenanthroline and nitro-naphthalimide moieties, both of which are capable of acting as electron sinks. A helpful comparison in ascribing the reduction processes is the complex $[Re(CO)_3(5\text{-PAN})Cl]$, wherein PNI denotes a naphthalimide with a piperidinyl electron donating group[82]. In this complex, the two analogous reduction waves are anodically shifted [$E_{1/2(red)}$ = −1.59, −1.73 V]

Table 2-2. Relevant electrochemical data for 5-PAN and $[Re(CO)_3(5\text{-PAN})Cl]^a$

	Compound		
	5-PAN[a]	$[Re(CO)_3(5\text{-PAN})Cl]^a$	$[Re(CO)_3(5\text{-PAN})Cl]^b$
$E_{pa(ox)}$ (V)	-	+0.84[c]	+0.95
$E_{1/2(red1)}$ (V)	−1.03	−0.95	−0.92
$E_{1/2(red2)}$ (V)	−1.31	−1.18	−1.08[d]
$E_{1/2(red3)}$ (V)	−2.42[d]	−1.73	−1.73
E_{redox} [e] (V)	-	+1.70	+1.70
E_{HOMO} [f] (eV)	-	−5.64	−5.75
E_{LUMO} [f] (eV)	−3.86	−3.98	−4.11
$\Delta E_{LUMO-HOMO}$ (eV)	-	1.64	1.64

[a] Measurements were carried out in MeCN at a scan rate of 100 mV s^{-1} with Fc/Fc^+ employed as an internal standard and are reported vs. Fc/Fc^+. [b] Measurements were carried out in DMF at a scan rate of 100 mV s^{-1} with Fc/Fc^+ employed as an internal standard and are reported vs. Fc/Fc^+. [c] This wave is irreversible, and the value reported is the onset of oxidation in the anodic scan direction. [d] This wave is irreversible, and the value reported is the onset of reduction in the cathodic scan direction. [e] E_{redox} is defined as the difference in onset potential of the first oxidation [$E_{pa(ox)}$] and first reduction [$E_{pc(red)}$]. [f] $E_{HOMO/LUMO} = -[E_{ox/red}$ vs. $Fc/Fc^+ + 4.8]$ eV[83].

compared to $[Re(CO)_3(5\text{-PAN})Cl]$ [82]. DFT calculations ascribed the first wave to reduction of phenanthroline and the second to naphthalimide reduction, which is in line with destabilization of both sets of orbitals but particularly the naphthalimide by the electron donating piperidine. However, in the case of $[Re(CO)_3(5\text{-PAN})Cl]$, the much more electron deficient nature of the nitro-naphthalimide stabilizes it such that it is the first reduction [$E_{1/2(red)} = -0.95$ V] while the second reduction [$E_{1/2(red)} = -1.18$ V] is reduction of the phenanthroline.

In order to characterize the nature of the oxidation measurements were also conducted on [$Re(CO)_3$(5-PAN)Cl] in DMF (**Figure 2-5**) which is a poorly coordinating solvent. In the cathodic scan the CV profile of the complex in DMF was similar to that observed in ACN, with three reduction waves, all of which appeared at similar potentials to those observed in ACN, although the reduction waves are much less reversible. However, the oxidation of [$Re(CO)_3$(5-PAN)Cl] in DMF has very different features. In the characterization of the electrochemical oxidation of Re(phen), the first oxidation [$E_{pa(ox)}$ = +1.39 V] of this complex is ascribed to loss of radical chlorine followed by rapid solvent coordination, while the second reversible oxidation [$E_{1/2(ox)}$ = +1.79 V] is ascribed to the Re(I)/Re(II) redox couple[81]. Although the potentials of these processes are different to that observed for 5-PAN in ACN [$E_{pa(ox)}$ = +0.84 V], the combination of a multielectron process and return wave at ca. +0.7 V points towards a similar electrochemical phenomenon in effect here. The first oxidation is likely to be loss of chlorine radical, with the return wave likely to be due to electrochemical reaction with the free chlorine radical, and the second process constituting the metal centered oxidation. This is in contrast to the CV trace in DMF, where the poorer coordinating properties of DMF preclude the displacement of chlorine radical for solvent, resulting in a simpler oxidation process [$E_{pa(ox)}$ = +0.95 V] comprised of the one electron oxidation of Re(I) to Re(II). The similar redox potentials for both the oxidation and reductions in ACN and DMF point toward a molecule with a small dipole moment in the ground state, as the electronics of the system appear insensitive to solvent polarity. This is clearly evidenced by the complex exhibiting the same net electrochemical (DE) and HOMO–LUMO gaps in ACN and DMF (DE = +1.70, |HOMOLUMO| = 1.64 eV) and DMF.

2.5 Quantum yield of $[Re(CO)_3(5\text{-PAN})Cl]$

The quantum yield of $[Re(CO)_3(5\text{-PAN})Cl]$ was determined using a comparative emission method. After synthesizing Re(phen) in-house utilizing the method of *Marti et al.*[84], emission experiments were conducted. Absorption spectra of both $[Re(CO)_3(5\text{-PAN})Cl]$ and $[Re(CO)_3PhenCl]$ were taken and the absorption intensities kept to between 0.1–0.2. Utilizing the λ_{max} values of the metal-to-ligand charge transfer (MLCT) absorption bands of both $[Re(CO)_3(5\text{-PAN})Cl]$ and Re(phen) (λ_{max} = 351 nm and 361 nm, respectively) emission spectra were recorded and the integrations of the respective emission spectra were determined. After obtaining these values, equation 1 was applied with the reported quantum yield of Re(phen) (φ =0.017)[84], producing a quantum yield for $[Re(CO)_3(5\text{-PAN})Cl]$ of φ = 0.021 ± 0.003. This was calculated using equation 1.

$$\varphi_{Re(5\text{-PAN})} = \varphi_{Re(phen)} \left(\frac{(A_{Re(phen)})(I_{Re(5\text{-PAN})})}{(A_{Re(5\text{-PAN})})(I_{Re(phen)})} \right) \quad (1)$$

Equation utilized to calculate the quantum yield of $[Re(CO)_3(5\text{-PAN})Cl]$ ($\varphi_{Re(5\text{–PAN})}$). φ_{RePhen} is representative of the reported quantum yield of Re(phen) and *A* and *I* are the absorbance intensity and emission integration of the respective $[Re(CO)_3(5\text{-PAN})Cl]$ and Re(phen) species.

2.6 Evaluation of the excited state of $[Re(CO)_3(5\text{-PAN})Cl]$

To determine whether the MLCT being accessed during catalysis is a triplet ^{3}MLCT or a singlet ^{1}MLCT, the electron absorption spectrum of $[Re(CO)_3(5\text{-PAN})Cl]$ was collected in both

methanol and dichloromethane – if the accessible excited state of Re(5-PAN) were a triplet ^{3}MLCT, there would be a bathochromic shift observable in the electronic absorption spectrum upon the utilization of the more polar methanol solvent. Upon collecting the electronic absorption spectrum of [Re(CO)$_3$(5-PAN)Cl] in methanol there was a minimal (ca. 2 nm) bathochromic shift relative to the electronic absorption spectrum of [Re(CO)$_3$(5-PAN)Cl] collected in dichloromethane (**Figure 5-14**).

Subsequently, however, electronic absorption spectra for [Re(CO)$_3$(5-PAN)Cl] were collected in aerated and degassed methanol at equimolar concentrations, analysis of which showed no change in absorption intensity (**Figure 5-14**), which is consistent with singlet ^{1}MLCT fluorescence, as quenching of a singlet excited state by oxygen is unlikely relative to the ^{3}MLCT; if the excited state were a ^{3}MLCT, there would be an observable decrease in absorption intensity. The excited state being a ^{1}MLCT would be consistent with naphthalimides commonly acting as fluorophores, but to this end, the final excited state has not been assigned, as these results are inconclusive and further studies are required to confirm the final excited state.

2.7 Photocatalysis

The following is a typical experiment using [Re(CO)$_3$(5-PAN)Cl]. In each sample tested, 0–300 equivalences of triethylamine (TEA, 0–5.44 mmol) or 0–110.3 equivalences of BIH (0–2 mmol) were premixed in MeOH/DCM (1 : 9 v/v) for 10 min, after which, 13.5 mg (0.018 mmol) of [Re(CO)$_3$(5-PAN)Cl] was added. All samples were kept at a 5 mL total reaction volume, irradiated with blue light positioned 1 inch from the reaction vessel and at a 21° angle of incident light. The solution was bubbled with $^{13}CO_2$ evolved in situ with 0.500 g $Ba^{13}CO_3$ and 1

M H_2SO^4 drip for a reaction time of 1.5 hours. For each trial, the drip rate was set such that the Schlenk flask containing $Ba^{13}CO_3$ was full at the end of 1.5 hours and the H_2SO_4 was well in excess. All catalytic experiments were conducted at least in triplicate under blue light irradiation. At the end of each trial, liquid products were quantified via ^{13}C NMR. 400 mL of the reaction solution and 200 mL of $CDCl_3$ were added to an NMR tube and wrapped in aluminum foil until it was ready to be loaded into the NMR instrument. The carbon peaks for TEA at ~10 and 46 ppm were integrated and set to 1. The carbon peaks for BIH and its oxidative product, BI^+, at ~33 ppm were integrated and set to 1. The $H^{13}COO^-$ peak at ~160 ppm was integrated and quantified with a calibration curve (**Figure 5-25** and **Figure 5-29**). For the detection of gaseous products, Re(5-PAN) and BIH were dissolved in MeOH/DCM (1 : 9 v/v) in a vial with a stir bar and rubber septum. The vial was purged with CO_2 for 20 min, then irradiated with blue light for 30 min. A headspace sample was taken with a 1 mL airtight syringe and analyzed by GC.

2.7.1 $[Re(CO)_3(5\text{-PAN})Cl]$ with TEA

Catalytic studies of $[Re(CO)_3(5\text{-PAN})Cl]$ showed that reduction was dependent upon photoirradiation with 450–460 nm blue light – in the absence of blue light, no catalytic conversion of CO_2 was observed (**Figure 5-24**) – and that catalytic conversion was dependent on the fully complexed $[Re(CO)_3(5\text{-PAN})Cl]$ complex and not the ligand alone (**Figure 5-23**). The catalytic capability of $[Re(CO)_3(5\text{-PAN})Cl]$ to reduce $^{13}CO_2$ to $H^{13}COO^-$ was quantified with the integration of the $H^{13}COO^-$ peak at ∼160 ppm on the ^{13}C NMR spectrum relative to the TEA peak (**Figure 2-6**). This value was subsequently confirmed by developing a calibration curve of the integrations of known concentration of formate (**Figure 5-25**) that were within the range of catalytically produced formate.

Analysis of the catalytic data shows that the production of $H^{13}COO^-$ correlates with the addition of excess TEA in an exponential trend with R^2 = 0.9682. Catalytic saturation of the system is indicated by the plateau such that the maximum $H^{13}COO^-$ produced is 0.87 mmol, corresponding to a turnover number (TN = $[H^{13}COO^-]/[[Re(CO)_3(5\text{-PAN})Cl]]$) of 48–50 at 300 equiv. TEA where the concentration of $[Re(CO)_3(5\text{-PAN})Cl]$ was 3.62 mM in 5 mL. This value is in accordance with literature values ranging from 0–230 with irradiation time periods ranging from 30 minutes to 24 hours[9-12,14,19,85–95]. More precisely, this value is comparable to the 48 TN reported by *Hawecker et al*. for a similar rhenium diamine bidentate complex utilizing bipyridine over a similar time scale[14]. Quantified formate values resulting from catalysis experiments were validated utilizing a calibration curve fit to a set of formate standards of concentrations from 0–0.2 M in 1:9 (v:v) MeOH/DCM and 100 equivalents TEA, and the subsequent integration of the ^{13}C peak of formate with TEA set as an integration of 1 at D1 relaxation times of 1, 2, and 5 seconds – the calibration curve for D1= 5s showed an R^2 =

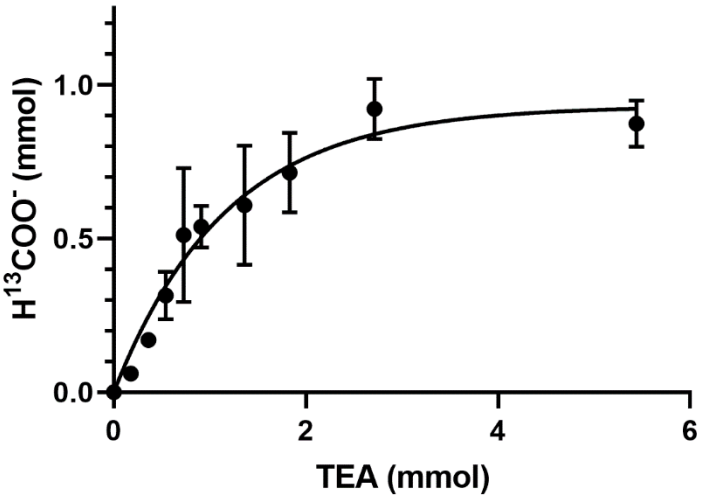

Figure 2-6. A plot of $H^{13}COO^-$ (mmol) vs. TEA (mmol) upon blue light (450–460 nm) irradiation in the presence of [Re(CO)$_3$(5-PAN)Cl]. $H^{13}COO^-$ increased with an exponential curve fit with R^2 = 0.9682 and reaching a plateau at y = 0.87 mmol $H^{13}COO^-$.

0.9978; similar R^2 values were observed for D1 =1s and D1 =2s (**Figure 5-25**). The subsequent reported quantified formate TN values are extrapolated by multiplying the experimentally determined formate value by the scale factor of TEA (**Figure 2-6** and **Figure 5-26**). The reported turnover numbers at D1 = 1 s, 2 s, and 5 s are consistent with each other (**Figure 5-26**).

2.7.2 [Re(CO)$_3$(5-PAN)Cl] with BIH

It should be noted that at higher concentrations of BIH (≥1 mmol), the limit of solubility in MeOH/DCM (1 : 9 v/v) in the presence of catalyst was reached, requiring that the BIH be dissolved in the solvent system prior to addition of the catalyst. Without this order of dissolution, the catalytic production of $H^{13}COO^-$ at concentrations of BIH ≥ 1 mmol, was highly variable (**Figure 5-28**) as undissolved BIH would be misrepresented in the calibration curve (**Figure 5-29**).

The production of $H^{13}COO^-$ correlates with the addition of excess BIH and blue light in an exponential trend with R^2 = 0.9932 (**Figure 2-7**). A plateau at 9.48 mmol indicated the maximum $H^{13}COO^-$ produced and catalytic saturation. The maximum TN achieved was 533, and turnover frequency (TOF = TN/reaction time) 356 h^{-1} at ~110 equivalences of BIH, where the concentration of $[Re(CO)_3(5\text{-PAN})Cl]$ was 3.62 mM in 5 mL of MeOH/DCM (1 : 9 v/v). $[Re(CO)_3(5\text{-PAN})Br]$ was also tested for photocatalytic activity and showed no functional difference from that of [Re(CO)3(5-PAN)Cl], which is in contradiction to some literature reports which have seen halide degradation kinetics differences[14,15]. No formate was detected in the absence of catalyst, BIH, or $^{13}CO_2$ and a negligible amount was detected in the absence of irradiation. The calculated TN of 533 not only surpasses our previously reported $[Re(CO)_3(5\text{-PAN})Cl]$/TEA system tenfold but introduces a standard for selective turnover of CO_2 to formate *via* a mononuclear rhenium(I) catalyst.

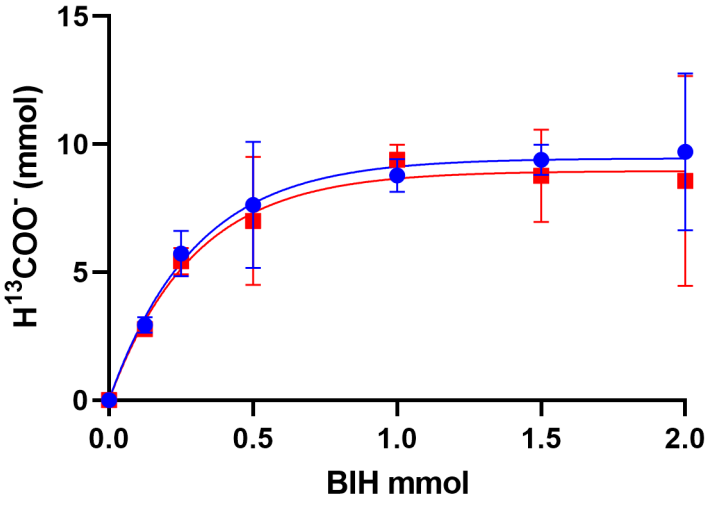

Figure 2-7. A plot of $H^{13}COO^-$ (mmol) vs. BIH (mmol) upon blue light irradiation of $[Re(CO)_3(5\text{-PAN})Cl]$ (blue circles, R^2 = 0.9932) and $[Re(CO)_3(5\text{-PAN})Br]$ (red squares, R^2 = 0.9864). $H^{13}COO^-$

increased with an exponential curve fit and reached a plateau at y = 9.45 and 8.96 mmol $H^{13}COO^-$, respectively.

The production of HCO_3^- has also been reported appearing on ^{13}C NMR at ~158 ppm[19]. Ion chromatography was therefore conducted and confirmed the identity of formic acid, and lack of carbonate (**Figure 5-30**). Gaseous products of photocatalysis were also analyzed by GC. Trace quantities of CO were detected at a maximum production of 820 nmol CO corresponding to a TN of 0.04 and a TOF of 0.09 h^{-1} (**Figure 5-31**).

2.8 Effects of solvent on photocatalysis

The solvent system MeOH/DCM (1 : 9 v/v) was chosen because it best solubilized all of the reaction components, however MeOH has been reported to enhance the catalytic activity of rhenium diimine complexes by increasing the current in electrolysis experiments[97]. To reveal the effect of MeOH in photocatalysis, experiments were done in the presence of deuterated methanol (along with DMF at typical 1:9 v/v ratio used before). When DCM was used as the lone solvent, no formate was produced as evidenced by the loss of the ~160 ppm peak in the ^{13}C NMR and the subsequent emersion of a weak peak at ~156 ppm with an integration of 0.6. When MeOH was replaced with CD_3OD (CD_3OD/DCM 1 : 9 v/v), the ~160 ppm peak was reduced to an integration of 0.9 (**Figure 5-32**).

In DMF alone, a common solvent used in rhenium photocatalysis, the formate peak was also not seen in the ^{13}C NMR and a peak at ~156 ppm was seen with an integration of 7.6. It should be noted that the aldehyde carbon of DMF has a peak at 161 ppm, therefore a formate peak could be occluded. Nonetheless, the absence of MeOH resulted in the loss of the signature formate peak at 160 ppm and subsequent appearance of a peak slightly upfield at 156

ppm with greatly diminished integration. When experiments were conducted in MeOH/DCM with no CO_2, no carbon signal was observed above 150 ppm, thus the source of the carbon is indeed CO_2 with no degradation of MeOH itself. MeOH is likely necessary for catalysis as a major proton source.

2.9 Photocatalytic mechanism

A variety of factors including solvent, sacrificial donor, and halide ligand can affect the catalytic activity of rhenium diimine complexes. TLC analysis of the reaction mixture before and after irradiation showed no obvious degradation of the catalyst while BI^+ did separate from BIH (**Figure 5-33**), which was also indicated by NMR. With the addition of BIH, compared to TEA, TN was dramatically increased possibly due to the increase in reductive power and efficient formation of the one-electron reduced catalytic species[8]. When TEMPO was added in equimolar concentrations to BIH, the integration of formate increased, suggesting TEMPO acting as a hydride donor. These observations allude to a hydride mechanism.

A possible mechanism is described (**Figure 2-8**). After reductive quenching of the photoexcited catalyst by BIH, the halide dissociates, and the active catalyst is produced. Literature descriptions of formate generation then propose the formation of a metal hydride intermediate[4,98–100]. Insertion of CO_2 into the M−H bond then produces the intermediate. This process is in competition with H_2 generation, which cannot be detected as H_2 is used a co-feed gas for the methanizer during GC analysis.

In control experiments in the absence of light, formate was still detected, reaching a maximum amount of 3.20 mmol (R^2 = 0.9037) corresponding to a TN of 176 at 110 equivalents

of BIH to $[Re(CO)_3(5\text{-PAN})Cl]$. To explain the cause of this activity, we noted a literature report of BIH forming a radical cation in the presence of atmospheric O_2 without irradiation[101]. Under blue light irradiation, BIH alone, in MeOH/DCM (1:9 v/v), was able to reduce CO_2 to formate with a low turnover of 5.7 (TN = [formate]/[BIH]). Given the sizable difference in TN from 5.7 to 533, we conclude that any BIH-only mechanism is overridden in the presence of $[Re(CO)_3(5\text{-PAN})Cl]$ by the hydride mechanism.

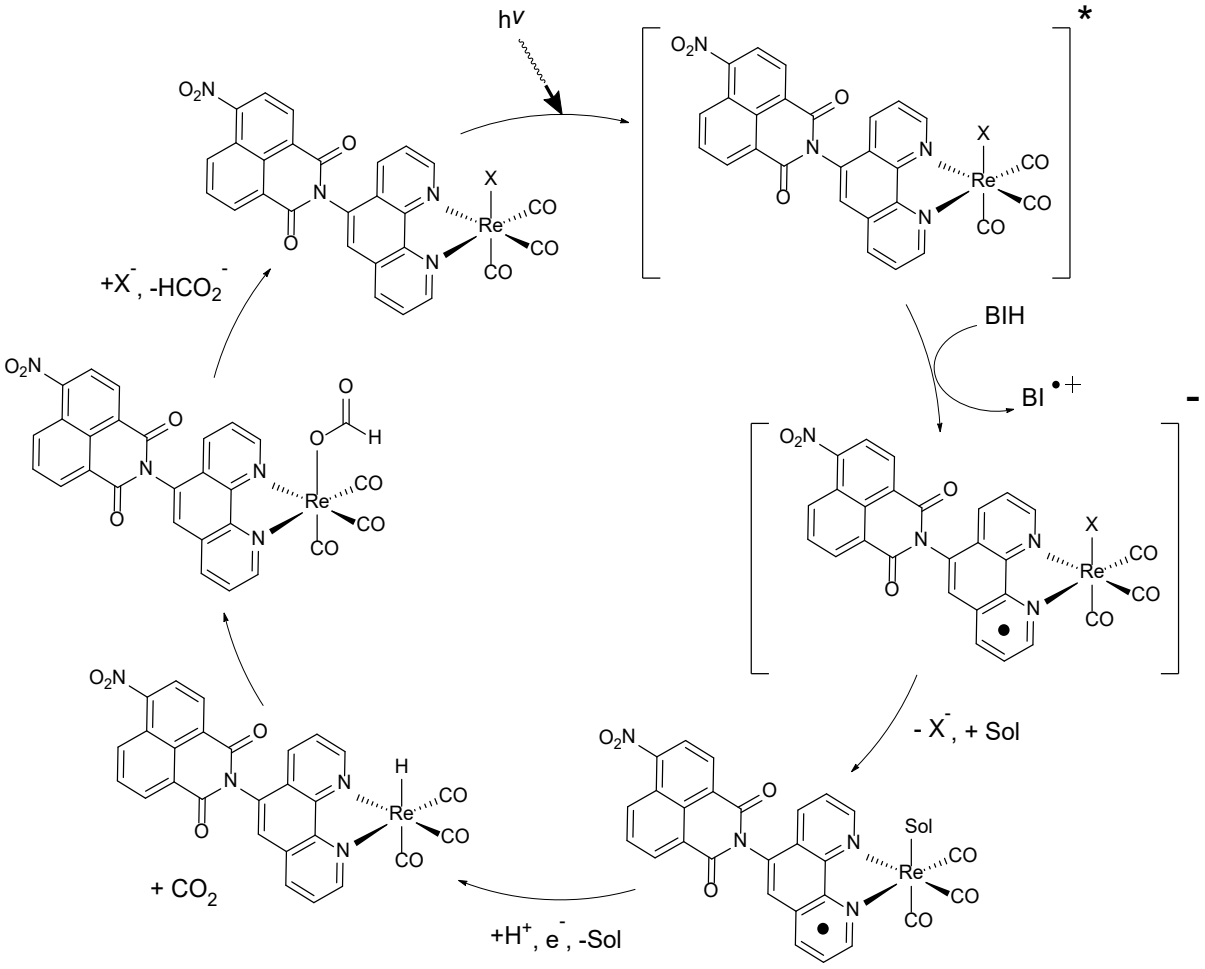

Figure 2-8. Proposed hydride mechanism of CO_2 reduction to formate via $[Re(CO)_3(5\text{-PAN})Cl]$ or $[Re(CO)_3(5\text{-PAN})Br]$. X = Cl or Br, Sol = DCM or MeOH.

The hydride mechanism shown in **Figure 2-8**. only accounts for one BIH per catalytic cycle, whereas the TN is 533 with 110 equivalences of BIH. This suggests multiple mechanisms

or components are contributing to the formation of formate herein. Notably, the role of methanol is underappreciated in the proposed mechanism and may account for the enhanced TN.

2.10 Conclusion

Herein, the synthesis, structural characterization, electrochemistry, and photocatalytic activity of two novel rhenium(I) naphthalimide complexes were reported. Solid-state characterization of $[Re(CO)_3(5\text{-PAN})Cl]$ indicated an octahedral complex indicating facial coordination of three CO ligands, bidentate coordination of the naphthalimide-based photosensitizing ligand, and direct coordination of a halide in the solid state. It should be noted, however, that solvent displacement of chloride in coordinative solvent is highly probable, and in this case confirmed via cyclic voltammetry. Electrochemical evaluation of $[Re(CO)_3(5\text{-PAN})Cl]$ indicated sufficient reduction potential to reduce CO^2 to $HCOO^-$, and as such, catalytic experiments were undertaken.

Production of $H^{13}COO^-$ was evaluated in relation to the sacrificial electron-donor TEA or BIH via ^{13}C NMR and confirmed to be dependent upon photoirradiation. Analysis of the catalytic data obtained for $[Re(CO)_3(5\text{-PAN})Cl]$ indicated that production of $H^{13}COO^-$ increased with additional molar equivalents of TEA, and plateaued at 0.87 mmol $H^{13}COO^-$ at 150 equivalents TEA. This method was verified via comparison to the observed integration of a set of formate standards of known concentration and the subsequent calibration curves produced from this data and confirms the method as a valid means of formate quantification. The reported quantified formate values are consistent at NMR relaxation times of D1= 1s, 2s, and 5s. The TN

and TOF of the rhenium(I) naphthalimide complex were improved in the presence of BIH. The generated $H^{13}COO^-$ increased with excess BIH until a plateau was reached at 9.45 mmol of $H^{13}COO^-$. The corresponding TN at 110 equivalents of BIH to $[Re(CO)_3(5\text{-PAN})Cl]$ is 533, a tenfold improvement to catalysis using TEA and marked selectivity over CO production, which was observed in nanomole quantities. MeOH/DCM was not only used for its ability to solvate the catalyst, but to optimize the production of $H^{13}COO^-$; DCM or DMF lead to diminished $H^{13}COO^-$ signal. While the addition of MeOH improved catalytic activity, the source of the carbon was CO_2. To date, this TN is the only reported value for a rhenium(I) mononuclear homogeneous photocatalyst for the selective photoreduction of CO_2 to formate.

$[Re(CO)_3(5\text{-PAN})Cl]$ is an exciting complex to apply towards CO_2 reduction as the field is developing new methods of synthesizing valuable chemicals while maintaining sustainable and mild conditions. The complex itself is an interesting avenue for future investigation in terms of development through derivatization of the bidentate naphthalimide ligand and optimization of the solvent system to better harness the quenching capabilities of BIH.

2.11 Future directions

2.11.1 Expanding substrate scope

Though not the target of the present thesis, it is worth noting the second highest contributor to climate change, methane. While CO_2 is a climate modifier due to its long lifetime and high abundance, methane impacts the climate via its strong radiative efficiency, or heat-trapping ability. Methane lifetime is relatively short at 9 years, making it a potent short term climate forcer that will dissipate in a decade so long as the emissions are kept low[1]. The

catalyst described herein was not subject to methane atmosphere, however, it is certainly an available avenue of research as molecular metal catalysts are versatile tools to study strategies for reducing greenhouse gas emissions. Additionally, at similar reduction potentials to those reported for [$Re(CO)_3$(5-PAN)Cl], electrosynthesis of methylamine from CO_2 and NO_3^- was recently reported[102] and will be explored with [$Re(CO)_3$(5-PAN)Cl]/BIH.

2.11.2 Derivatization of 5-PAN

The 5-PAN naphthalimide system used herein is readily derivatized with a variety of substituents, allowing for the modification of the lowest excited state of the complexes; the emissive, likely singlet ^{1}MLCT fluorescent state can be tuned by modification of the ancillary ligand and the identity of the leaving group X, but this excited state must first be confirmed and will be evaluated in the future utilizing time-dependent density functional theory (TD-DFT) experiments that will analyze excited state lifetime as an indicator of excited state identity. Further mechanistic studies are needed to elaborate on the complex mechanism at play, especially the role of MeOH.

2.11.3 AFH series (Py/Pic-Nap-TPA/Cbz)

Another series of naphthalimide-based ligands were developed to explore the necessity of continuous conjugation and ligand to metal charge transfer for CO_2RR (**Figure 2-9**). The compounds incorporate a picolyl- or pyridyl- group at the at the chelate head thus breaking or maintaining conjugation, respectively. At the 4-position of the naphthalimide, triphenylphosphine (TPA) or carbazole (Cbz) is incorporated, both have interesting photophysical properties, are well characterized, and used in a variety of applications[103]. This series was characterized as photoactive supramolecular compounds by the Gunnlaugsson

group at Trinity College Dublin while complexation to rhenium and subsequent photocatalysis experiments are underway at Syracuse University.

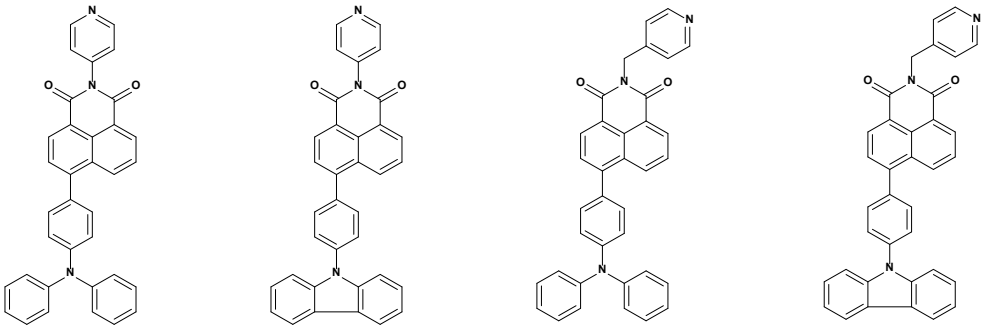

Figure 2-9. From left to right, the structure of Py-NAP-TPA, Py-NAP-Cbz, Pic-NAP-TPA, and Pic-NAP-Cbz

2.12 References

(77) McAllister, W. A.; Marston, A. L. The Infrared and Raman Spectra of Rhenium Carbonyl Chloride and Bromide. *Spectrochim. Acta Part A Mol. Spectrosc.* **1971**, *27* (3), 523–525. https://doi.org/10.1016/0584-8539(71)80060-0.

(78) Kalläne, S. I.; van Gastel, M. Raman Spectroscopy as a Method to Investigate Catalytic Intermediates: CO 2 Reducing [Re(Cl)(Bpy-R)(CO) 3] Catalyst. *J. Phys. Chem. A* **2016**, *120* (38), 7465–7474. https://doi.org/10.1021/acs.jpca.6b07246.

(79) Ng, C. O.; Lai, S. W.; Feng, H.; Yiu, S. M.; Ko, C. C. Luminescent Rhenium(i) Complexes with Acetylamino- and Trifluoroacetylamino-Containing Phenanthroline Ligands: Anion-Sensing Study. *Dalt. Trans.* **2011**, *40* (39), 10020–10028. https://doi.org/10.1039/c1dt10831j.

(80) Liu, X.; Xia, H.; Gao, W.; Wu, Q.; Fan, X.; Mu, Y.; Ma, C. New Rhenium(i) Complexes with

Substituted Diimine Ligands for Highly Efficient Phosphorescent Devices Fabricated by a Solution Process. *J. Mater. Chem.* **2012**, *22* (8), 3485–3492. https://doi.org/10.1039/c2jm14222h.

(81) Franco, F.; Cometto, C.; Garino, C.; Minero, C.; Sordello, F.; Nervi, C.; Gobetto, R. Photo- and Electrocatalytic Reduction of CO 2 by [Re(CO) 3 {α,A'-Diimine-(4-Piperidinyl-1,8-Naphthalimide)}Cl] Complexes. *Eur. J. Inorg. Chem.* **2015**, No. 2, 296–304. https://doi.org/10.1002/ejic.201402912.

(82) Paolucci, F.; Marcaccio, M.; Paradisi, C.; Roffia, S.; Bignozzi, C. A.; Amatore, C. Dynamics of the Electrochemical Behavior of Diimine Tricarbonyl Rhenium(I) Complexes in Strictly Aprotic Media. *J. Phys. Chem. B* **1998**, *102* (24), 4759–4769. https://doi.org/10.1021/jp980659f.

(83) Cardona, C. M.; Li, W.; Kaifer, A. E.; Stockdale, D.; Bazan, G. C. Electrochemical Considerations for Determining Absolute Frontier Orbital Energy Levels of Conjugated Polymers for Solar Cell Applications. *Adv. Mater.* **2011**, *23* (20), 2367–2371. https://doi.org/10.1002/adma.201004554.

(84) Martí, A. A.; Mezei, G.; Maldonado, L.; Paralitici, G.; Raptis, R. G.; Colón, J. L. Structural and Photophysical Characterisation of Fac-[Tricarbonyl(Chloro)- (5,6-Epoxy-1,10-Phenanthroline)Rhenium(I)]. *Eur. J. Inorg. Chem.* **2005**, No. 1, 118–124. https://doi.org/10.1002/ejic.200400531.

(85) Morimoto, T.; Tanabe, J.; Sakamoto, K.; Koike, K.; Ishitani, O. Selective H 2 and CO Production with Rhenium(I) Biscarbonyl Complexes as Photocatalyst. *Res Chem Intermed*

2013, *39*, 437–447. https://doi.org/10.1007/s11164-012-0661-3.

(86) Teesdale, J. J.; Pistner, A. J.; Yap, G. P. A.; Ma, Y. Z.; Lutterman, D. A.; Rosenthal, J. Reduction of CO2 Using a Rhenium Bipyridine Complex Containing Ancillary BODIPY Moieties. *Catal. Today* **2014**, *225*, 149–157. https://doi.org/10.1016/j.cattod.2013.10.091.

(87) Whang, D. R.; Apaydin, D. H.; Park, S. Y.; Sariciftci, N. S. An Electron-Reservoir Re(I) Complex for Enhanced Efficiency for Reduction of CO2 to CO. *J. Catal.* **2018**, *363*, 191–196. https://doi.org/10.1016/j.jcat.2018.04.028.

(88) Lang, P.; Pfrunder, M.; Quach, G.; Braun-Cula, B.; Moore, E. G.; Schwalbe, M. Sensitized Photochemical CO 2 Reduction by Hetero-Pacman Compounds Linking a Re I Tricarbonyl with a Porphyrin Unit. *Chem. - A Eur. J.* **2019**, *25* (17), 4509–4519. https://doi.org/10.1002/chem.201806347.

(89) Liyanage, N. P.; Yang, W.; Guertin, S.; Sinha Roy, S.; Carpenter, C. A.; Adams, R. E.; Schmehl, R. H.; Delcamp, J. H.; Jurss, J. W. Photochemical CO 2 Reduction with Mononuclear and Dinuclear Rhenium Catalysts Bearing a Pendant Anthracene Chromophore. *Chem. Commun.* **2019**, *55* (7), 993–996. https://doi.org/10.1039/C8CC09155B.

(90) Shirley, H.; Sexton, T. M.; Liyanage, N. P.; Palmer, C. Z.; McNamara, L. E.; Hammer, N. I.; Tschumper, G. S.; Delcamp, J. H. Effect of “X” Ligands on the Photocatalytic Reduction of CO 2 to CO with Re(PyridylNHC-CF 3)(CO) 3 X Complexes. *Eur. J. Inorg. Chem.* **2020**, No. 19, 1844–1851. https://doi.org/10.1002/ejic.202000283.

(91) Hori, H.; Johnson, F. P. A.; Koike, K.; Ishitani, O.; Ibusuki, T. Efficient Photocatalytic CO2 Reduction Using [Re(Bpy) (CO)3{P(OEt)3}] +. *J. Photochem. Photobiol. A Chem.* **1996**, *96* (1–3), 171–174. https://doi.org/10.1016/1010-6030(95)04298-9.

(92) Koike, K.; Hori, H.; Ishizuka, M.; Westwell, J. R.; Takeuchi, K.; Ibusuki, T.; Enjouji, K.; Konno, H.; Sakamoto, K.; Ishitani, O. Key Process of the Photocatalytic Reduction of CO 2 Using [Re(4,4'-X 2 -Bipyridine)(CO) 3 PR 3] + (X = CH 3 , H, CF 3 ; PR 3 = Phosphorus Ligands): Dark Reaction of the One-Electron-Reduced Complexes with CO 2 . *Organometallics* **1997**, *16* (26), 5724–5729. https://doi.org/10.1021/om970608p.

(93) Hori, H.; Ishihara, J.; Koike, K.; Takeuchi, K.; Ibusuki, T.; Ishitani, O. Photocatalytic Reduction of Carbon Dioxide Using [Fac-Re(Bpy)(CO)3(4-Xpy)]+ (Xpy = Pyridine Derivatives). *J. Photochem. Photobiol. A Chem.* **1999**, *120* (2), 119–124. https://doi.org/10.1016/S1010-6030(98)00430-4.

(94) Kurz, P.; Probst, B.; Spingler, B.; Alberto, R. Ligand Variations in [ReX(Diimine)(CO)3] Complexes: Effects on Photocatalytic CO2 Reduction. *Eur. J. Inorg. Chem.* **2006**, No. 15, 2966–2974. https://doi.org/10.1002/ejic.200600166.

(95) Tsubaki, H.; Sugawara, A.; Takeda, H.; Gholamkhass, B.; Koike, K.; Ishitani, O. Photocatalytic Reduction of CO2 Using Cis,Trans-[Re(Dmbpy)(CO)2(PR3)(PR'3)]+ (Dmbpy=4,4'-Dimethyl-2,2'-Bipyridine). *Res. Chem. Intermed.* **2007**, *33* (1–2), 37–48. https://doi.org/10.1163/156856707779160771.

(96) Andrade, G. A.; Pistner, A. J.; Yap, G. P. A.; Lutterman, D. A.; Rosenthal, J. Photocatalytic Conversion of CO2 to CO Using Rhenium Bipyridine Platforms Containing Ancillary Phenyl

or BODIPY Moieties. *ACS Catal.* **2013**, *3* (8), 1685–1692. https://doi.org/10.1021/cs400332y.

(97) Rotundo, L.; Azzi, E.; Deagostino, A.; Garino, C.; Nencini, L.; Priola, E.; Quagliotto, P.; Rocca, R.; Gobetto, R.; Nervi, C. Electronic Effects of Substituents on Fac-M(Bpy-R)(CO)3 (M = Mn, Re) Complexes for Homogeneous CO2 Electroreduction. *Front. Chem.* **2019**, *7* (JUN), 417. https://doi.org/10.3389/fchem.2019.00417.

(98) Loewen, N. D.; Neelakantan, T. V.; Berben, L. A. Renewable Formate from C–H Bond Formation with CO2: Using Iron Carbonyl Clusters as Electrocatalysts. *Acc. Chem. Res.* **2017**, *50* (9), 2362–2370. https://doi.org/10.1021/ACS.ACCOUNTS.7B00302.

(99) Cluff, D. B.; Arnold, A.; Fettinger, J. C.; Berben, L. A. Electrocatalytic Reduction of CO2 into Formate with Glassy Carbon Modified by [Fe4N(CO)11(PPh2Ph-Linker)]−. *Organometallics* **2018**, *38* (6), 1230–1235. https://doi.org/10.1021/ACS.ORGANOMET.8B00396.

(100) Cunningham, D. W.; Yang, J. Y. Kinetic and Mechanistic Analysis of a Synthetic Reversible CO2/HCO2− Electrocatalyst. *Chem. Commun.* **2020**, *56* (85), 12965–12968. https://doi.org/10.1039/D0CC05556E.

(101) Hasegawa, E.; Nakamura, S.; Oomori, K.; Tanaka, T.; Iwamoto, H.; Wakamatsu, K. Competitive Desulfonylative Reduction and Oxidation of α-Sulfonylketones Promoted by Photoinduced Electron Transfer with 2-Hydroxyaryl-1,3-Dimethylbenzimidazolines under Air. *J. Org. Chem* **2021**, *86*, 47. https://doi.org/10.1021/acs.joc.0c02666.

(102) Wu, Y.; Jiang, Z.; Lin, Z.; Liang, Y.; Wang, H. Direct Electrosynthesis of Methylamine from Carbon Dioxide and Nitrate. *Nat. Sustain.* **2021**, *4* (8), 725–730. https://doi.org/10.1038/s41893-021-00705-7.

(103) Soroceanu, M.; Constantin, C. P.; Damaceanu, M. D. Polynaphthylimide–Azomethines Containing Triphenylamine or Carbazole Moieties with Tuned Optoelectronic Properties through Molecular Design. *Molecules* **2022**, *27* (18). https://doi.org/10.3390/molecules27185761.

Chapter 3. Synthesis, Characterization, and Imaging of Fluoroplatin: a Pro-drug for Fluorescence Detection of Aquated Cisplatin

Work in this chapter was prepared by the author unless noted otherwise. All HRMS was done by Dr. Ebbing De Jong at Upstate Medical University. All *in vivo* work was done by Dr. Tito Borner at the University of Pennsylvania. ^{195}Pt NMR was done by Dr. Deborah Kerwood.

3.1 Synthesis of oxoplatin and fluoroplatin

Oxoplatin and fluoroplatin were synthesized as adapted from literature[34], shown below (**Scheme 3-1**) and detailed in Chapter 5.

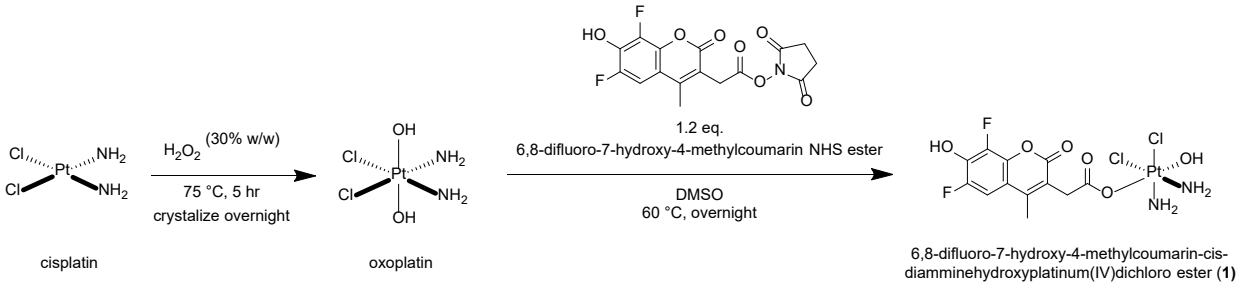

Scheme 3-1. Synthesis of oxoplatin and fluoroplatin

3.2 **1** was stable in aqueous buffer over 24 hours

Over the course of 24 hours, **1** was dissolved in Hank's Balanced Salt solution (HBSS) with or without D-glucose and analyzed by RP-HPLC. The solution of **1** in traditional HBSS with D-glucose supplementation resulted in a new peak observed at an earlier retention time possibly due to the formation of a Pt(IV)-glucose conjugate. It is understood that **1**, as well as cisplatin and other related complexes typically have many off-target interactions that reduce

their *in vivo* potency. Platinum is also known to oxidize glucose and is initiated by glucose adsorption onto platinum[104]. Consequently, the omission of D-glucose resulted no observable side products (**Figure 5-40**). To prevent the formation of side products in subsequent reactions henceforth, HBSS was used without D-glucose.

3.3 **1** had favorable fluorescent properties.

The electronic absorbance of **1** (30 mM) was measured in HBSS and the absorption maximum was found to be 363 nm (**Figure 5-41**). The fluorescence excitation and emission profiles were collected for **1** resulting in λ_{Ex} = 359 and λ_{Em} = 459, consistent with a large stokes shift of 100 nm, which is beneficial for reducing overlap between the excitation and emission wavelength and hence background interference (**Figure 5-42**).

3.4 Reduction of **1** by GSH lead to the production of **2.**

A reaction mixture of **1** and GSH was monitored by RP-HPLC and followed **Scheme 3-2**. Upon initial mixture, **1** had a retention time of ~6.7 min and the reduction product, 6,8-difluoro-7-hydroxy-4-methylcoumarin carboxylic acid (**2**), had a weak signal at ~8.0 min. Over time, the signal of **1** decreased and that of **2** increased (**Figure 5-43**). That peak was collected, analyzed by HRMS, and the expected mass of **2** was detected ($[M+H]^+$: expected, 271.20; observed, 271.04, **Figure 5-44**).

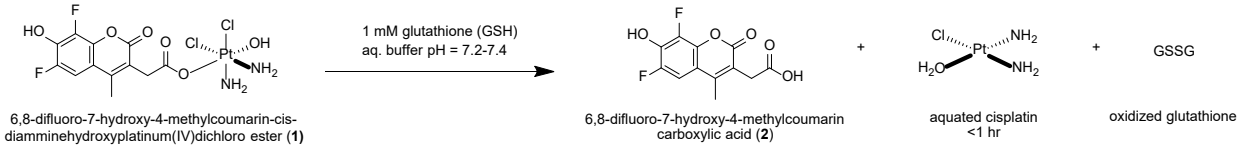

Scheme 3-2. Reduction of **1** via GSH to **2**, **3**, and oxidized GSH.

3.5 Reduction of **1** by GSH lead to an increase in emission intensity.

The addition of GSH to **1** lead to an increase in fluorescence intensity over the course of 3 hours (**Figure 3-1**). The observed increase in both excitation and emission maxima was consistent with the release of reduced fluorophore, **2**, from the quenching effects of platinum binding.

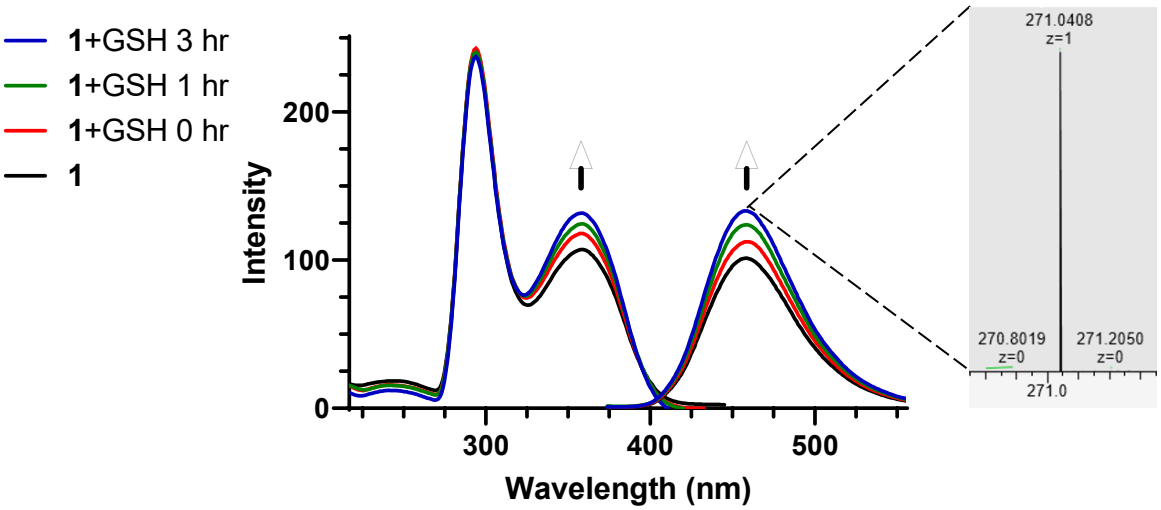

Figure 3-1. Fluorescence excitation and emission of 1 (2 mM) in HBSS with the addition of 1 mM GSH at 0, 1, and 3 hours with insert showing HRMS of 2. Emission spectra were collected at an excitation wavelength of 363 nm and 5 mm slit widths. The full HRMS spectrum can be found in **Figure 5-44**.

3.6 **1** accumulated primarily in the nucleus.

After one hour of incubation with **1**, internalization into HEK-293 cells was observed and a z-projection was produced to confirm internalization rather than surface localization (**Figure 3-2**). Colocalized with the nuclear stain, RedDot 1, **1** was observed primarily in the nucleus of the cell with some residual signal in the cytosol.

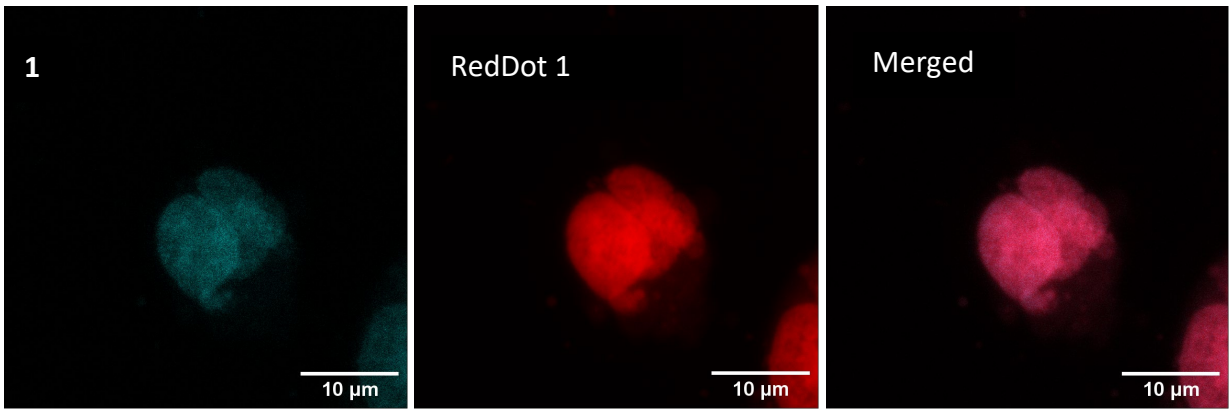

Figure 3-2. Fluorescence confocal microscopy of HEK-293 cells incubated with 1 (10 µM, blue) for 1 hour and stained for nuclei (RedDot 1, red) obtained by a 20 µm depth z-stack (0.21 µm interval) on DAPI and Cy-5 filter presets (scale bar, 10 µm). Images were visualized on a Zeiss LSM980 confocal microscope (63x oil objective).

3.7 Anti-proliferative activity of 1 versus cisplatin was comparable.

The effect of **1** towards cell viability of the human cell line HEK-293 was compared to that of cisplatin with a dose dependent decrease in cell viability observed for both **1** and cisplatin (**Figure 3-3**). After 5 hours of drug exposure and 19 hours of recovery in fresh media, the cells exposed to the highest dose of drug (50 µM) had 86.5% and 61.2% viability corresponding to **1** and cisplatin, respectively. **1** induced cell death as measured by loss of proliferative activity in a similar trend to cisplatin consistent with **1** forming the intracellular aquated species akin to cisplatin.

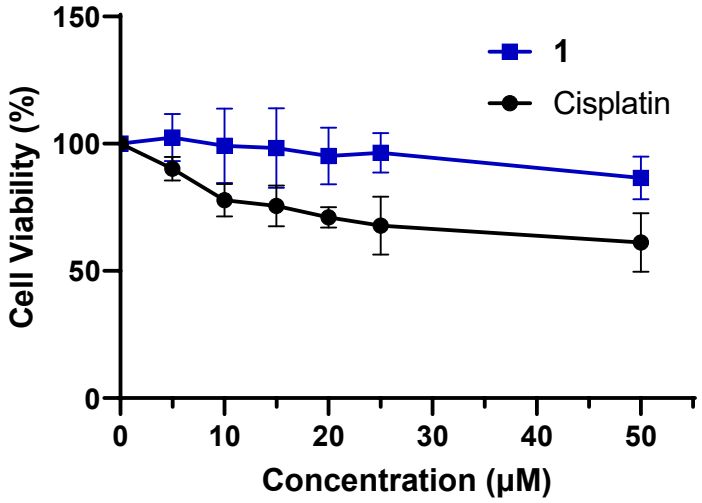

Figure 3-3. Concentration dependance of **1** and cisplatin on cytotoxicity in HEK-293 cultures. Cells were incubated with 5% CO_2 and at 37 °C with Pt complex at 0—50 μM for 5 hours, refreshed with drug-free media, and allowed to recover for 19 hours. Cells were then incubated with CCK-8 reagent for an additional 2 hours and assayed for cell viability at 450 nm.

3.8 Conclusion

Herein, we described the preparation and characterization of a Pt(IV) prodrug, which was designed to reduce into the colocalized fluorophore, **2** , and aquated cisplatin, **3**. **1** was stable in buffered aqueous media showing no degradation over 24 hours when incubated at 37 °C. In a model intracellular environment of 1 mM GSH, reduction of **1** was supported by an increase in fluorescence emission as well as the elution of **2** via RP-HPLC, which was confirmed by HRMS. Confocal microscopy supported cellular internalization of **1** with localization primarily in the nucleus. Furthermore, **1** was traceable via DAPI filter presets, thus exemplifying its ease of use and practicality for further studies. With its aqueous stability, rapid cellular uptake, and facile imaging, **1** is a suitable tool for verifying localization of *in vivo* and *ex vivo* cisplatin. By

developing new methods to track and image cisplatin, we may discover DEGs in the affected tissues.

3.9 Future Directions

After the development and characterization of the fluorescent pro-probe, **1**, *in vivo* experiments were required to assess its activity in animal models and transcriptional affects post-administration. This work is ongoing in the labs of Professors Matthew R. Hayes, Bart C. De Jonghe, and Ben Reiner at the University of Pennsylvania (Philadelphia, PA, USA). Food intake and kaolin intake studies will be conducted to ascertain the degree of malaise and nausea in rodent models. The pseudo-primate *Suncus maurinus* (musk shrews) will be utilized to measure emetic behaviors post-administration of **1**. All studies will be performed alongside a cisplatin control. After administration of **1** into the 4th ventricle of rats to target the AP-NTS, the animals will be sacrificed, and tissues collected to undergo fluorescence microscopy and 10x snRNAseq. Finally, tissue samples will be subject to lysis, homogenization, and ICP-MS to further validate the localization of Pt in specific neuronal populations.

3.10 References

(104) Vassilyev, Y. B.; Khazova, O. A.; Nikolaeva, N. N. Kinetics and Mechanism of Glucose Electrooxidation on Different Electrode-Catalysts. *J. Electroanal. Chem. Interfacial Electrochem.* **1985**, *196* (1), 105–125. https://doi.org/10.1016/0022-0728(85)85084-1.

Chapter 4. Rapid, green disulfide bond formation in water using the corrin dicyanocobinamide

Work in this chapter was prepared by the author unless noted otherwise. All HRMS was done by Dr. Ebbing De Jong at Upstate Medical University. CV was done by Dr. Adam Henwood at Trinity College Dublin. The work reported in this chapter resulted in the following publication awaiting peer review:

- **Spear, A**.; Orativskyi, O.; Tran, S.; Zubieta, J. A.; Doyle, R. P. Rapid, green disulfide bond formation in water using the corrin dicyanocobinamide. *Chem. Commun.* Submitted June 1, 2023.

4.1 Detailed oxidation reaction with model substrate OT

As a model substrate, a modified oxytocin (**OT**) was used for detailed screening of Cbi. **OT** incorporates an azido-modified lysine at position 8 and is frequently synthesized in our lab. An equimolar amount of peptide was combined with 2 mg Cbi in 2 mL of 20 mM HEPES solution (pH = 7). The reaction was done in a 20 mL clear glass vial open to air with stirring. After 30 minutes of reaction, HPLC was performed to detect a retention time shift of 7.629 to 7.506 min. To validate the HPLC results, the eluted peptide was collected, lyophilized, and redissolved in an aqueous solution of dithiothreitol (DTT, 10 mM), a strong reducing agent. The retention time was observed to revert to that of the reduced peptide (7.629 min, **Figure 5-47**).

Purification was achieved by simple HPLC methods as provided in the supplemental materials for all peptides screened. Lyophilized powders of the isolated reduced and oxidized

peptides, as well as DTT-treated peptides in solution, were subject to HRMS (**Figure 5-48**). The appropriate masses were observed for **OT** (reduced = 1050.4578 m/z; oxidized = 1048.4439 m/z; z=1) and the loss of two hydrogens indicative of oxidation. The DTT treated peptide also displayed the expected mass of the reduced peptide (1050.4591 m/z; z=1).

4.2 Cbi construct is required for catalysis

To determine the necessity of Cbi as metal catalyst, $Co(II)Cl_2$ was employed as an analogue of the reduced metal center. $Co(II)Cl_2$ and peptide were combined at equimolar concentrations in 1 mL H_2O and the retention time of the peptide was tracked as described previously. $Co(II)Cl_2$ did not oxidize the peptides under the conditions used. Furthermore, when B_{12} was introduced as a catalyst under the same conditions, oxidation was not observed over the course of 48 hours, suggesting a strong influence from the axial ligands (**Figure 5-49**).

4.3 Cbi catalyzed the aerobic oxidation of a library of peptides with regioselectivity

Cbi was then tested as a catalyst for oxidative disulfide formation in a library of peptides with varying lengths and number of disulfides (**Table 4-1**). Full peptide HPLC chromatograms and mass spectra can be found in the supplemental information. The single disulfide containing peptides consisted of **OT**, vasopressin (**AVP**), and somatostatin (**SST**). **OT** produced the sharpest line peaks, distinct shift in elution times (7.629 to 7.506 min), and shortest conversion time of 30 min. **AVP**, while similar in sequence to **OT**, had broader line peaks and took 90 min to convert, exemplified by a slight elution time shift of 6.494 to 6.527 (**Figure 5-51**). **SST** also produced sharp line peaks but did not show any shift in elution time over the course of

oxidation with either DMSO or Cbi (**Figure 5-56**, **Figure 5-57**). Rather than determining time of oxidation via HPLC, reactions were allowed to run over 48 hours, purified, lyophilized and subject to HRMS. **SST** displayed the appropriate mass for its oxidized form in 1 hour upon reaction with Cbi and 48 hours with DMSO (**Figure 5-59**). The double disulfide containing peptide endothelin-1 (**ET-1**) was also studied and found to oxidize after 1 hour of reaction with Cbi (**Figure 5-60**, **Figure 5-61**). Commercial controls of **AVP**, **SST**, and **ET-1** were bought in to further validate the HPLC retention times (**Figure 5-50**, **Figure 5-58**, **Figure 5-61**).

Table 4-1. Disulfide bond formation of peptides using DMSO or Cbi.

Peptide	Disulfides (amt)	Conversion Time (min)	
		DMSO	Cbi
OT	1	2880	30
OT	1	-	50[a]
OT	1	-	1560[b]
OT	1	-	2880[c]
AVP	1	2880	90
AVP	1	-	243[d]
SST	1	2880	60
ET-1	2	2880	60
***Tr*CART-1**	1	1440	60
***Tr*CART-2**	2	2880	60
***Tr*CART-3**	3	2880	60

All reactions were performed in air with 10% DMSO or 1 mol equiv of Cbi with respect to peptide with the following exceptions: [a] 0.5 mol equiv; [b] 0.1 mol equiv; [c] 1 mol equiv of $Co(II)Cl_2$; [d] degassed water under argon.

***Tr*CART-(1-3)** are a series of cocaine and amphetamine related transcript (CART) analogues derived from the *Takifugu rubripes* sequence. Each iteration of the analogue peptides incorporates a larger portion of the sequence and an increasing amount of disulfide

bonds. ***Tr*CART-(1-3)** were oxidized by Cbi within an hour while DMSO required 24-48 hours (**Figure 5-62**-**Figure 5-74**). ***Tr*CART-2** and **3** were subject to tryptic digest to determine the bound cysteines. ***Tr*CART-2** was predicted to contain disulfides at C4-22 and C10-24, the latter being the appropriate linkage for the native human CART (hCART). After digestion, the ionized species of the major fragment was detected (M=1670.7388; m/z 418, z=4; 557, z=3; 836, z=2) (**Figure 5-70**). ***Tr*CART-3** was predicted to have disulfide linkages at C4-22, C10-30, and C24-37, all corresponding to the folding pattern of hCART and supported by HRMS. The digested fragments of 1628.7 (543.9301, z=3) and 1529.77 (765.8832, z=2) were observed (**Figure 5-74**). In both cases, the hydrophobicity of the peptide led to precipitation and faint signals during HRMS and trypsin digestion, especially for the fully oxidized peptides lacking free thiols.

4.4 Putative mechanism

The putative mechanism is air-oxidation catalyzed by Cbi and is consistent with literature detailing nonenzymatic protein folding[43,105]. To support this, reactions were prepared in smaller, narrower vials to reduce the surface area of the headspace-solution interface, purged the vessels in argon, and capped the vessels. The water used in the reaction was additionally degassed by three rounds of freeze-pump-thaw. **AVP** was reacted under these conditions with Cbi resulting in a conversion time of 4 hours as opposed to 90 minutes in air, however residual air was introduced when the auto sampling needle punctured the septum over recurring experiments (**Figure 5-52**). Oxidation via atmospheric O_2, as opposed to Cbi itself, is further supported when considering reduction potentials, Cbi was measured herein (**Figure 5-54**) to have a reduction potential of -1.5 V vs $Fc^{+/0}$ in DMF, while O_2 has a reported potential of +0.6 V under the same reference and solvent[106]. It is hypothesized that Cbi is

playing a role in activating molecular oxygen[107] to form the sulfenic acid species of the peptide though more time-resolved experiments are needed to support this hypothesis. The last step of the mechanism is a condensation reaction between the -SH and -SOH groups resulting in the bridged peptide and H_2O (Scheme 4-1).

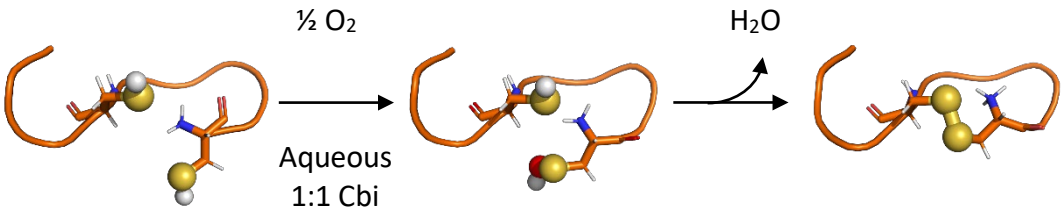

Scheme 4-1. Proposed mechanism of Cbi-catalyzed air-oxidation of cysteine residues to a cystine bond.

4.5 Cbi catalyzed aerobic oxidation of disulfides produced functional peptides

To confirm functionality post Cbi oxidation, **OT** was screened, both free and after conjugation to B_{12}, at the oxytocin receptor with equipotent agonism recorded (K_D = 4.39 and 4.63 nM, respectively)[108].

4.6 Conclusion

In conclusion, Cbi is a powerful catalyst for the oxidation of cysteine residues in peptides synthesized via SPPS. Cbi can be synthesized from vitamin B_{12} or purchased commercially. When synthesized from B_{12}, assuming 92% literature yield[109], and running at a 2 mg scale, these reactions cost $0.27 per reaction with respect to the catalyst; alternatively, when Cbi is

purchased directly, the cost is $41.80 per reaction. The system is facile and green, requiring water and air. Complete conversion is observed in 1 hour or less for most peptides. Catalysis with Cbi was shown to impart regioselectivity in ***Tr*CART-2** and **3,** implying that the cobalt-bound construct was able to stabilize or direct folding towards the thermodynamic product within the short time span of 1 hour. Further *in silico* modelling and time-resolved spectroscopy is needed to describe the interaction between peptide, molecular oxygen, and Cbi. This method provides chemists a rapid, aqueous route to achieve the oxidized forms of peptides with a commercially available, green oxidant.

4.7 Future directions

To expand substrate scope and accessibility, other methods of purification are being explored. PD-10 desalting columns may provide a cheap and simple route for separating Cbi from peptides after catalysis. The use of these columns will also serve research laboratories without access to an HPLC. Further mechanistic studies are also needed to elaborate on the interaction between Cbi, molecular oxygen, and peptides.

4.7.1 ***Tr*CART** for the development of stroke therapeutics

CART is a neuropeptide with agonism at the recently deorphanized GPR-160[110]. Literature suggests CART and its peptide fragments may have neuroprotective and neuroregenerative effects in post-ischemic injury in rats[111]. The ***Tr*CART1-3** peptides based on the sequence of *Takifugu rubripes* was synthesized by SPSS, oxidized via Cbi catalysis, and characterized via RP-HPLC and HRMS. Docking studies will be conducted to gauge ***Tr*CART1-3** binding at GPR-160 with comparison to human CART. Subsequent ant/agonism experiments will

be conducted on SPR to support the *in-silico* results. In collaboration with Dr. Tito Borner from the lab of Professor Matthew Hayes at the University of Pennsylvania, food intake reduction studies will be conducted in rats with the ***Tr*CART1-3** peptides and the native CART control. Finally, the performance of these analogues in an animal model of ischemic stroke will be explored.

4.8 References

(105) Rehder, D. S.; Borges, C. R. Cysteine Sulfenic Acid as an Intermediate in Disulfide Bond Formation and Nonenzymatic Protein Folding. *Biochemistry* **2010**, *49* (35), 7748–7755. https://doi.org/10.1021/bi1008694.

(106) Pegis, M. L.; Roberts, J. A. S.; Wasylenko, D. J.; Mader, E. A.; Appel, A. M.; Mayer, J. M. Standard Reduction Potentials for Oxygen and Carbon Dioxide Couples in Acetonitrile and N , N -Dimethylformamide. *Inorg. Chem.* **2015**, *54* (24), 11883–11888. https://doi.org/10.1021/acs.inorgchem.5b02136.

(107) Huang, W.-F.; Chang, S.-T.; Huang, H.-C.; Wang, C.-H.; Chen, L.-C.; Chen, K.-H.; Lin, M. C. On the Reduction of O 2 on Cathode Surfaces of Co–Corrin and Co–Porphyrin: A Computational and Experimental Study on Their Relative Efficiencies in H 2 O/H 2 O 2 Formation. *J. Phys. Chem. C* **2020**, *124* (8), 4652–4659. https://doi.org/10.1021/acs.jpcc.0c00481.

(108) Asker, M.; Krieger, J. P.; Liles, A.; Tinsley, I. C.; Borner, T.; Maric, I.; Doebley, S.; Furst, C. D.; Börchers, S.; Longo, F.; et al. Peripherally Restricted Oxytocin Is Sufficient to Reduce Food Intake and Motivation, While CNS Entry Is Required for Locomotor and Taste

Avoidance Effects. *Diabetes, Obes. Metab.* **2023**, *25* (3), 856–877. https://doi.org/10.1111/dom.14937.

(109) Ó Proinsias, K.; Karczewski, M.; Zieleniewska, A.; Gryko, D. Microwave-Assisted Cobinamide Synthesis. *J. Org. Chem.* **2014**, *79* (16), 7752–7757. https://doi.org/10.1021/jo501364b.

(110) Yosten, G. L. C.; Harada, C. M.; Haddock, C.; Giancotti, L. A.; Kolar, G. R.; Patel, R.; Guo, C.; Chen, Z.; Zhang, J.; Doyle, T. M.; et al. GPR160 De-Orphanization Reveals Critical Roles in Neuropathic Pain in Rodents. *J. Clin. Invest.* **2020**, *130* (5), 2587–2592. https://doi.org/10.1172/JCI133270.

(111) Luo, Y.; Shen, H.; Liu, H.-S.; Yu, S.-J.; Reiner, D. J.; Harvey, B. K.; Hoffer, B. J.; Yang, Y.; Wang, Y. CART Peptide Induces Neuroregeneration in Stroke Rats. *J. Cereb. Blood Flow Metab.* **2013**, *33* (2), 300–310. https://doi.org/10.1038/jcbfm.2012.172.

Chapter 5. Experimental

5.1 Chapter 2 Experimental

5.1.1 General methods and instrumentation

Chloropentacarbonyl rhenium(I), bromopentacarbonyl rhenium(I), 1,10-phenanthroline-5- amine, 4-nitro-1,8-naphthalic anhydride, 2- phenylbenzimidazole, iodomethane, sodium borohydride, sulfuric acid, diethyl ether, potassium bromide (KBr), triethylamine, $CDCl_3$, CD_3OD and DMSO-d6 NMR solvents were all purchased through Sigma Aldrich (Milwaukee, WI, USA). Sodium hydroxide was purchased through Fisher Scientific (Agawam, MA, USA). Acetonitrile, methanol, ethanol, and dichloromethane were purchased through Sigma Aldrich and subsequently dried over 4 Å molecular sieves in-house before use. Barium carbonate (^{13}C, 98%+) was purchased from Cambridge Isotope Laboratories, Inc. (Tewksbury, MA, USA). Reverse osmosis grade water was obtained in-house. A 12 W LED blue light (450–460 nm) was purchased from Abi, USA (Vernon, CA, USA).

Mass Spectrometry of $[Re(H_2O)_2(CO)_3Cl]$ and 5-PAN were conducted on a Shimadzu 8040 mass spectrometer. Mass spectrometry of $[Re(CO)_3(5\text{-PAN})Cl]$ was conducted on a Bruker AutoFlex III MALDI-ToF/ToF Mass Spectrometer and dilutions of $[Re(CO)_3(5\text{-PAN})Cl]$ were made in 1:9 (v:v) MeOH/DCM in the presence of alpha-cyano-4-hydroxycinnamic acid (CHCA) matrix. $^1H/^{13}C$ NMR spectra were conducted on a Bruker Avance III HD 400 MHz instrument and calibrated to the residual $CDCl_3$ signal at 7.24 ppm, D1 = 5s for ^{13}C NMR. FT-IR spectroscopy was carried out on a Nicolet Infrared Spectrophotometer utilizing potassium bromide (KBr) disks. Electronic absorption spectroscopy was conducted on a Varian 50 Bio spectrophotometer.

Excitation and emission spectroscopy was conducted on an Agilent Technologies Cary Eclipse Fluorescence Spectrophotometer. Raman spectra were collected using a fiber-coupled i-Raman Plus spectrometer (B&W Tek, Newark DE) with an excitation wavelength of 785 nm. Final spectra are the product of 100 averages of 1 s integration windows and have a spectral resolution of ~4 cm^{-1}. The Raman spectral intensities have been normalized to one. All samples that required centrifugation were centrifuged utilizing a Thermo Electronic Corporation Sorvall® Legend RT centrifuge and were centrifuged at 4000 rpm for 5–10 minutes. Gas chromatography (GC) was conducted on an HP-6890 instrument with a ShinCarbon packed column (Restek, PA, USA), a Flame Ionization Detector (FID), and a methanizer. The FID was calibrated with the standards 1% CO in helium, 1% CO_2 in helium, and 0.5% CH_4 in helium (Airgas). All injections were done with a calibrated 1 mL syringe (Agilent). Elemental Analysis and ion chromatography were conducted by Intertek Pharmaceuticals (Whitehouse, NJ, 08888).

5.1.1 Synthesis of $Re(H_2O)_3(CO)_3X$

Chloropentacarbonyl rhenium(I) (8.45 mmol, 3.0551 g) was dissolved in 50 mL of water in a 100 mL round bottom flask. The solution was left to reflux and monitored via TLC (70/30 hexanes/ethyl acetate) until full conversion was observed. The reflux of chloropentacarbonyl rhenium (I) can take up to four days for full conversion. The solvent was removed and the solid dried *in vacuo*. The white/green solid was obtained in ~93% yield (2.5451 g). $[Re(H_2O)_3(CO)_3]Cl$ was characterized by ESI-MS (**Figure 5-1**) and ^{13}C NMR (**Figure 5-2**).

Bromopentacarbonyl rhenium(I) was refluxed in water for 24 hours to produce $[Re(CO)_3(H_2O)_3]Br$ as previously reported in the literature[17].

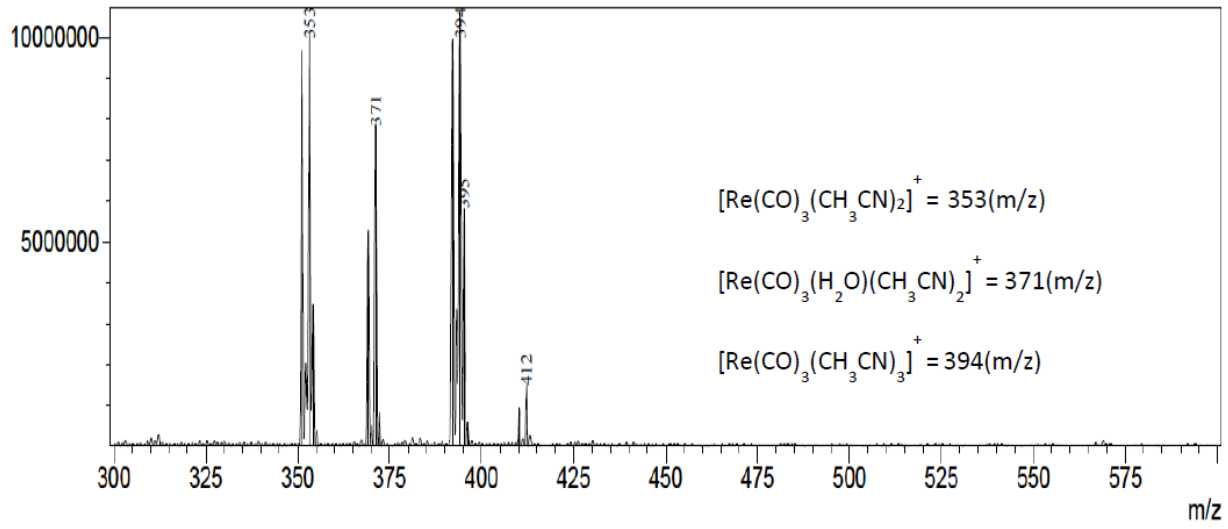

Figure 5-1. ESI-MS of $[Re(CO)_3(H_2O)_3]^+$ dissolved in methanol in the presence of acetonitrile and water with 0.1% TFA. Both the di- and trisubstituted acetonitrile adducts were observed at 353, 371, and 394 m/z, respectively. Expected mass = 324 g/mol.

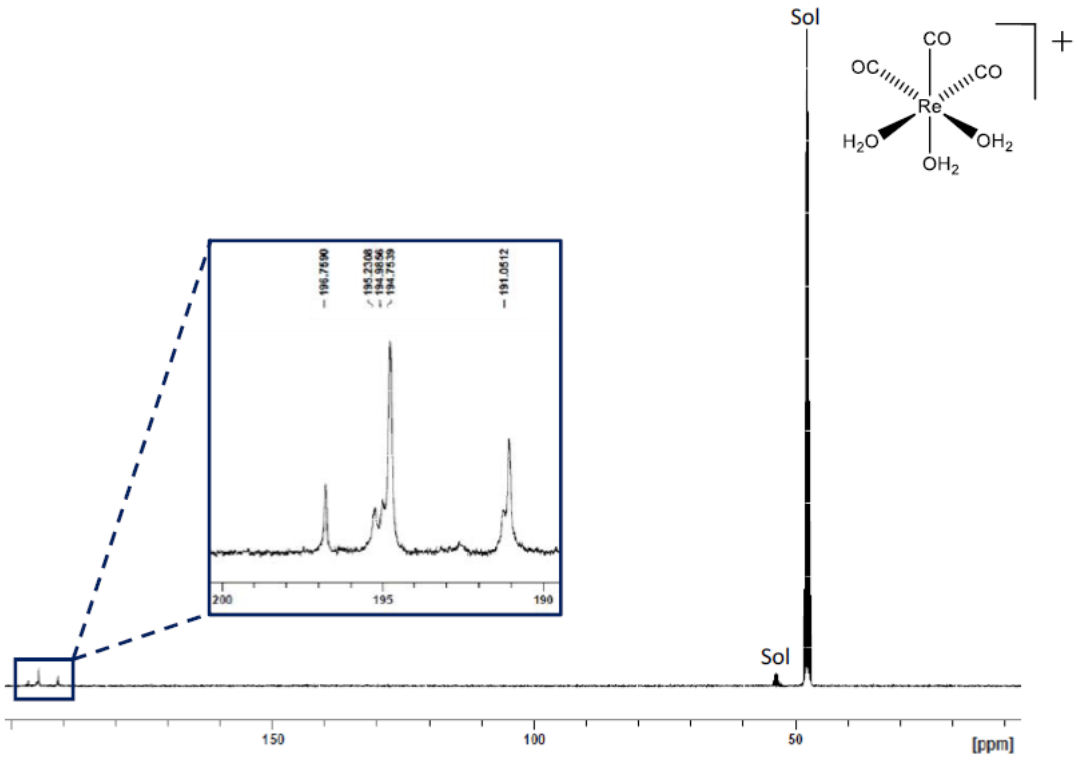

Figure 5-2. ^{13}C NMR of $[Re(CO)_3(H_2O)_3]Cl$ in deuterated methanol (CD_3OD) showing distinct carbonyl peaks between 190 – 200ppm.

5.1.2 Synthesis of 5-PAN

Synthesis of (1-(1,10)-phenanthroline-5-(4-nitro-naphthalimide))(5-PAN), initially reported by *Yarnell et al*.[112,113], was approached utilizing a new synthetic method. 0.429 g (2.2 mmol) of 1,10- phenanthroline-5-amine was suspended in 25 mL of anhydrous ethanol. Simultaneously, a second solution of 0.486 g (2 mmol) of 4-nitro-1,8-naphthalic anhydride was suspended in 25 mL of anhydrous ethanol. Both solutions were combined in a 100 mL round-bottom flask and heated to reflux under argon with stirring. The solution was refluxed for a period of 48 h and the solution was left to cool to room temperature, whereupon a tan colored precipitate was observed. Diethyl ether was then added to ensure complete precipitation of the product. The solution was filtered through a Gooch filter, washed three times with 20 mL of diethyl ether, each time centrifuged at 4000 rpm for 5 minutes, and the ether decanted off; 5-PAN was then dried overnight in vacuo and was massed to 0.364 g (yield ≈44% based on 4-nitro-1,8-naphthalimide). This yield is less than the 67% reported by Yarnell in the presence of acetic acid[112]. 5-PAN was confirmed via ^{1}H NMR (**Figure 5-3**), ^{13}C NMR (**Figure 5-4**), ESI-MS (**Figure 5-5**), and FT-IR (**Figure 5-6**), and fluorescence excitation and emission spectroscopy (**Figure 5-7**).

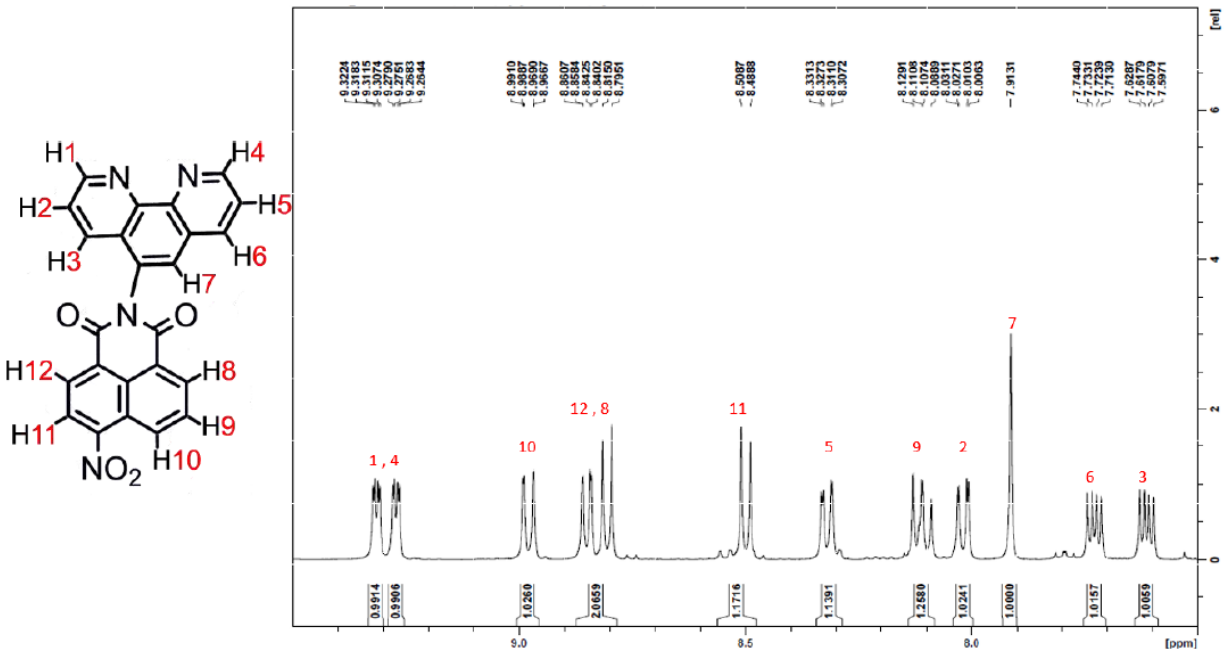

Figure 5-3. ^{1}H NMR spectrum of 5-PAN with zoomed in aromatic region (400 MHz, chloroform-d) δ 9.32-9.31 (dd, 1H), 9.28-9.26 (dd, 1H), 9.00-8.97 (dd, 1H), 8.86-.84 (dd, 1H), 8.82-8.80 (d, J = 8.0 Hz, 1H), 8.51-8.49 (d, J = 8.0 Hz, 1H), 8.33-8.31 (dd, 1H), 8.13-8.09 (dd, 1H), 8.03-8.00 (dd, 1H), 7.91 (s, 1H), 7.74-7.71 (dd, 1H), 7.63-7.60 (dd, 1H).

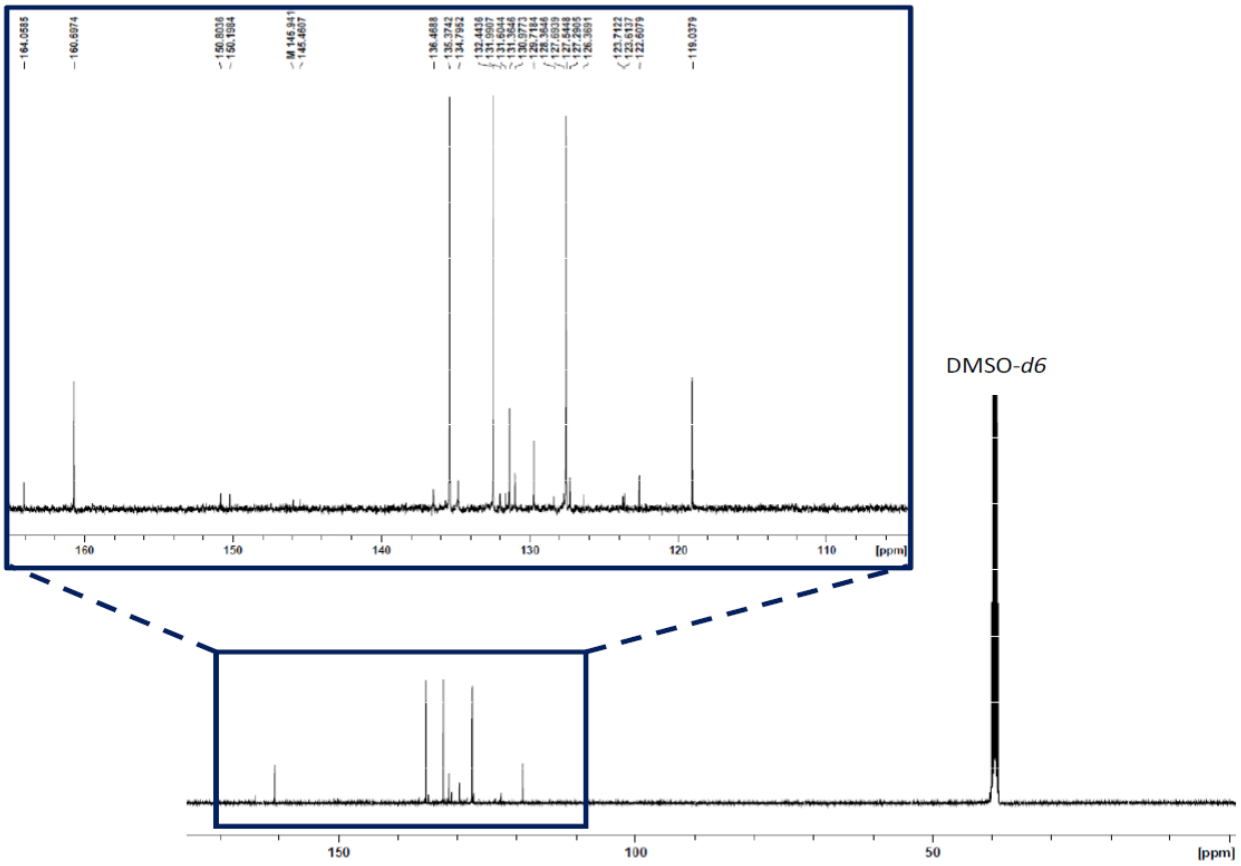

Figure 5-4. ^{13}C NMR of the free 5-PAN ligand acquired in DMSO-d6 showing the appropriate number of 24 carbon signals with the signals beyond 160 being assigned to ketone carbons of the naphthyl core.

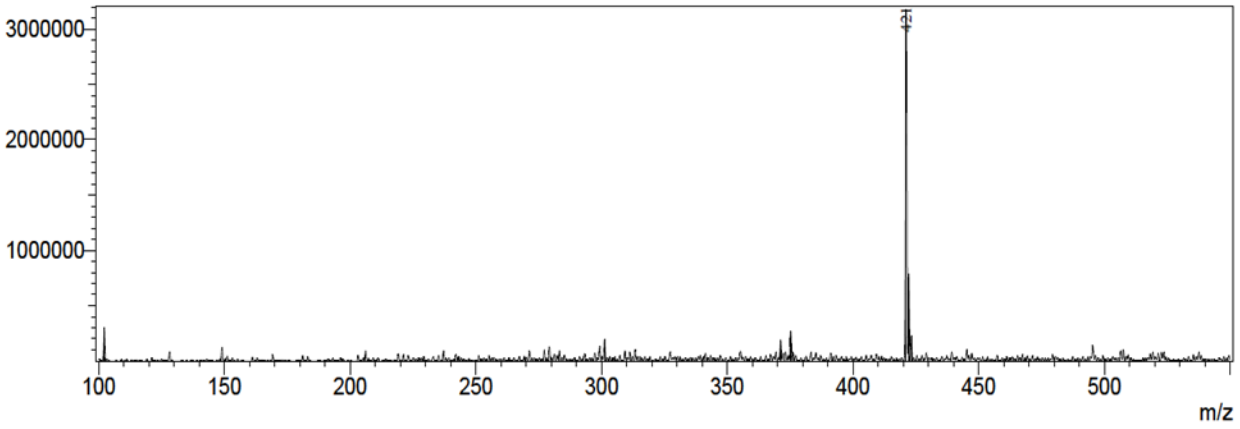

Figure 5-5. ESI-MS of 5-PAN dissolved in DCM and run in the presence of methanol. Expected mass $[M+H]^+$: 421 m/z; observed mass $[M+H]^+$: 421 m/z.

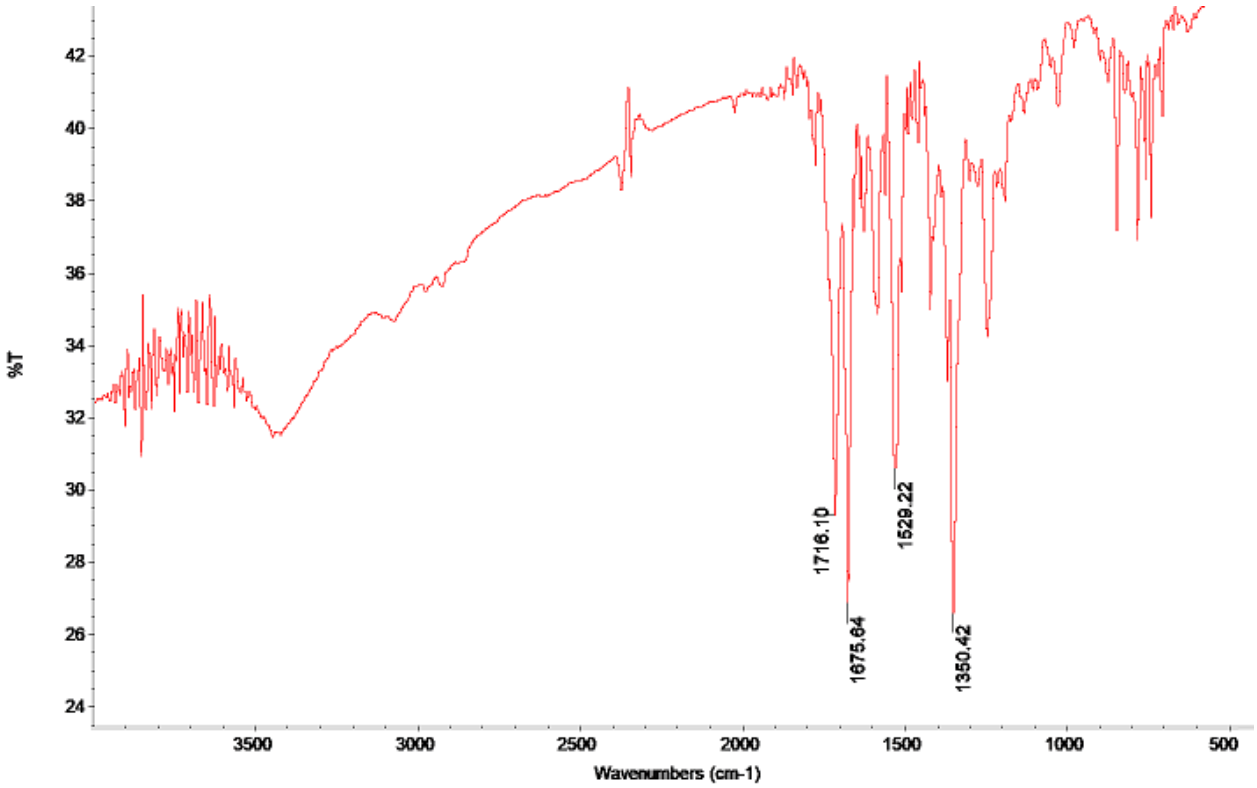

Figure 5-6. FT-IR of 5-PAN (KBr, cm^{-1}): CO-N-CO: 1716.10, C=O: 1675.64, C-NO_2: 1529.22, C-NO_2: 1350.42.

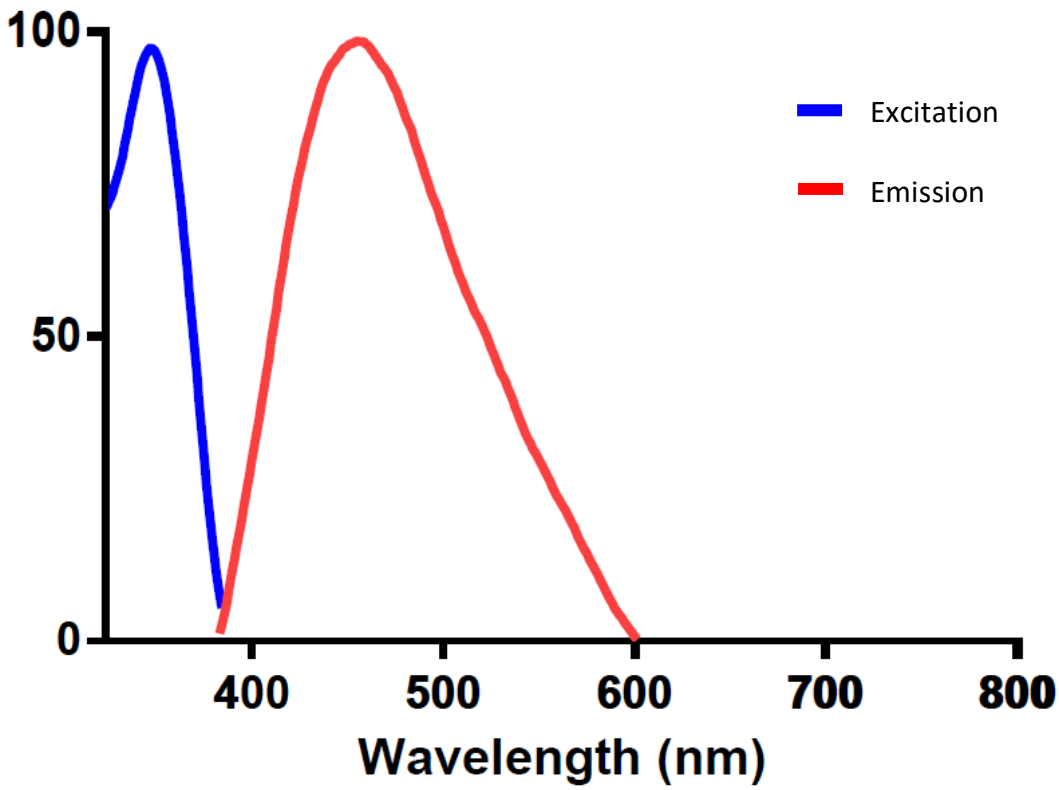

Figure 5-7. Excitation and emission spectra of 5-PAN in 1:9 (v:v) MeOH/DCM showing an excitation λ_{max} of 350 nm and an emission λ_{max} of 456 nm resulting in a Stokes shift of 106 nm.

5.1.3 Synthesis of AFH series

The following compounds were synthesized by the author at Trinity College (Dublin, Ireland) with collaboration from Adam F. Henwood, Ph.D., Louisa C. Sigurvinsson, and Professor Thorfinnur Gunnlaugsson.

***N*-(4-pyridyl)-4-bromo-1,8-naphthalimide (Br-Nap-Py)**: This is a modified procedure of a method previously reported for a similar compound[114]. To a round-bottomed flask containing pre-dried molecular sieves (3 Å) were added 4-bromonaphthalic anhydride (0.250 g, 0.90 mmol, 1.0 equiv.) and 4-aminopyridine (0.119 g, 1.33 mmol, 1.4 equiv.). The flask was evacuated and

backfilled with nitrogen before dry toluene (10 mL) and dry triethylamine (1 mL) were added. The reaction mixture was heated to reflux for 72 h, before filtering hot through celite, and washed with toluene (3 × 25 mL). The toluene was removed under reduced pressure, methanol was added, and the compound filtered. The compound was washed with ether (3 × 10 mL), hexane (3 × 10 mL), and dried to give an off-white solid (0.218 g). Yield: 69%. ^{1}H NMR (600 MHz, $CDCl_3$) δ (ppm): 8.83 (d, *J* = 5.3 Hz, 2H), 8.71 (d, *J* = 7.3 Hz, 1H), 8.68 (d, *J* = 8.5 Hz, 1H), 8.47 (d, *J* = 7.8 Hz, 1H), 8.11 (d, *J* = 7.8 Hz, 1H), 7.91 (t, *J* = 7.9 Hz, 1H), 7.31 (d, *J* = 5.3 Hz, 2H).^{13}C NMR (151 MHz, $CDCl_3$) δ (ppm): 163.2, 163.2, 151.3, 143.2, 134.3, 132.9, 132.0, 131.5, 131.4, 131.0, 129.5, 128.5, 124.1, 122.9, 122.0. MS APCI (m/z): $[M+H]^+$ expected: ($C_{17}H_{10}BrN_2O_2$) 352.9920 observed: 352.9922.

***N*-(4-picolyl)-4-bromo-1,8-naphthalimide (Br-Nap-Pic)**: To a round-bottomed flask containing a suspension of 4-bromonaphthalic anhydride (0.300 g, 1.08 mmol, 1.0 equiv.) and acetic acid (5 mL) was added 4-picolylamine (0.234 g, 2.16 mmol, 2.0 equiv.). The flask was heated to reflux for 18 h, before cooling to room temperature. The reaction mixture was raised to pH 6 with aqueous KOH to facilitate precipitation. The precipitate was filtered and washed with MeOH (3 × 10 mL), ether (3 × 10 mL), and dried to give an off-white solid (0.200 g). Yield: 50%. ^{1}H NMR (400 MHz, $CDCl_3$) δ (ppm): 8.69 (dd, *J* = 7.3, 0.9 Hz, 1H), 8.62 (dd, *J* = 8.5, 0.9 Hz, 1H), 8.54 (d, *J* = 4.6, 1.5 Hz, 2H), 8.44 (d, *J* = 7.9 Hz, 1H), 8.07 (d, *J* = 7.9 Hz, 1H), 7.88 (dd, *J* = 8.4, 7.4 Hz, 1H), 7.37 (d, *J* = 6.0 Hz, 2H), 5.36 (s, 2H).

Optimized synthetic procedure for palladium-catalyzed Suzuki-Miyaura cross-coupling reactions: To a round-bottomed flask with a tap, or a Schlenk tube were added dioxane (ca. 15 mL) and water (ca. 5 mL) in a 3:1 ratio. The solvent mixture was degassed by three freeze-

pump-thaw cycles, before backfilling with N_2. Under positive N_2 pressure, the appropriate arylboronic acid (4-(9H-carbazol-9-yl)phenylboronic acid or (4-diphenylamino)phenylboronic acid, 1.2 equiv., ca. 0.280 g), 4-bromonaphthalimide (1.0 equiv., ca. 0.300 g), K_3PO_4 (2.0 equiv., ca. 0.350 g), $Pd(OAc)_2$ (5 mol%, ca. 0.010 g) and SPhos (10 mol%, ca. 0.030 g) were added to the reaction vessel, and the vessel sealed. The reaction was heated to reflux for 18 h. Distilled water was added, before extracting with three portions of dichloromethane. The organic fractions were combined and washed with brine and saturated aqueous $NaHCO_3$. The organic solvent was dried over $MgSO_4$, before removing under reduced pressure, before purifying by column chromatography (DCM/MeOH gradient 100:0 to 90:10). In all cases, TLC showed elution of two compounds after chromatography: a yellow or red fluorescent band corresponding to the title compound and a blue fluorescent, unidentifiable impurity, which was also present in the ^1H NMR spectra. This impurity could be removed by dissolving the compound in the minimum volume of DCM and adding dropwise to an excess of vigorously stirring ether. The resultant precipitate was stirred for 1 hour, filtered, washed with ether and dried to give the title compound. Yields were in the region of 40-50%.

5.1.4 Synthesis and characterization of $[Re(CO)_3(5\text{-PAN})Cl]$

0.0814 g (0.25 mmol) of $[Re(H_2O)_3(CO)_3]Cl$ was dissolved in 5 mL of CH_3OH/DCM (1:9, v:v) in a 50 mL round-bottom flask. 0.105 g (0.25 mmol) of 5-PAN was then dissolved in 15 mL of CH_3OH/DCM (1:9, v:v) and combined with the solution of $[Re(CO)_3(H_2O)_3]Cl$; the solution was stirred at room temperature for 1.5 h. The MeOH/ DCM (1:9, v:v) azeotrope was selected to aid in the solubility of 5-PAN, which was not soluble in methanol alone, as is $[Re(H_2O)_3(CO)_3]Cl$. After stirring, a yellow solid was precipitated with diethyl ether and dried in vacuo. $[Re(CO)_3$(5-

PAN)Cl] was characterized via MALDI-ToF MS (**Figure 5-8**), electronic excitation and emission spectroscopy (**Figure 5-9**), ^{1}H NMR (**Figure 5-10**), ^{13}C NMR (**Figure 5-11**) FT-IR (**Figure 5-12**), elemental analysis (**Table 5-1**), Raman spectroscopy (**Figure 2-2**), and single crystal X-ray diffraction (**Figure 2-1**).

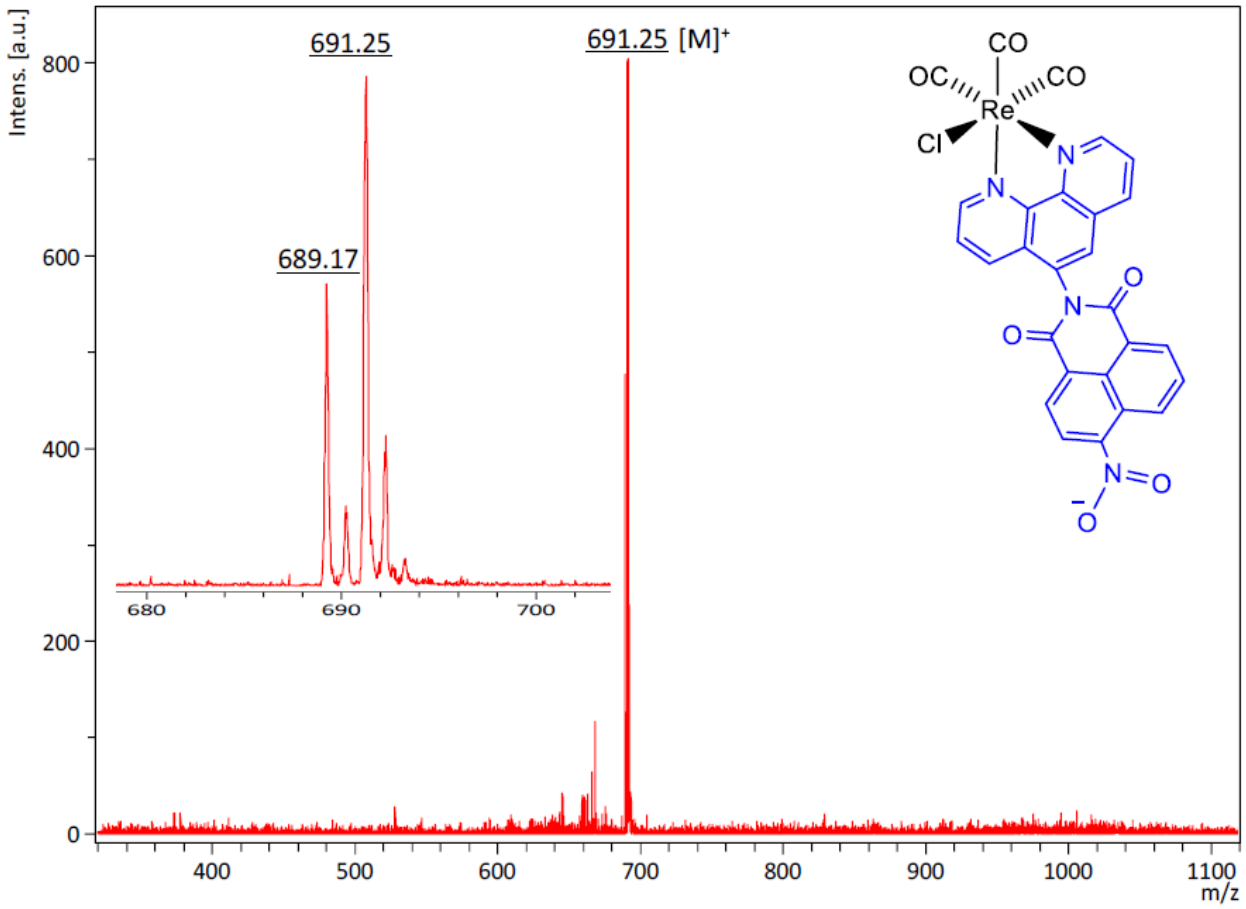

Figure 5-8. MALDI-ToF MS of $[Re(CO)_3(5\text{-PAN})Cl]$ with expected mass (m/z) $[M\text{-}Cl\text{-}H_2O]^+$: 691 and observed mass: 691.25.

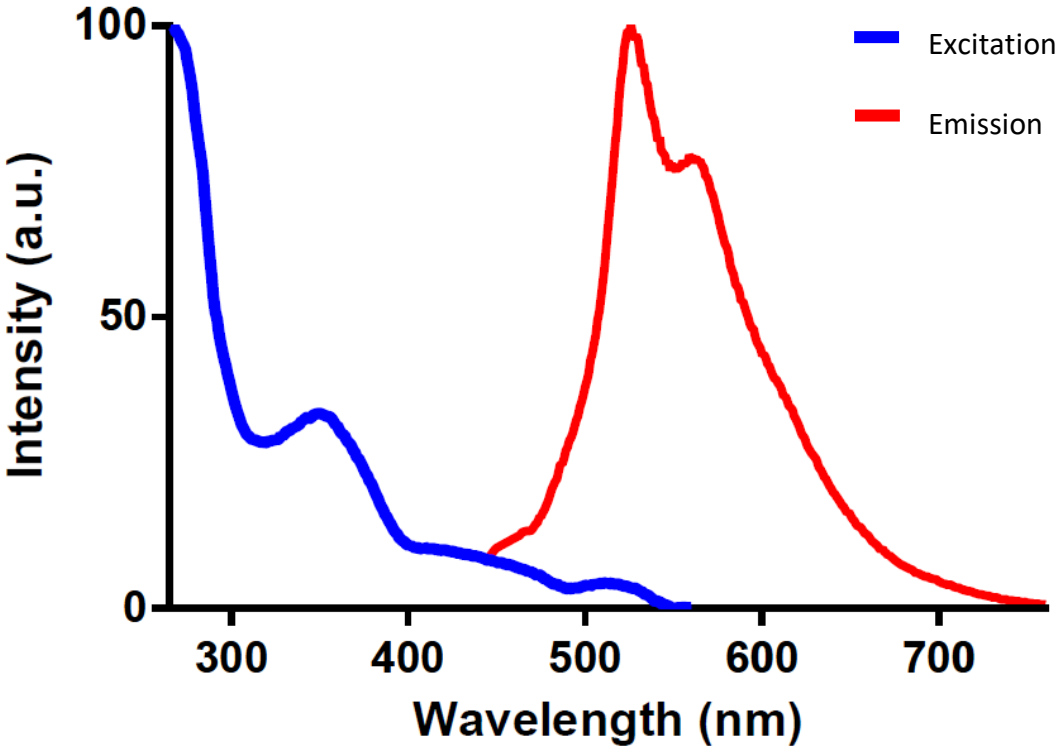

Figure 5-9. Electronic excitation (blue) and emission (red) spectra of $[Re(CO)_3(5\text{-PAN})Cl]$ for determination of achievable excitation with blue light was collected in a solution of 1:9 (v:v) MeOH/DCM. λ_{max} = 526 nm when excited at 450nm.

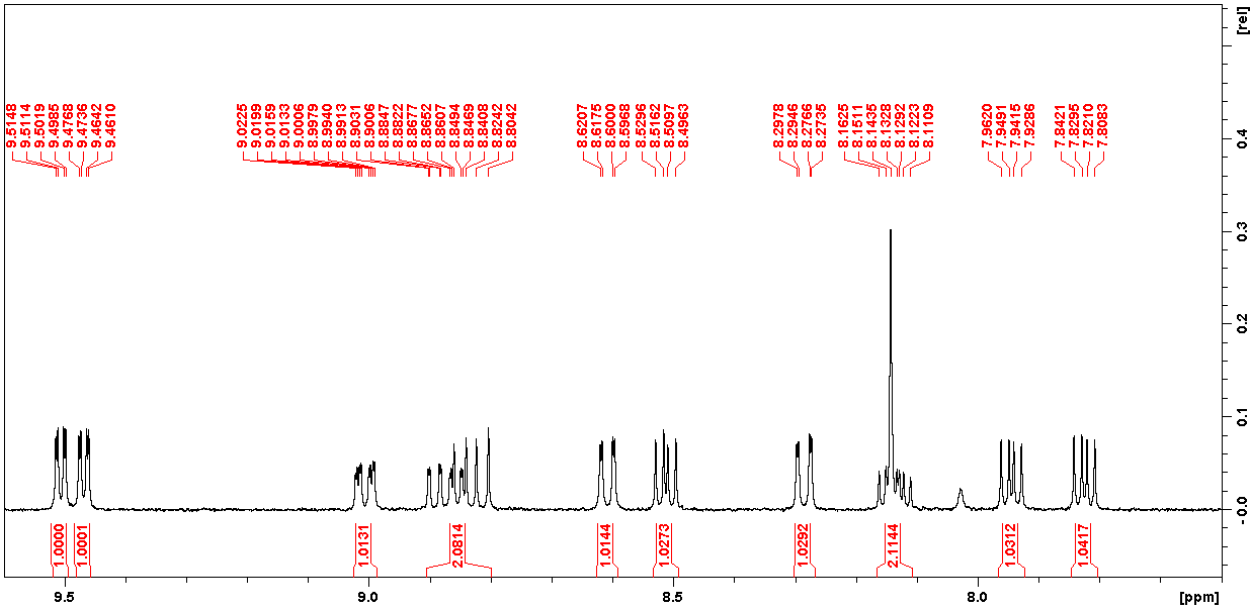

Figure 5-10. ^{1}H NMR spectrum of [$Re(CO)_3$(5-PAN)Cl] with zoomed in aromatic region (400 MHz, $CDCl_3$) δ 9.51-9.50 (dd, 1H), 9.48-9.46 (dd, 1H), 9.02-9.00 (ddd, 1H), 8.90-8.80 (2H, overlapped), 8.62-8.60 (dd, 1H), 8.53-8.50 (dd, 1H), 8.30-8.27 (dd, 1H), 8.16-8.11 (2H, overlapped), 8.00-7.92 (dd, 1H), 7.84-7.81 (dd, 1H).

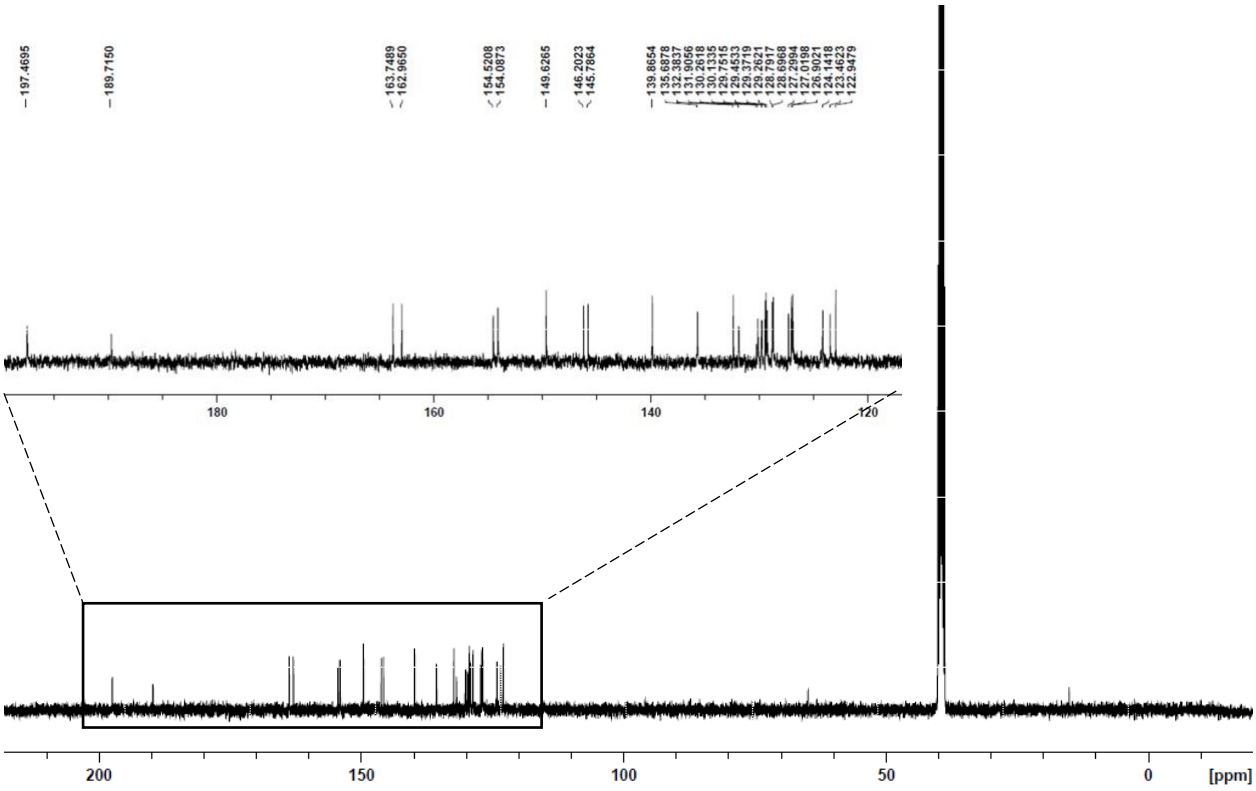

Figure 5-11. ^{13}C NMR spectrum of the $[Re(CO)_3(5\text{-PAN})Cl]$ complex, acquired in DMSO-d6, exhibiting the appropriate number of carbon signals – with the carbon signals at 189 ppm and 197 ppm, respectively, assigned as the carbonyl carbons of the rhenium tricarbonyl core.

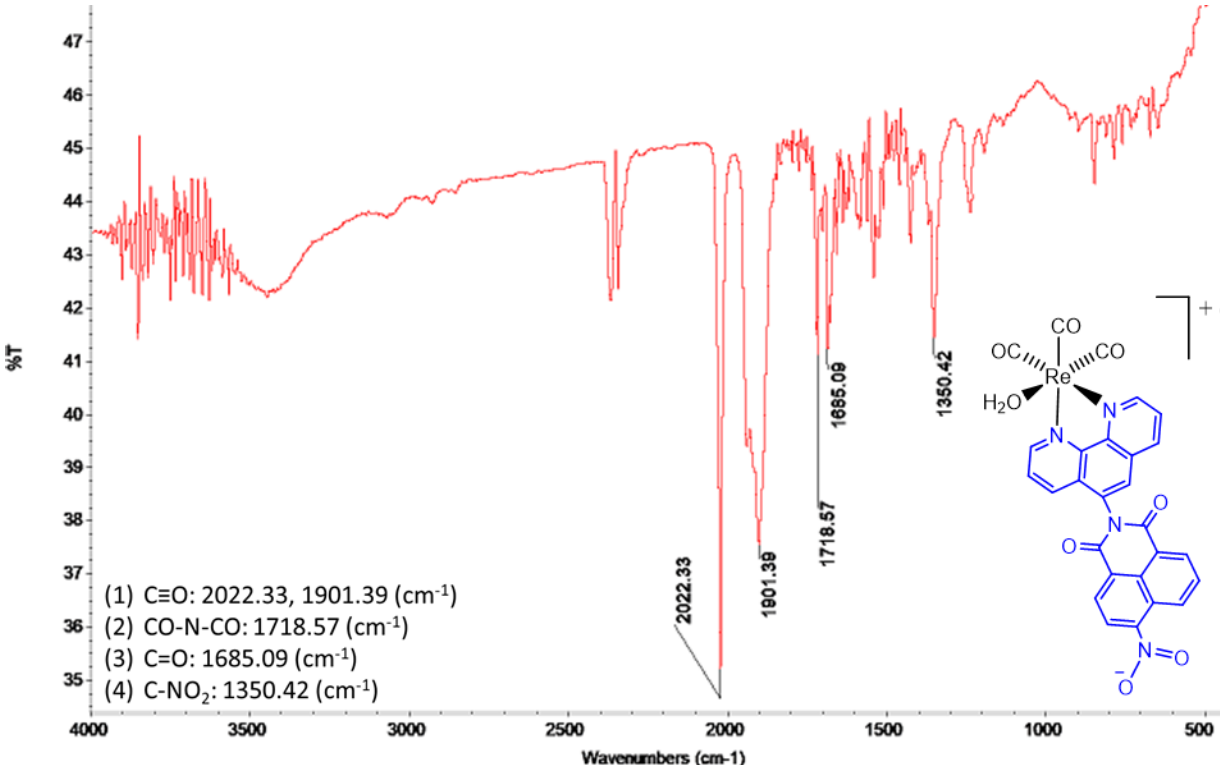

Figure 5-12. FT-IR of $[Re(CO)_3(5\text{-PAN})Cl]$ (KBr, cm^{-1}) C≡O: 2022; 1901, CO-N-CO: 1716, C=O: 1685.09, C-NO_2: 1350.

Table 5-1. Elemental Analysis of $[Re(CO)_3(5\text{-PAN})Cl]$ conducted by Intertek (Whitehouse, NJ, USA)

$[Re(CO)_3(5\text{-PAN})Cl]$	*%C*	*%H*	*%N*
Theoretical	44.08	1.66	7.62
Sample 1	44.08	1.79	7.07
Sample 2	42.58	2.16	7.12
Average	43.33	1.98	7.10
Error	-0.75	0.32	-0.52

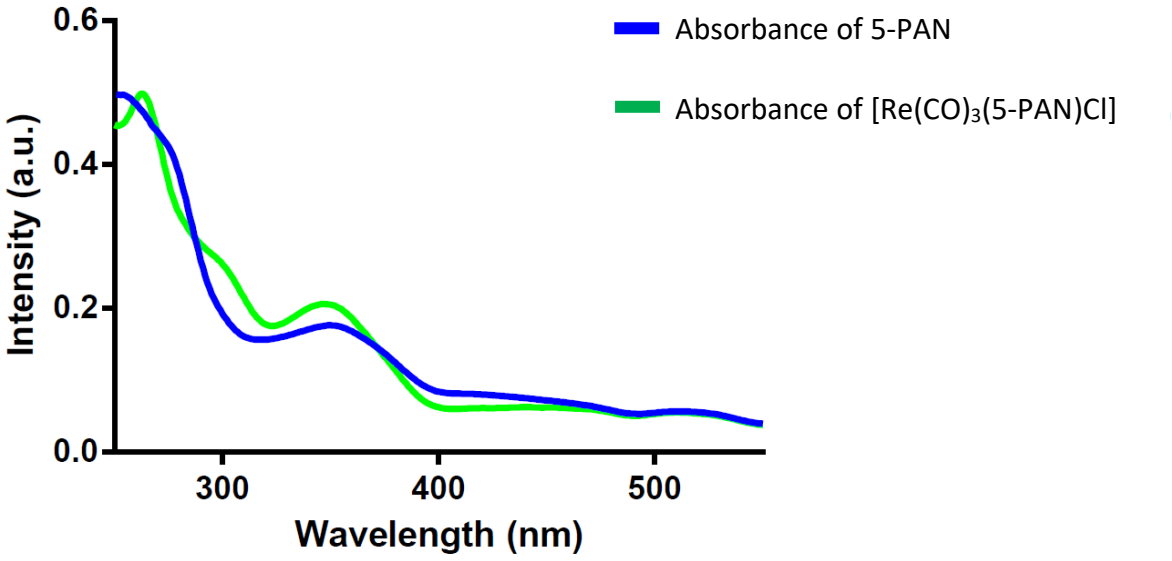

Figure 5-13. Electronic absorption spectra of both 5-PAN (blue) and $[Re(CO)_3(5\text{-PAN})Cl]$ (green) conducted in 1:9 (v:v) MeOH/DCM collected at equimolar concentration showing a broadening of the λ_{max} value of 5-PAN upon coordination to rhenium and a shift in absorbance toward blue wavelengths.

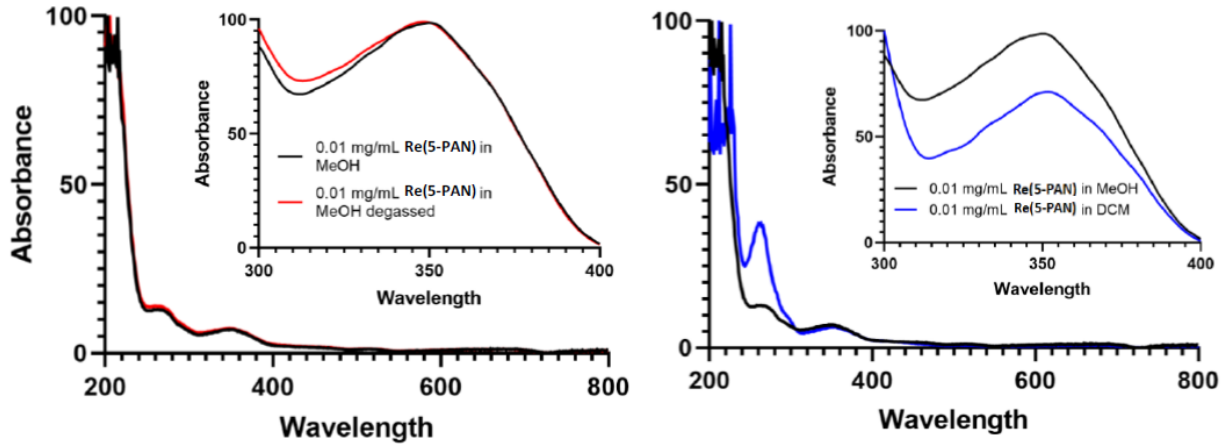

Figure 5-14. Electronic absorption spectrum of $[Re(CO)_3(5\text{-PAN})Cl]$ (Re(5-PAN)) conducted in both methanol and dichloromethane (right) showing a minimal red shift (2nm) of the absorption spectrum of Re(5-PAN) in a less polar solvent. Also depicted is the electronic absorption spectrum of Re(5-PAN) in both methanol and degassed methanol (left) – electronic absorption spectrum was collected utilizing samples of equimolar concentration of 0.0134 µM. Insets show a zoom of the region of interest containing the MLCT band from 300 – 400 nm.

5.1.5 Synthesis and characterization of $[Re(CO)_3(5\text{-PAN})Br]$

$[Re(CO)_3(5\text{-PAN})Br]$ was synthesized following the same method as that for $[Re(CO)_3(5\text{-PAN})Cl]$. $[Re(CO)_3(5\text{-PAN})Br]$ was characterized via ^1H NMR (**Figure 5-15**), ^{13}C NMR (**Figure 5-16**), FT-IR (**Figure 5-17**), and electronic absorbance spectroscopy (**Figure 5-18**).

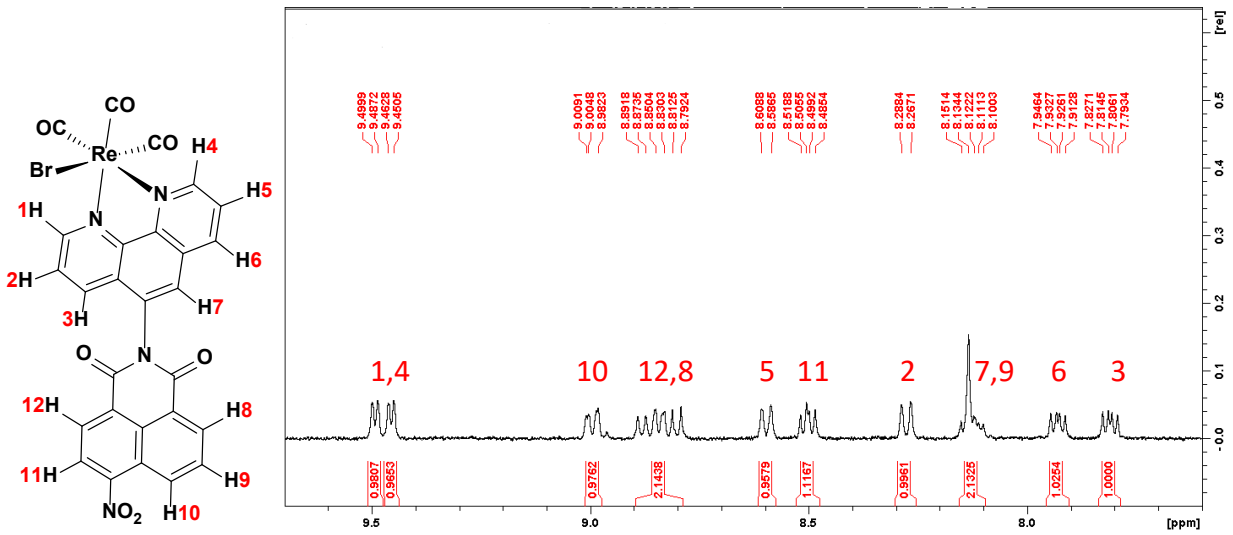

Figure 5-15. ^1H NMR of $[Re(CO)_3(5\text{-PAN})Br]$ in $CDCl_3$ with zoomed in aromatic region (400 MHz, chloroform-d) and image of **2** with assigned peaks. δ 9.49-9.48 (d, 1H, J=5.1 Hz), 9.46-9.45 (d, 1H, J=4.9 Hz), 9.00-8.98 (dd, 1H, J=9.1, 1.7 Hz), 8.89-8.79 (2H, overlapped), 8.60-8.58 (d, 1H, J=8.9 Hz), 8.50-8.48 (dd, 1H, J=7.9, 5.4 Hz), 8.28-8.26 (d, 1H, J=8.5 Hz), 8.15-8.10 (2H, overlapped), 7.94-7.91 (dd, 1H, J=8.0, 5.4 Hz), 7.82-7.79 (dd, 1H, J=8.4, 5.1 Hz). The appropriate integration of 12 was observed.

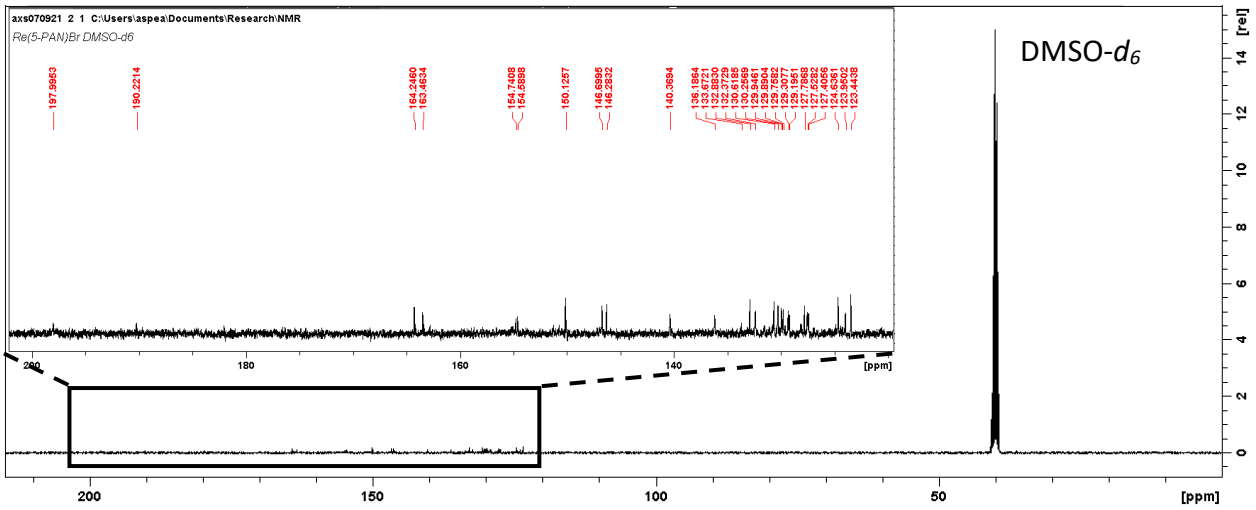

Figure 5-16. ^{13}C NMR spectrum of $[Re(CO)_3(5\text{-PAN})Br]$, acquired in DMSO-$d_6$ exhibiting the appropriate number of peaks. The carbon signals at 197 ppm and 180 ppm are assigned to the carbonyl carbons on the rhenium tricarbonyl core.

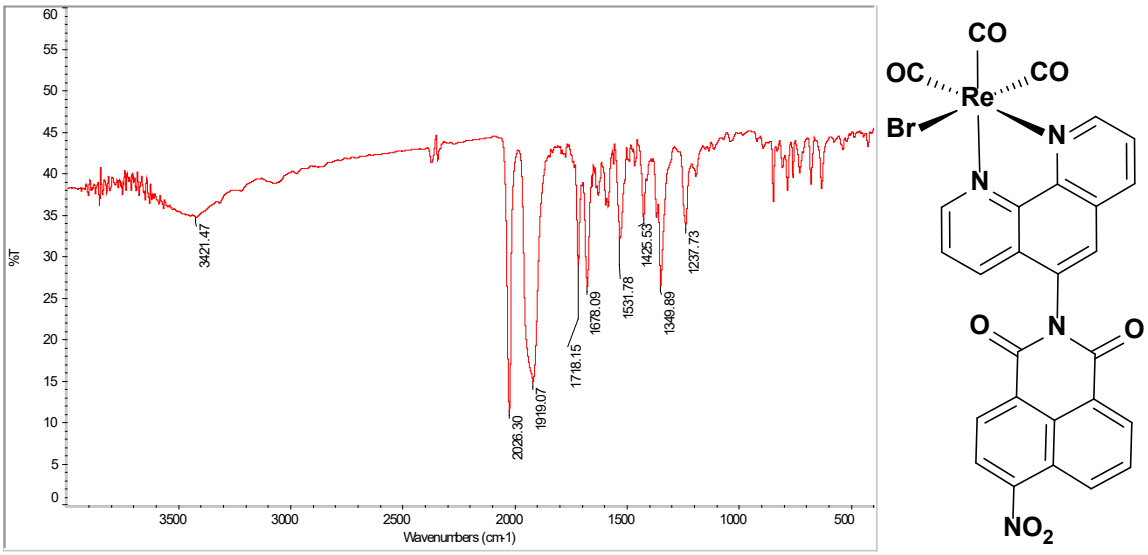

Figure 5-17. FT-IR of $[Re(CO)_3(5\text{-PAN})Br]$ (KBr, cm^{-1}) C≡O: 2026.30; 1919.07, CO-N-CO: 1718.15, C=O: 1678.09, C-NO_2: 1349.89.

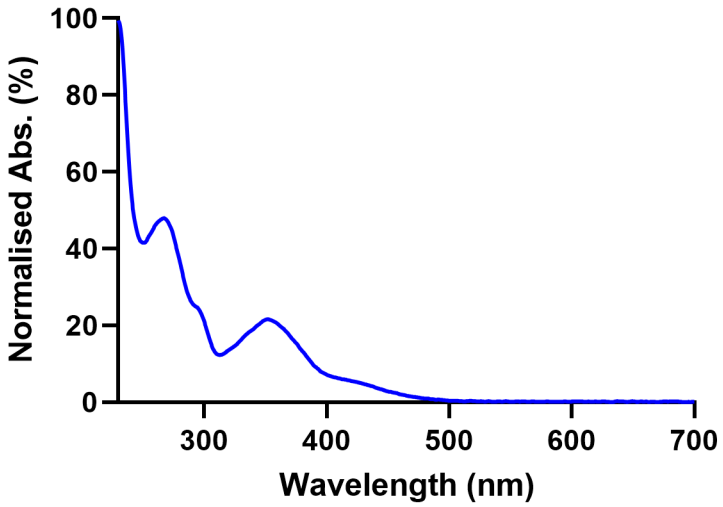

Figure 5-18. Electronic absorption spectrum of $[Re(CO)_3(5\text{-PAN})Br]$ in MeOH/DCM (1:9 v:v).

5.1.6 Synthesis of BIH

The synthesis of BIH was modified from literature procedures. 2-phenylbenzimidazole (3 g) was mixed with methyl iodide (8 g) in 15 mL of anhydrous MeOH containing NaOH (0.64 g) in a pressure tube. The tube was purged with argon then sealed and heated at 110 °C with stirring for 3 days. After cooling to room temperature, crystals formed. The crude intermediate was filtered and washed with MeOH and dried in vacuo. The intermediate was dissolved in 80 mL of anhydrous MeOH and $NaBH_4$ (1.5 g) was slowly added and stirred for 1 hour under argon. The solvent was then evaporated, and the product was recrystallized in hot ethanol/water 5:1 to give white crystals of BIH in 75% yield. BIH was verified via ^{1}H NMR (**Figure 5-19**) and ^{13}C NMR (**Figure 5-20**).

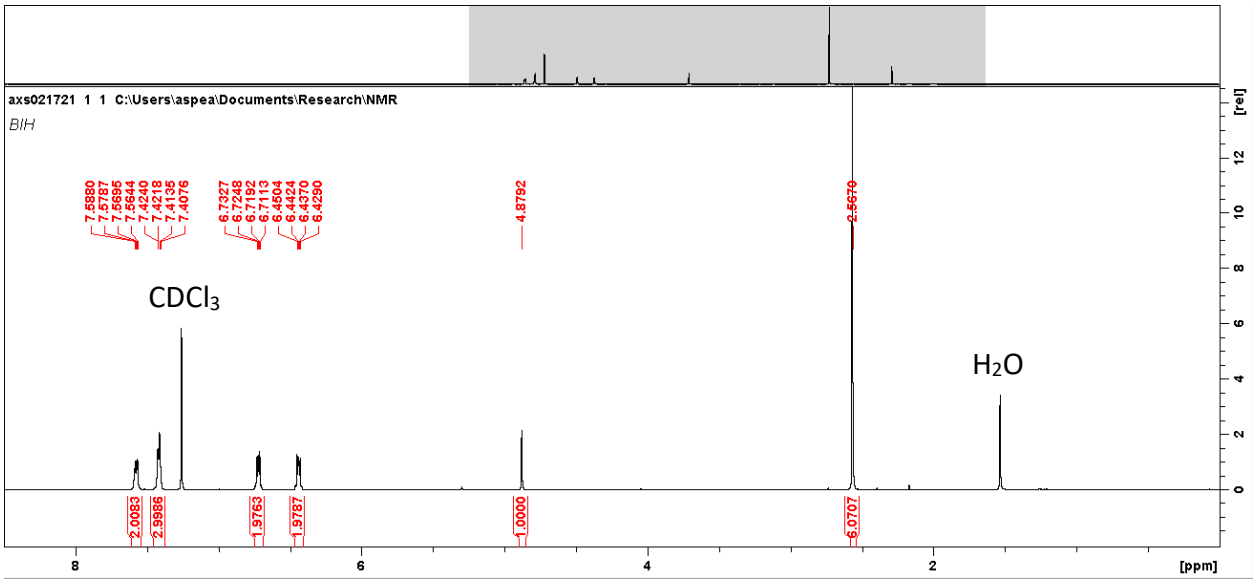

Figure 5-19. ^{1}H NMR of BIH (400 MHz, chloroform-d): δ 2.5670 (s, 6H), 4.88 (s, 1H), 6.43-6.45 (dd, J = 3.2, 5.4 Hz, 2H), 6.71-6.73 (dd, J = 3.2, 5.4 Hz, 2H), 7.41-7.42 (m, 3H), 7.56-7.59 (m, 2H).

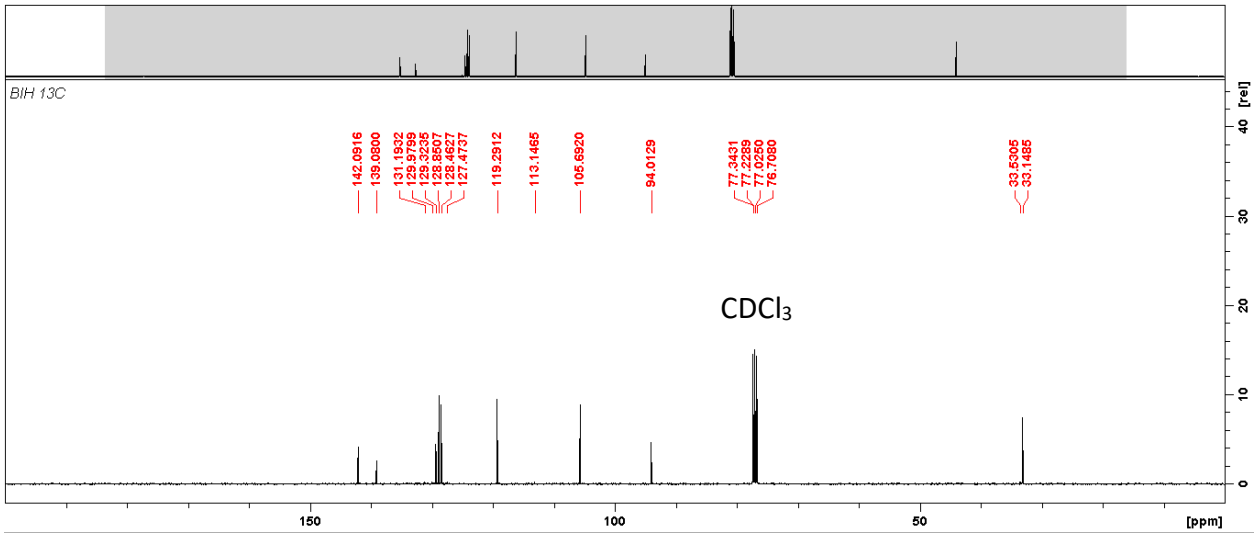

Figure 5-20. ^{13}C NMR of BIH (400 MHz, chloroform-d, D1=5). The peaks at 33.1485 and 33.5305 correspond to the methyl groups of BIH and the integration was set to 1 in subsequent NMR spectra in which the peaks were used as the internal reference.

5.1.7 Cyclic voltammetry

Cyclic voltammetry was performed on an Electrochemical Analyzer potentiostat model 600D from CH Instruments. CV solutions were prepared in acetonitrile and degassed by bubbling with nitrogen for about 10 min prior to scanning. Tetra(n-butyl)ammonium hexa-fluorophosphate ($TBAPF_6$; ca. 0.1 M in acetonitrile) was used as the supporting electrolyte. A Pt wire was used as the pseudo reference electrode; a Pt wire coil was used as the counter electrode and an Au disk electrode was used for the working electrode. The redox potentials are reported using the ferrocenium/ferrocene (Fc^+/Fc) redox couple as an internal reference.

5.1.8 Crystallography

Crystals of $[Re(CO)_3(5\text{-}PAN)X]$ (X = Cl or Br) suitable for single crystal X-ray diffraction studies were only obtained by combining $[Re(CO)_3(5\text{-}PAN)Cl]$ and $[Re(CO)_3(5\text{-}PAN)Br]$ (1 : 4 by mass) in MeOH/DCM (1 : 9 v/v) and gently layering toluene on top, then sealing the glass vial with a cap and parafilm. The crystallographic work was done by William W. Brennessel at the X-ray Crystallographic Facility of the Department of Chemistry at the University of Rochester, New York, United States and is detailed in Appendix A.

5.1.9 DFT Vibrational Frequencies

In silico determination of the predicted rhenium-chloride vibrational frequencies of $Re(CO)_5Cl$ and a $[Re(CO)_3(5\text{-}PAN)Cl]$ analog $Re(C_{12}H_8N_2)(CO)_3Cl$ ($Re(CO)_3(Phen)Cl$)(**Figure 5-21**). Density functional theory simulations of the monomeric molecular structures and vibrational frequencies of $Re(CO)_5Cl$ and $Re(CO)_3(Phen)Cl$ were performed with the Gaussian 16 (Revision A.03) software package. The calculations utilized the B3LYP density functional and def2-TZVP basis set for all atoms. Point group symmetry was utilized in both species, with $Re(CO)_5Cl$ in C4v

and $Re(CO)_3(phen)Cl$ in Cs. Convergence quality was increased from the default configuration using program settings of integral (grid=superfine) and opt=verytight. Harmonic vibrational frequency analyses of the optimized structures revealed no imaginary eigenvalues, verifying each structure to represent an energetic minimum on the potential energy surface. For $Re(CO)_5Cl$: Re-Cl (Exp.) = 2.515 Å, Re-Cl (DFT) = 2.500 Å. DFT Re-Cl stretching frequency = 296.65 cm^{-1} . For $Re(CO)_3(phen)Cl$: Re-Cl (Exp.) = 2.500 Å, Re-Cl (DFT) = 2.495 Å. DFT Re-Cl stretching frequency = 281.08 cm^{-1} [115,116].

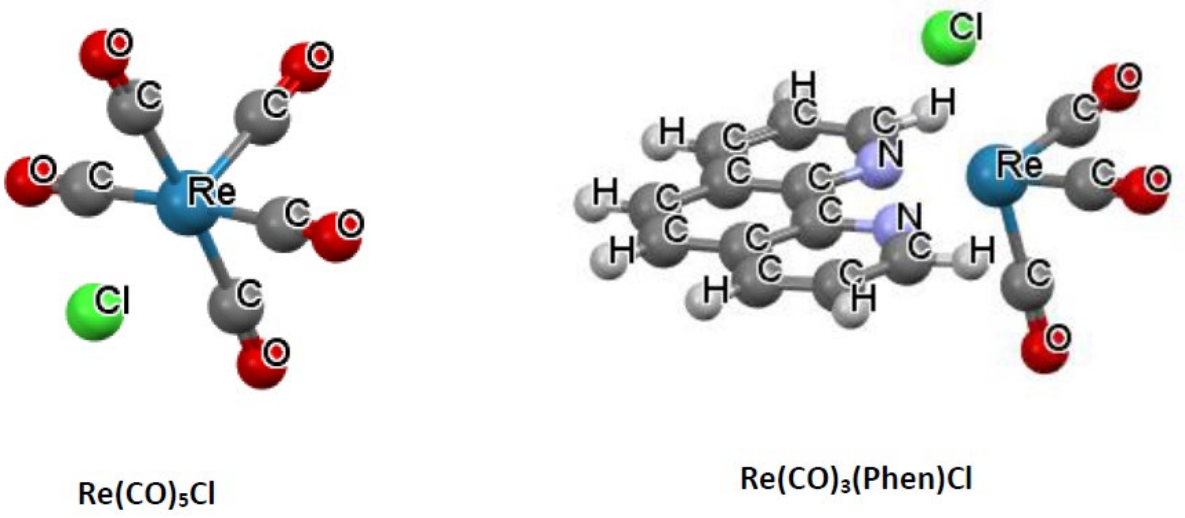

Figure 5-21. *In silico* determination of the predicted rhenium-chloride vibrational frequencies of $Re(CO)_5Cl$ and a Re(5-PAN) analog ($Re(CO)_3(Phen)Cl$) reindicating shift to a lower vibrational frequency.

5.1.10 DFT-TDA

The electronic structure of the metal complex was simulated with Gaussian 16 Rev C.01 using the B3LYP density functional and the def2-TZVP basis set (all-electron basis functions for the atoms except Re, which utilized an effective-core potential). The starting geometry of the

complex was taken from the experimental crystallographic structure and the structure was then fully geometry optimized. Solvent effects were included in all calculations using the Polarizable Continuum Model (nonequilibrium for the3 excited states) with DCM as the specified solvent. Vertical electronic transitions were calculated with time-dependent DFT based on the Tamm-Dancoff approximation (TDA) and included 100 states (singlets and triplets) to explore the possible transitions.

Table 5-2. Orbital density plots of $[Re(CO)_3(5\text{-PAN})Cl]$

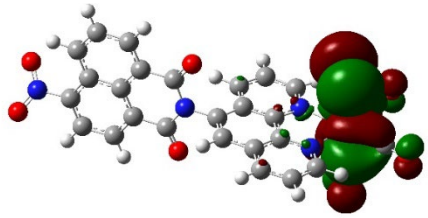 HOMO	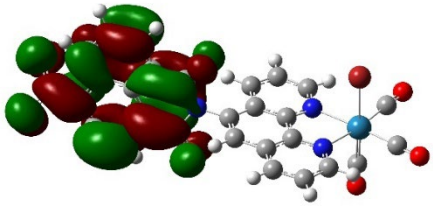 LUMO
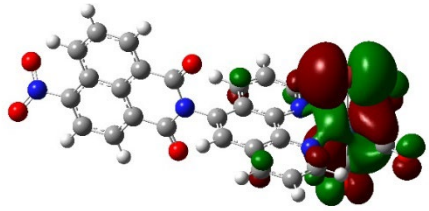 HOMO-1	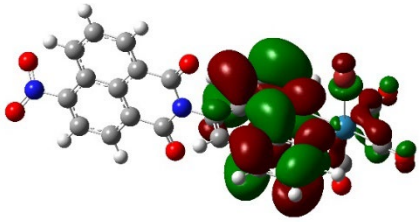 LUMO+1

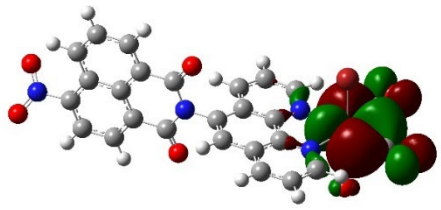	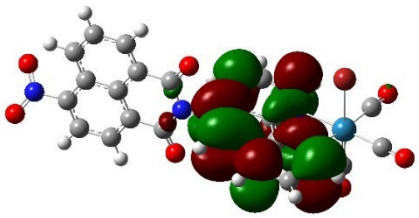
HOMO-2	LUMO+2

5.1.11 CO_2RR procedure

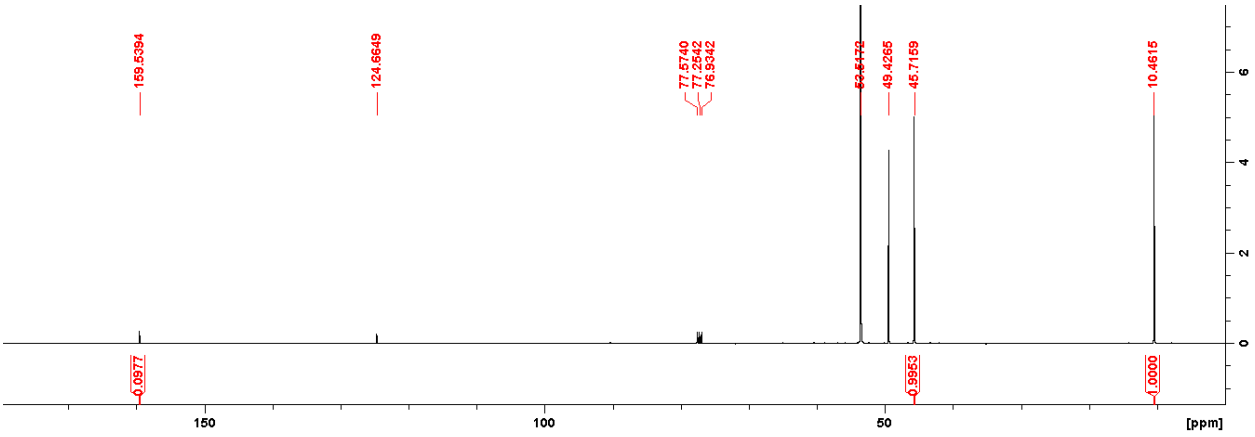

Figure 5-22. ^{13}C NMR for $[Re(CO)_3(5\text{-PAN})Cl]$ and 150 equivalences TEA. The TEA peaks are at 10.4615 and 45.7159 ppm. Methanol peak is at 49.4265 ppm. DCM peak is at 53.5172 ppm. $CDCl_3$ peaks are at 76.9342, 77.2542, and 77.5740 ppm. $^{13}CO_2$ peak is at 124.6649 ppm. $H^{13}COO^-$ 159.5394 ppm.

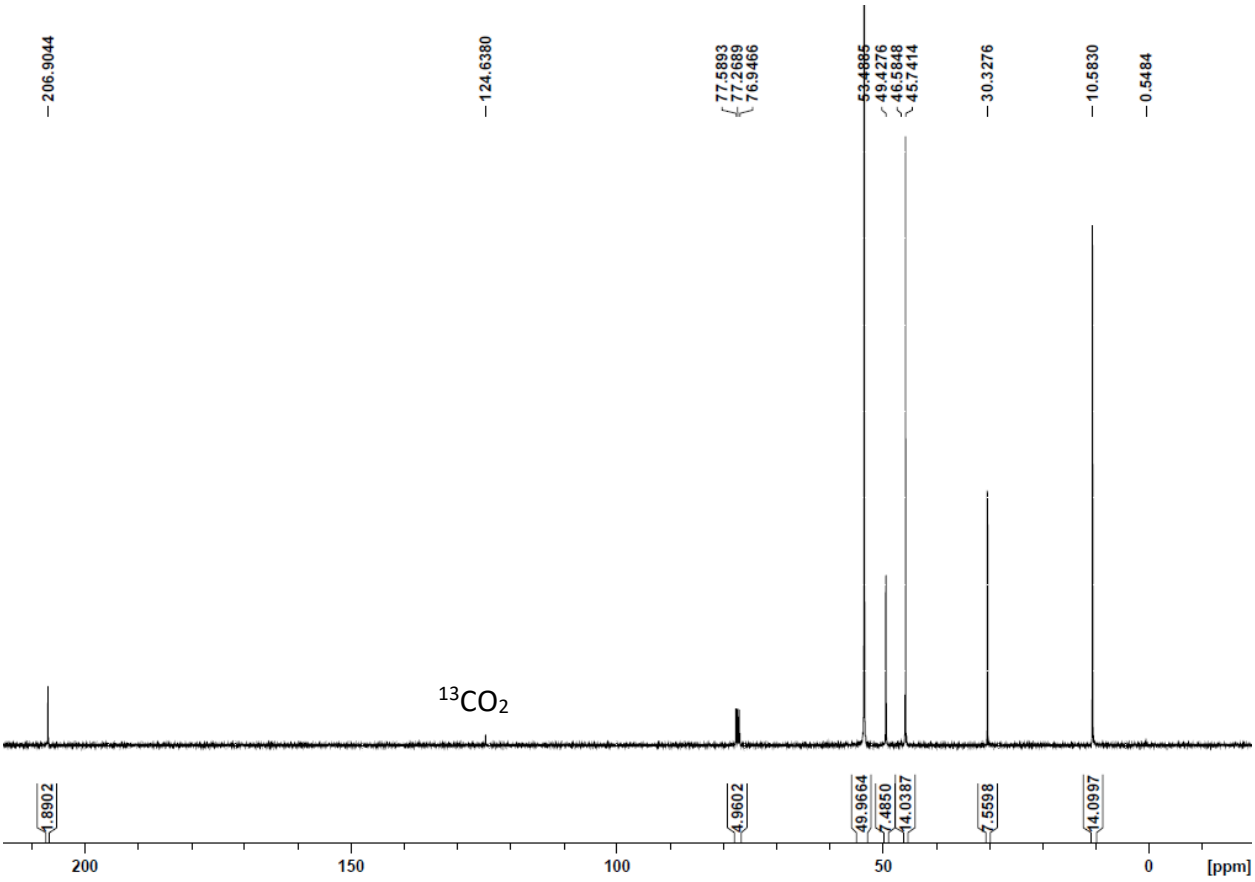

Figure 5-23. ^{13}C NMR of a CO_2/5-PAN solution in 1:9 (v:v) MeOH/DCM indicating only the presence of $^{13}CO_2$ when photoirradiated at 450 – 460 nm – suggesting no catalysis without the $[Re(CO)_3(5\text{-PAN})Cl]$complex. All other peaks are attributed to solvents, including a minor acetone impurity as noted by the peaks at 30 and 207 ppm, respectively, or sacrificial donor TEA.

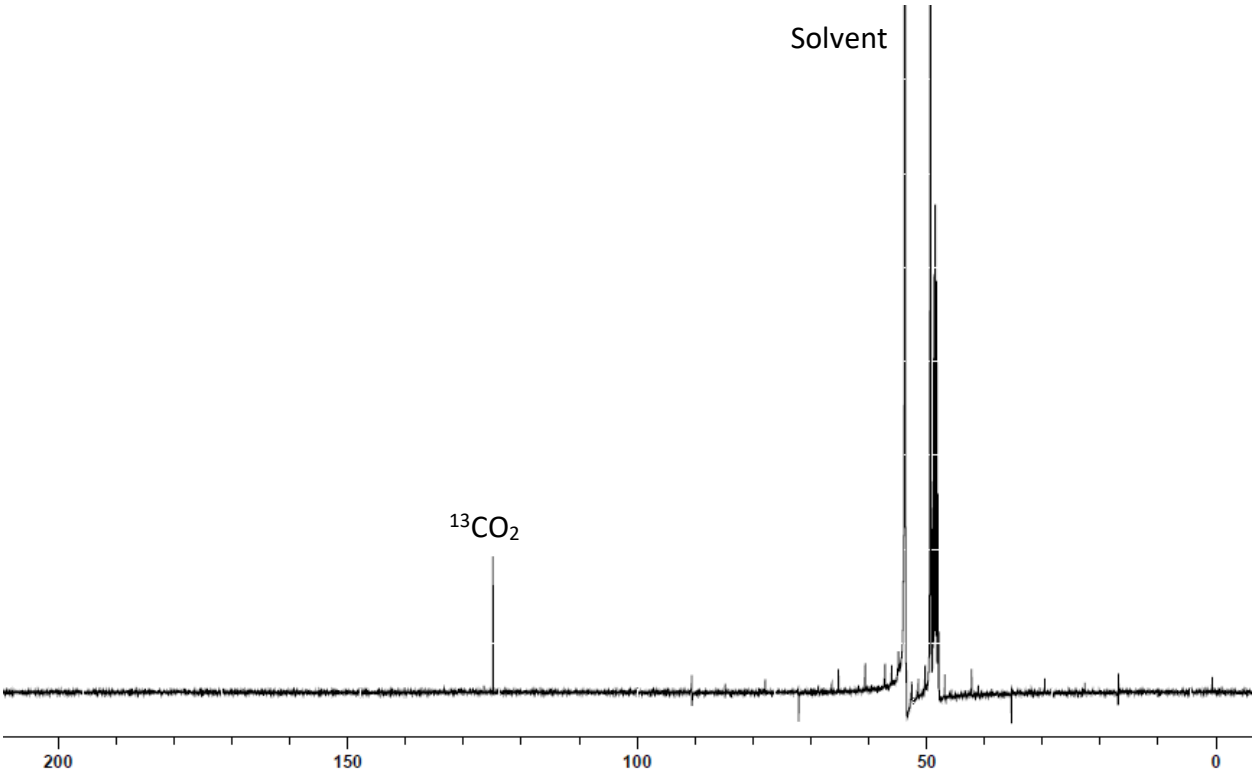

Figure 5-24. ^{13}C NMR of a CO_2/[$Re(CO)_3$(5-PAN)Cl] solution in 1:9 (v:v) MeOH:DCM indicating only the presence of $^{13}CO_2$ when not photoirradiated at 450 – 460 nm.

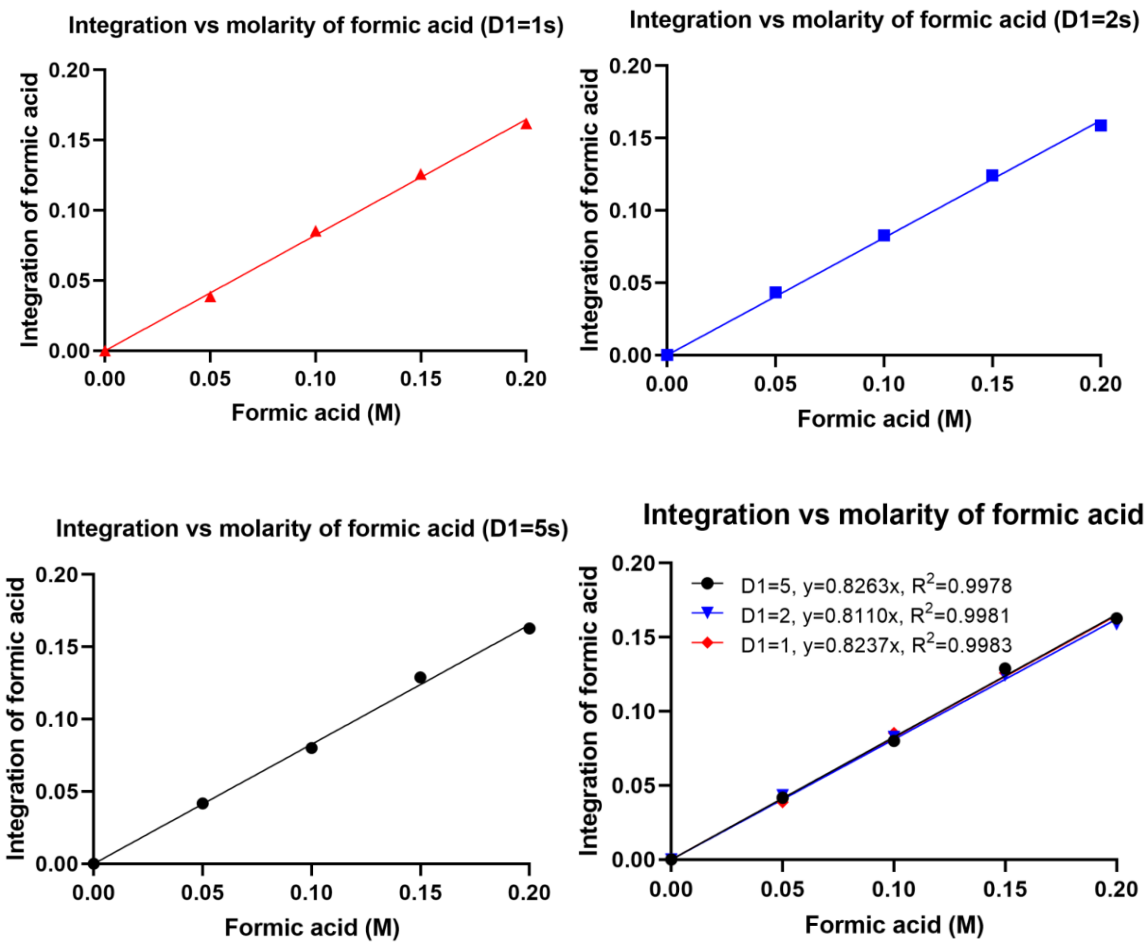

Figure 5-25. Linear regression of the ^{13}C NMR integration of $H^{13}COO^-$ supplemented with an internal standard of 100 equivalents TEA at D1 relaxation times of D1 = 1s (top left), 2s (top right), and 5s (bottom left). Also displayed is an overlay of all the independent linear regression at the previously described relaxations (bottom right).

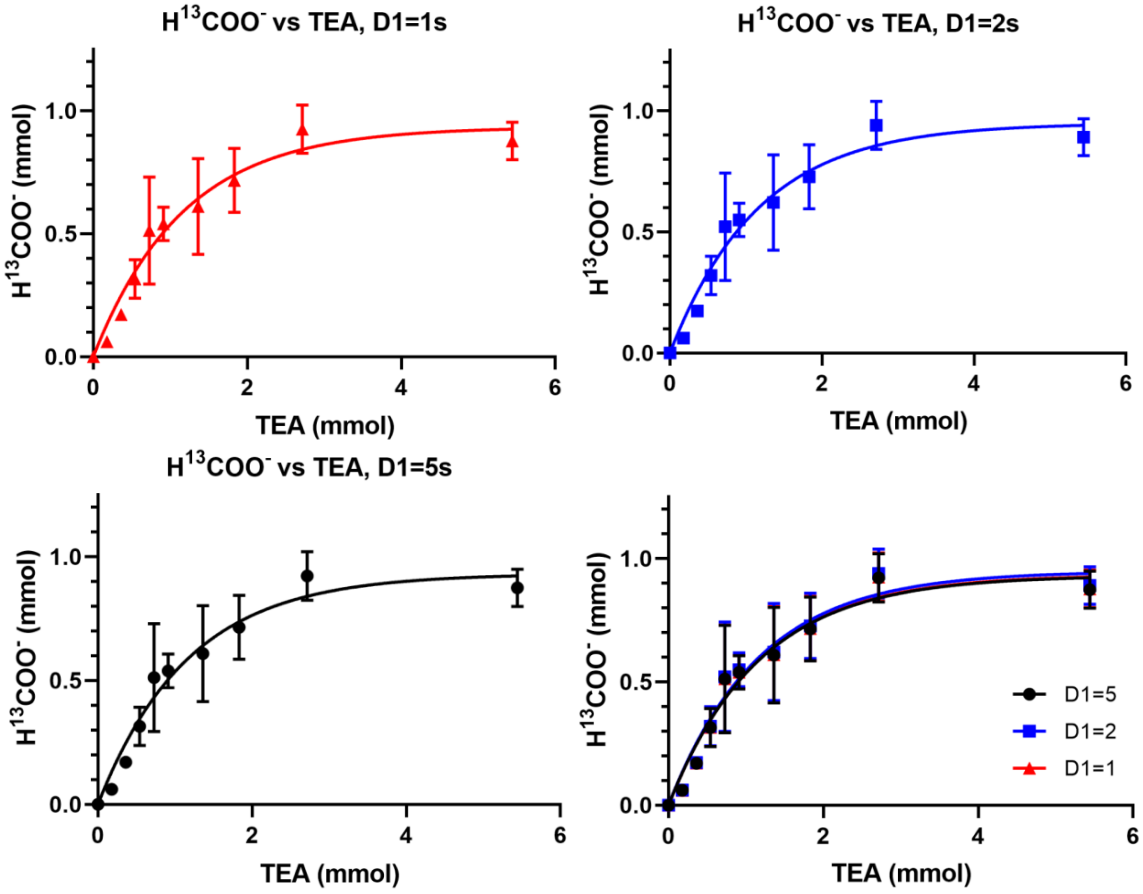

Figure 5-26. Turnover numbers for [Re(CO)$_3$(5-PAN)Cl] calculated from the linear regression of D1 = 1s (top left), 2s (top right), and 5s (bottom left). Also displayed is an overlay of all of the independent TN plots at the previously described relaxations (bottom right) showing similar R^2 values consistent about 0.96.

Table 5-3. Tabulated TN numbers for $[Re(CO)_3(5\text{-PAN})Cl]$

TEA equivalents	*TN (D1=5)*	*TN (D1=2)*	*TN (D1=1)*
0	0	0	0
10	3.33	3.39	3.34
20	9.41	9.59	9.44
30	17.32	17.65	17.38
40	28.21	28.75	28.30
50	29.77	30.33	29.86
75	33.48	34.11	33.59
100	39.10	39.84	39.23
150	50.96	51.92	51.12
300	48.34	49.25	48.49

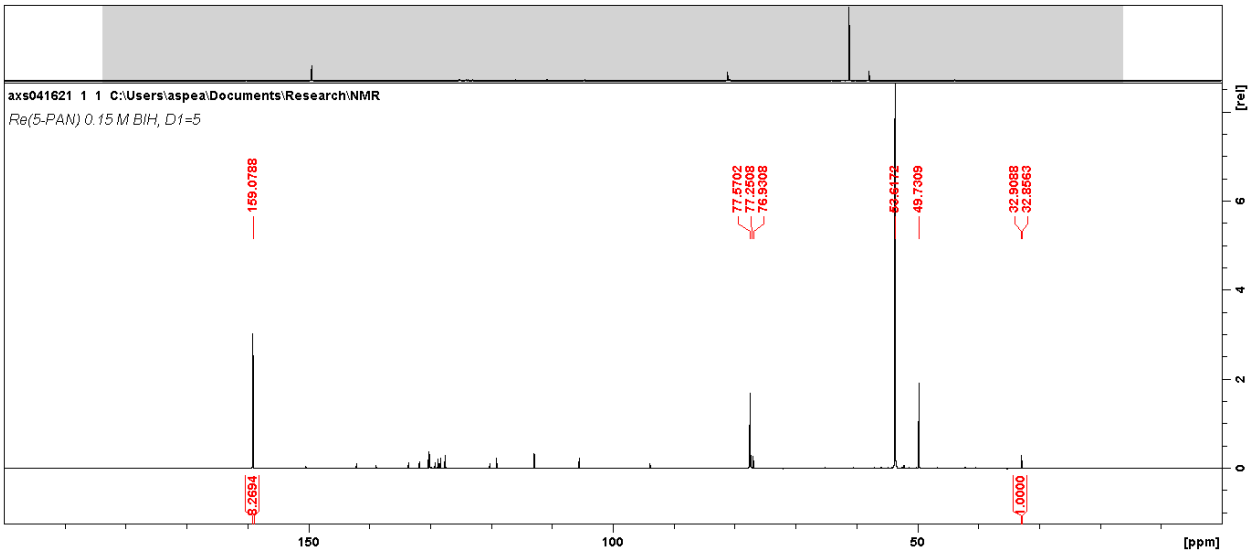

Figure 5-27. ^{13}C NMR for $[Re(CO)_3(5\text{-PAN})Cl]$ and 0.15 M (0.75 mmol) BIH. The BIH methyl peaks are 32.86 and 32.91 ppm. Methanol peak is at 49.73 ppm. DCM peak is at 53.61 ppm. $CDCl_3$ peaks are at 76.93, 77.25, and 77.57 ppm. $H^{13}COO^-$ peak is at 159.08 ppm. The remaining peaks between 90-150 ppm are attributed to BIH.

a)

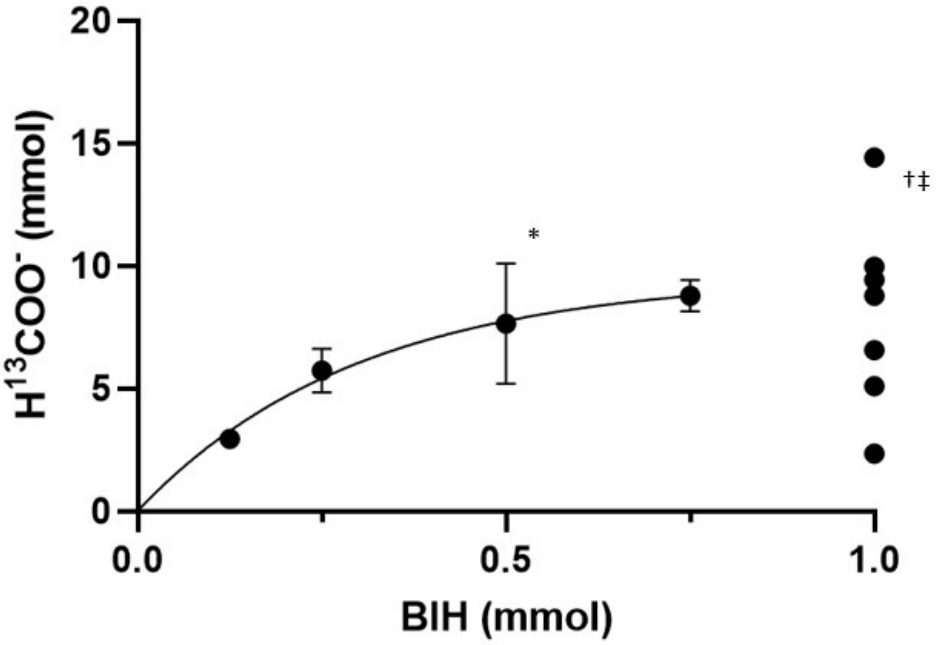

b)

Figure 5-28. (a) CO_2RR procedure without Pre-mixing BIH. At higher concentrations of BIH (1 mmol and above) the solubility limit of BIH in CH_3OH/DCM (1:9 v:v) is met, which varies the amount of BIH available to react and the amount of $H^{13}COO^-$ produced. Pre-mixing BIH in the solvent for 10 min before adding [$Re(CO)_3$(5-PAN)Cl] and $^{13}CO_2$ mitigates the variability. (b) Images of the reaction mixture at 0.5 mmol BIH* and 1.0 mmol BIH without pre-mixing† show clear and cloudy solutions, respectively. Pre-mixing the BIH (1.0 mmol), then adding [$Re(CO)_3$(5-PAN)Cl] results in a transparent solution‡.

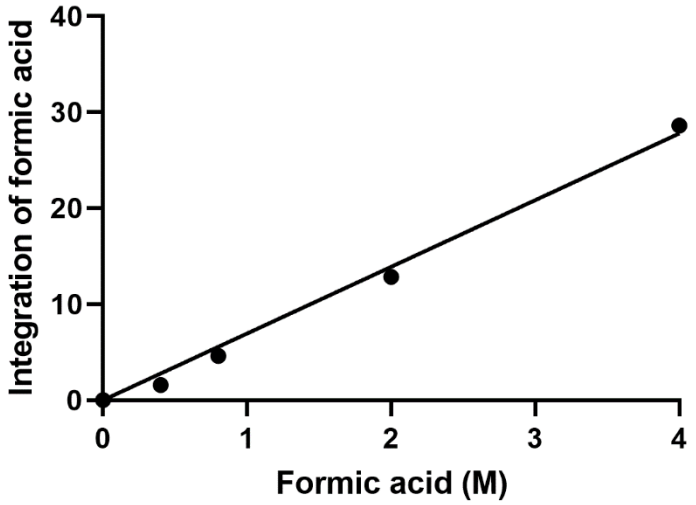

Figure 5-29. Calibration curve of the ^{13}C NMR integration of $H^{13}COO^-$ supplemented with an internal standard of 0.1 M BIH at a D1 relaxation time of 5 s. The linear regression is y=6.946x. The R^2 = 0.9927.

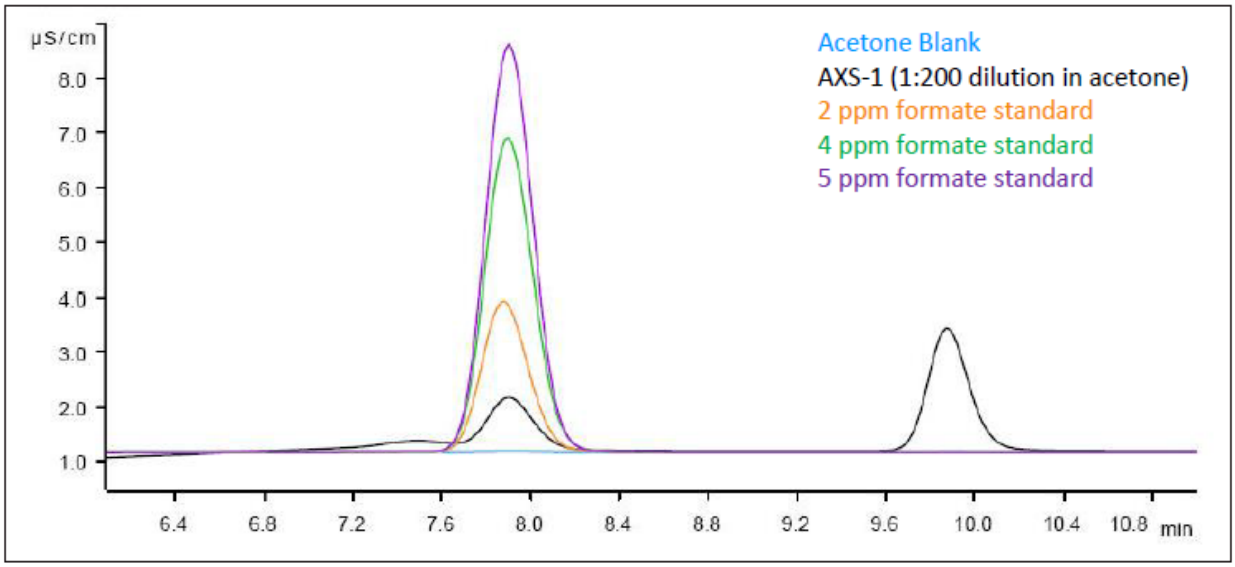

Overlay of Sample and Formate Standard Chromatograms

A

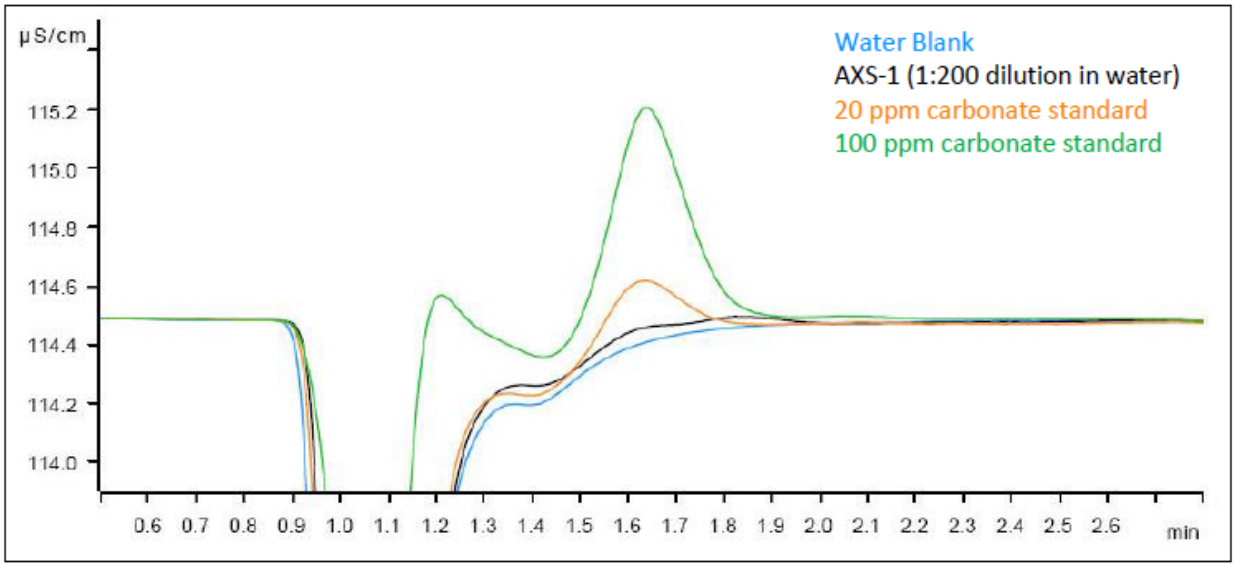

Overlay of Sample and Carbonate Standard Chromatograms

B

Figure 5-30. Ion chromatography of a reaction solution containing [$Re(CO)_3$(5-PAN)Cl] and BIH after irradiation. Formate was detected while carbonate was not. The peak eluting just before 10 min in **A** is likely chloride.

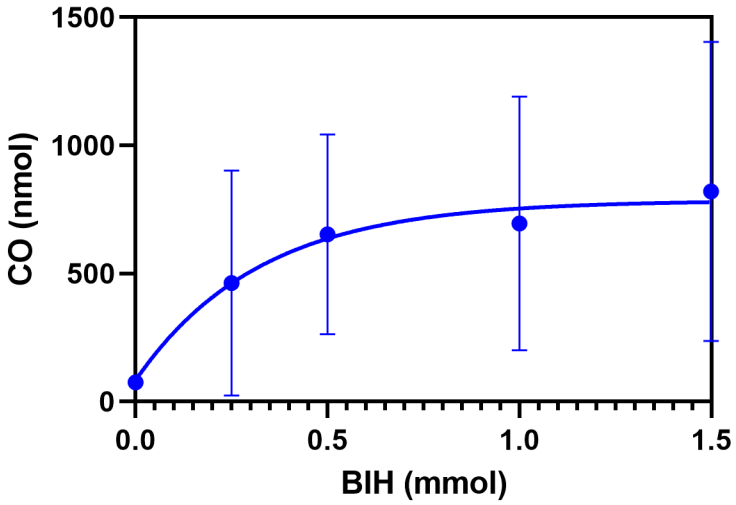

Figure 5-31. A plot of CO (nmol) vs BIH (mmol) upon blue light irradiation of $[Re(CO)_3(5\text{-PAN})Cl]$ for 30 min. CO amounts were determined by GC analysis of the headspace of a vial containing the reaction mixture.

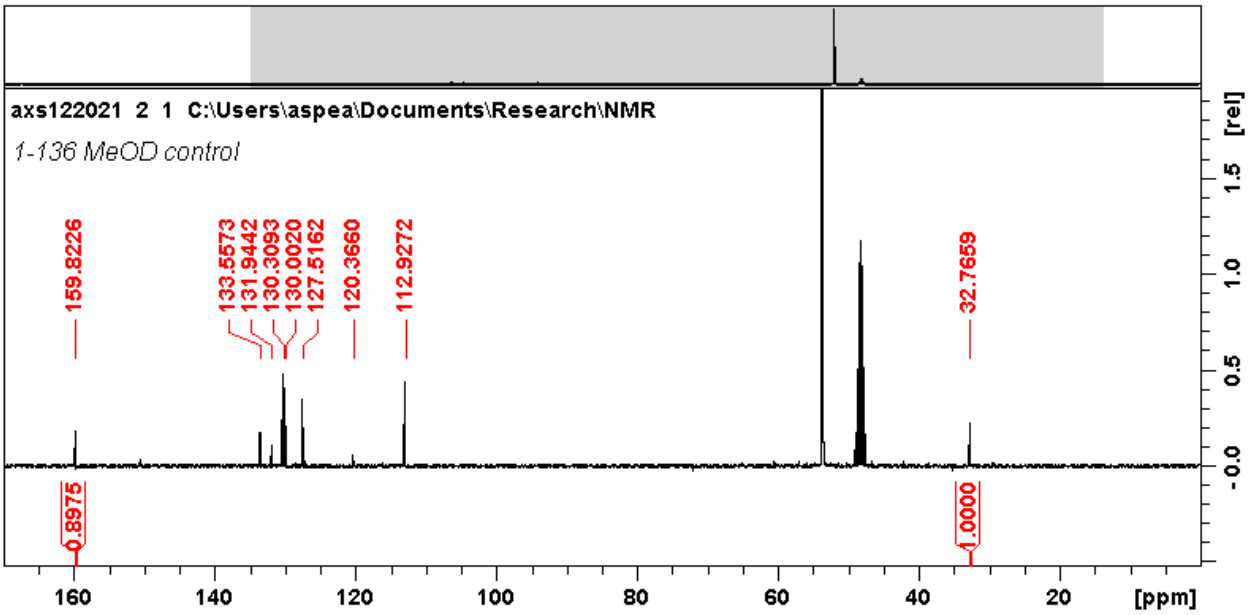

Figure 5-32. ^{13}C NMR of $[Re(CO)_3(5\text{-PAN})Cl]$ and 0.1 M BIH in CD_3OD/DCM (1:9 v:v) after irradiation with blue light for 1.5 hours. The integration of the formate peak at ~160 ppm is greatly diminished from 10.6 (average value for experiments using 0.1 M BIH) to 0.9. The peaks between 112-133 ppm and ~32 ppm are attributed to BIH. The remaining peaks are solvent related.

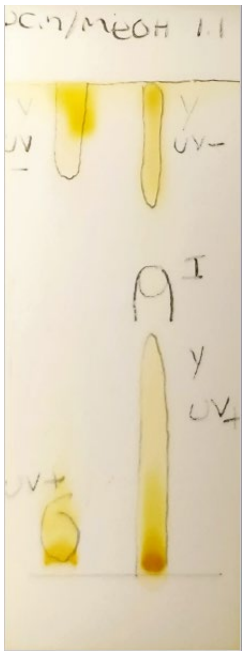

Figure 5-33. TLC of reaction solution before and after irradiation. DCM/MeOH (1:1, v:v) was used as the mobile phase. The Rf values are listed; $[Re(CO)_3(5\text{-PAN})Cl]$ = 0.90, BIH = 0.04, BI^+ = 0.59. Spots were determined by UV and iodine vapor.

5.2 Chapter 3 Experimental

5.2.1 General methods and instrumentation

All solvents and chemicals were purchased from Sigma-Aldrich (Milwaukee, WI, USA) unless noted otherwise and were used as received. *Cis*-diammineplatinum(II) dichloride was purchased from Tokyo Chemical Industries America (Philadelphia, PA, USA). 6,8-difluoro-7-hydroxy-4-methylcoumarin NHS ester was purchased from Fluoroprobes (Scottsdale, AZ, USA). HEK-293 cells and Dulbecco's Modified Eagle Medium (DMEM) were obtained from American Type Culture Collection (Manassas, VA, USA). Cell Counting Kit-8 (CCK-8) was purchased from Dojindo Laboratories (Kamimashiki-gun, Kumamoto, Japan).

Deionized water was produced in-house and filtered through a 0.2 μm pore vacuum filter prior to use. Hank's Buffered Salt Solution (HBSS) was prepared as follows: NaCl (8 g), KCl (0.4 g), $CaCl_2$ (0.14 g), $MgSO_4 \bullet 7H_2O$ (0.1 g), $MgCl_2 \bullet 6H_2O$ (0.1 g), $Na_2HPO_4 \bullet 2H_2O$ (0.06 g), KH_2PO_4 (0.06 g), and $NaHCO_3$ (0.35 g), were dissolved in 1 L of H_2O, filtered through a 0.2 μm pore vacuum filter, and sonicated for 1 hour in an ultrasonic bath and stored at 4 °C.

High resolution mass spectrometry (HRMS) was conducted on a Fusion Lumos Orbitrap mass spectrometer. ^{1}H, ^{13}C, and ^{195}Pt NMR were conducted on a Bruker Avance III HD 400 MHz instrument and were obtained after dissolving complexes in ACN-d3 or D_2O. The chemical shifts were expressed as δ (in ppm) from internal reference standard tetramethylsilane (TMS, ^{1}H NMR) or external reference 1 M Na_2PtCl_6 (^{195}Pt NMR), as appropriate. FT-IR was carried out on a Nicolet infrared spectrophotometer utilizing potassium bromide (KBr) disks. Electronic absorbance spectra were measured on a Thermo Scientific NanoDrop One^{C} microvolume spectrophotometer. Excitation and emission spectra were measured on an Agilent Technologies Cary Eclipse fluorescence spectrophotometer. Reaction tracking and purity was monitored by reverse-phase high performance liquid chromatography (RP-HPLC) on an Agilent Technologies series 1100 instrument with solution A: 0.01% TFA in H_2O, and solution B: 0.01% TFA in ACN. The method parameters were 5-60% B for 15 min, 95% B for 5 min, and 5% B for 5 min. Centrifugation was performed in a Sorvall Legend RT or VWR Micro Star 21 centrifuge. Live-cell imaging was conducted in 35 mm petri dishes with 14 mm microwells and #1.5 coverslips from MatTek (Ashland, MA, USA). Cytotoxicity assays were monitored using a Molecular Devices FlexStation 3. Confocal images were recorded using a Zeiss confocal laser

scanning microscope with Airyscan (980) using a 63x oil objective and processed using FIJI software (version 1.53t).

5.2.2 Synthesis of oxoplatin and fluoroplatin

cis,cis,trans-[$Pt(NH_3)_2Cl_2(OH)_2$] (oxoplatin): oxoplatin was synthesized by literature methods[33]. Briefly, 30% hydrogen peroxide (60 mL) was added drop wise to cisplatin (0.480 g, 1.59 mmol) in a round bottom flask. The reaction mixture was heated to 75 °C for 5 hours. The yellow solution was kept at room temperature in the dark overnight and crystals of the product formed. Yellow crystals were separated by filtration, washed with cold water and dried to obtain 0.495 g of oxoplatin (93% yield). **HRMS** (*m/z*, pos) $[M+H]^+$: expected, 333.05; observed, 333.9676. **FT-IR** (KBr, cm^{-1}): 3515.44 (w), 3459.63 (br, OH), 3252.77 (w), 1584.35 (s), 1441.53 (s), 1379.14 (s), 1073.19 (m, Pt-OH), 859.20 (w). All characterizations are detailed in the supplemental information (**Figure 5-34** and **Figure 5-35**).

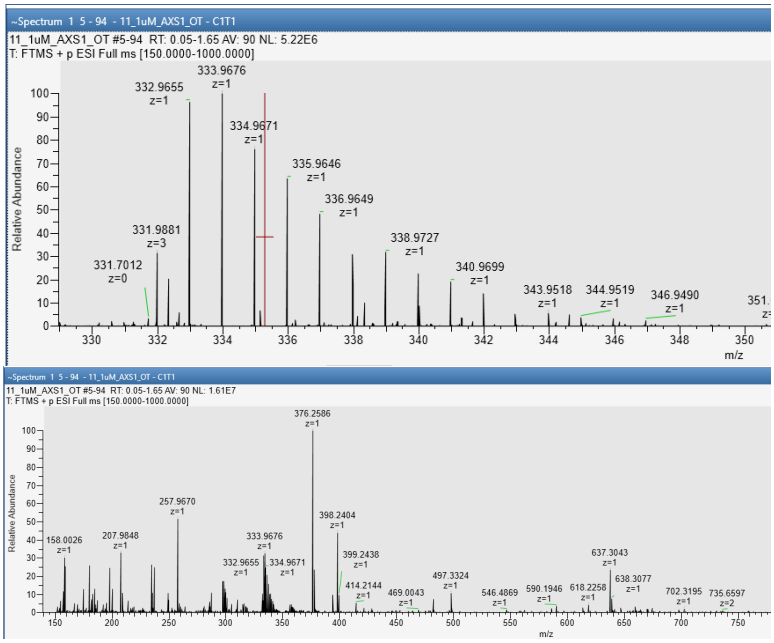

Figure 5-34. HRMS of oxoplatin zoomed in (top) and full scan (bottom) showing the expected peak of $[M+H]^+$ = 333.9676 m/z. The sample was dissolved with 0.1% formic acid to produce a 10 mM solution, serially diluted to 1 µM, and infused at 4 µL/min.

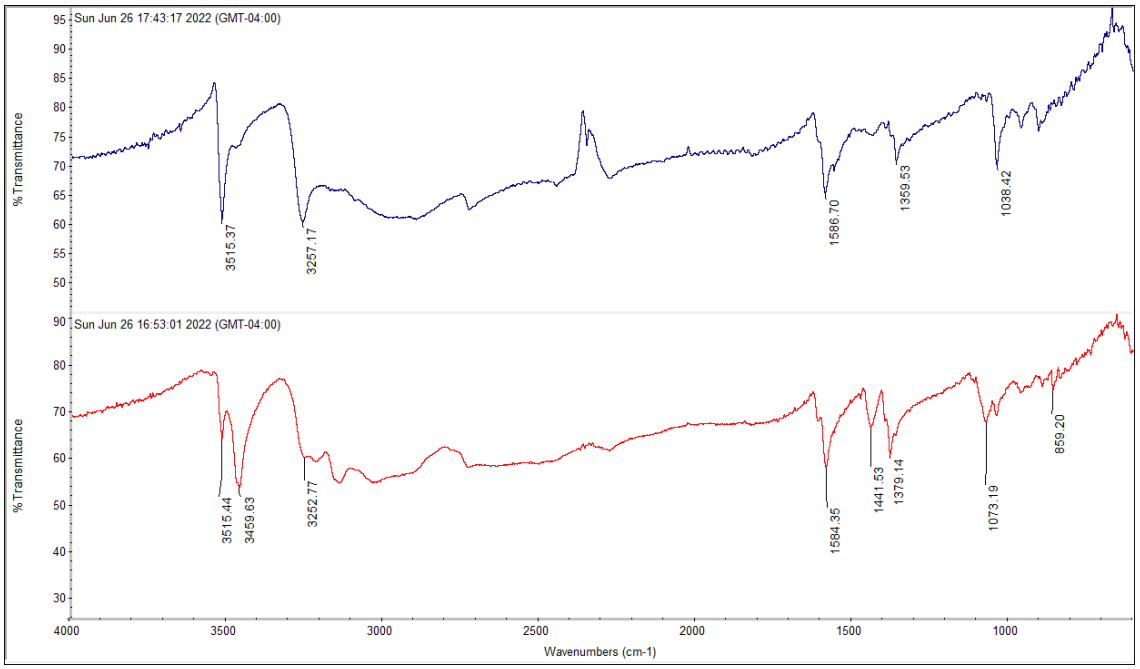

Figure 5-35. FT-IR (KBr, cm-1) of cisplatin and oxoplatin: cisplatin (top): 3515.37 (s), 3257.17 (s), 1586.70 (s), 1359.53 (w), and 1038.42 (s) and **1** (bottom): 3515.44 (w), 3459.63 (br, OH), 3252.77 (w), 1584.35 (s), 1441.53 (s), 1379.14 (s), 1073.19 (m, Pt-OH), 859.20 (w).

6,8-difluoro-7-hydroxy-4-methylcoumarin-cis-diamminehydroxyplatinum(IV)dichloro ester (1): The procedure for the synthesis of **1** was adapted from the literature[34]. Briefly, oxoplatin (1 equivalent) and 6,8-difluoro-7-hydroxy-4-methylcoumarin NHS ester (1.2 equivalences) were dissolved in DMSO (690 µL/10 mg of oxoplatin), and the mixture was stirred at 60 °C overnight in an oil bath. The solution was allowed to cool to room temperature and was added dropwise to excess diethyl ether (10−15 mL of diethyl ether per 1 mL of DMSO). After shaking the mixture, a two-phase system was obtained, and the diethyl ether phase was removed and discarded. The procedure was repeated until a sticky brown precipitate was obtained, which was then dissolved in methanol and precipitated by diethyl ether. **1** was isolated via centrifugation (4000 rpm, room temperature, 10 min), washed with diethyl ether, and air-dried. **1** was further purified by RP-HPLC. Retention time: 6.738 min (97.7% purity, **Figure 5-36**). **HRMS** (*m/z*, pos) $[M+H]^+$: expected, 585.22; observed, 585.99 (**Figure 5-37**). **^{1}H NMR** (400 MHz, ACN-d3, δ [ppm]): 1.77 (m, 2H), 2.11 (m, 4H), 2.33 (s, 3H), 3.65 (s, 2H), 5.19-5.45 (m, 5H), 7.32-7.35 (dd, 1H) (**Figure 5-38**). **^{195}Pt NMR** (86 MHz, DMSO-d6, δ [ppm]): 1036.60 (**Figure 5-39**).

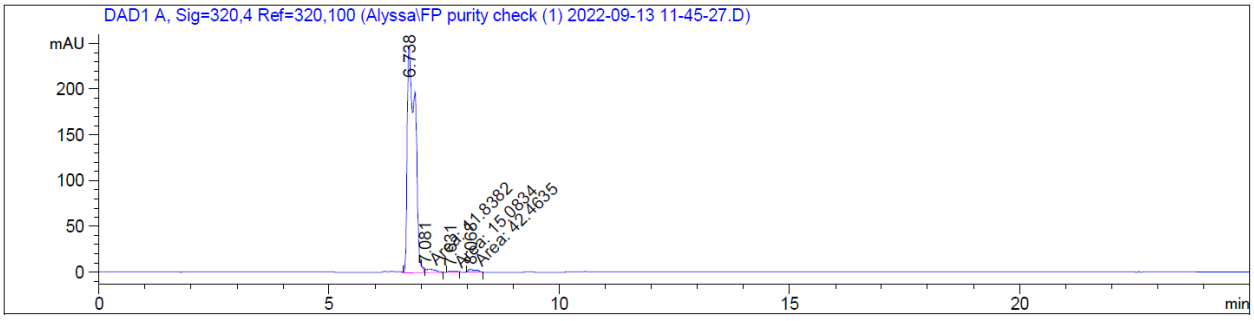

Figure 5-36. RP-HPLC purification trace of **fluoroplatin** with detection at 320 nm. The purity is 97.7% and all batches are ensured to be over 95% purity. **Fluoroplatin** eluted at a retention

time of 6.738 min. Solution A: 0.01% TFA in H2O, and solution B: 0.01% TFA in ACN. The method parameters were 5-60% B for 15 min, 95% B for 5 min, and 5% B for 5 min.

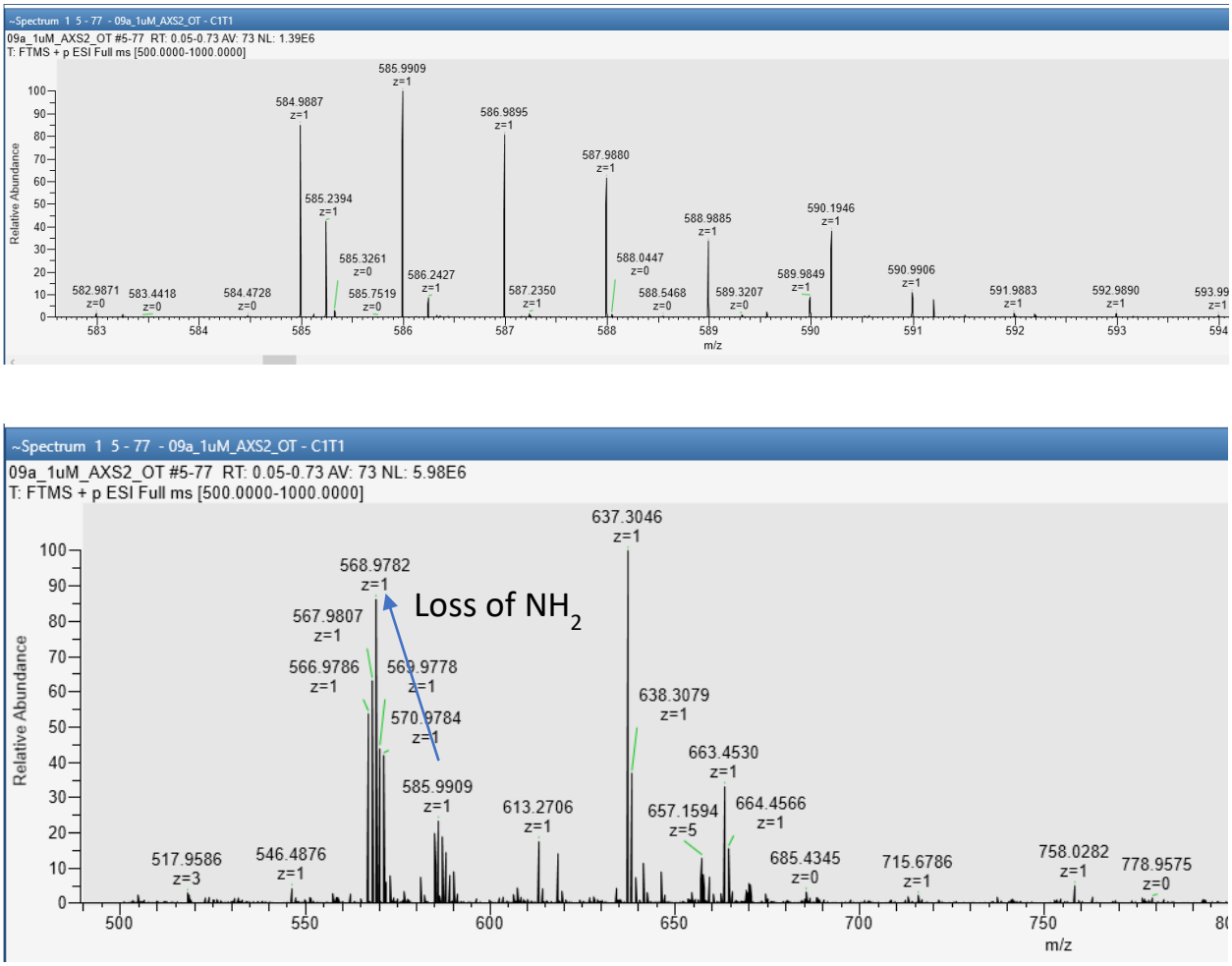

Figure 5-37. HRMS of **fluoroplatin** zoomed in (top) and full scan (bottom) showing the expected peak of $[M+H]^+$ = 585.9909. The sample was dissolved with 50% ACN with 0.1% formic acid to produce a 1 mM solution, serially diluted to 1 µM, and infused at 4 µL/min.

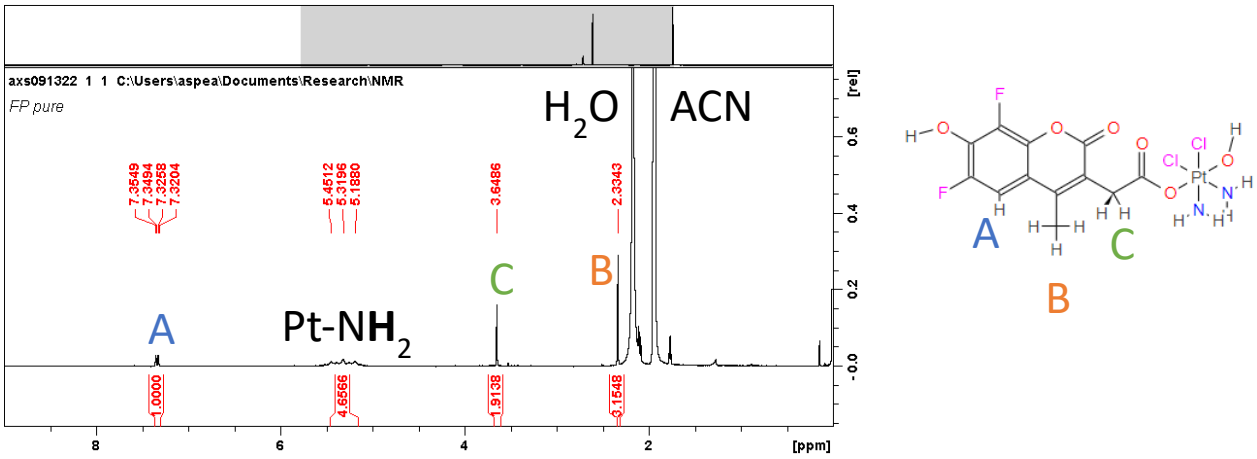

Figure 5-38. ^{1}H NMR (400 MHz, ACN-d3) of **fluoroplatin**: δ 1.7678 (m, 2H), 2.1066 (m, 4H), 2.3343 (s, 3H), 3.6486 (s, 2H), 5.1880-5.4512 (m, 5H), 7.3204-7.3549 (dd, 1H).

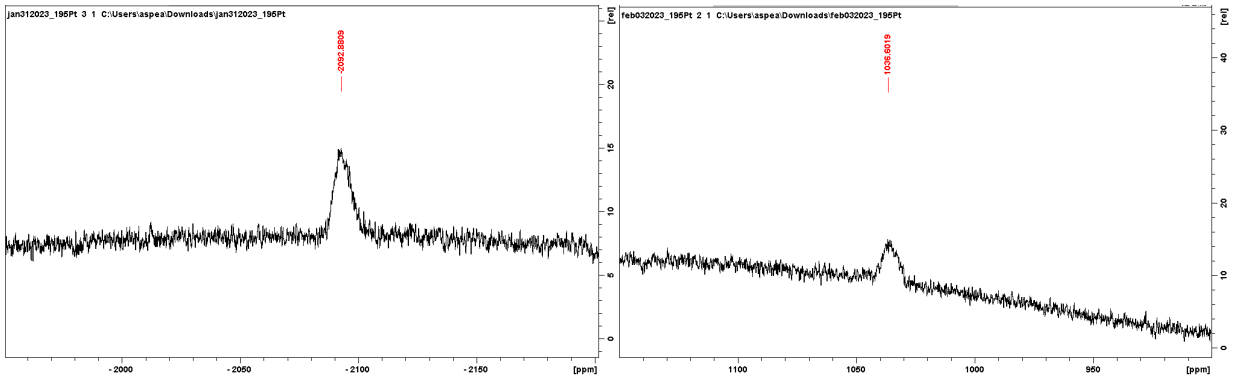

Figure 5-39. ^{195}Pt NMR (86 MHz; DMSO-d6) of cisplatin (left) δ (ppm): -2092.8809, and fluoroplatin (right): 1036.6019.

5.2.3 Aqueous stability of fluoroplatin

1 (0.2 mg) was taken up in 1 mL of HBSS with or without D-glucose in a 2 mL glass vial and capped. The samples were incubated at 37 °C for 24 hours and analyzed at 0-, 18-, and 24-hours using RP-HPLC at 360 nm.

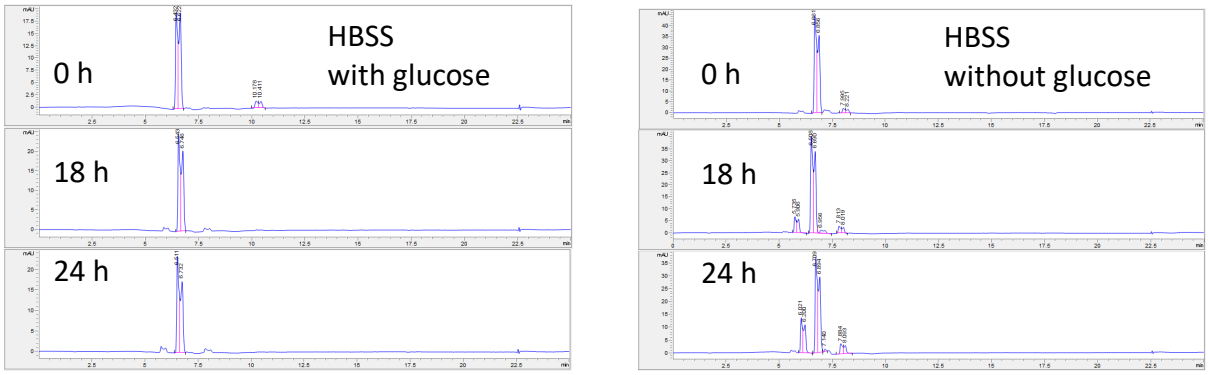

Figure 5-40. RP-HPLC tracking of aqueous stability. **Fluoroplatin** was taken up in 1 mL of HBSS (pH = 7.4, left), incubated at 37°C, and monitored using RP-HPLC at 320 nm over 24 h. A new peak was observed at a retention time of 5.8 min possibly due to the formation of a Pt(IV)-glucose conjugate. **Fluoroplatin** was then taken up in 1 mL HBSS (pH = 7.4) without D-glucose (right) resulting in no side products over 24 h.

5.2.4 Electronic absorption and fluorescence spectroscopy.

1 (30 mM) was taken up in HBSS and an electronic absorbance spectrum was collected from 200-800 nm. The resultant absorbance maximum was used as the excitation wavelength for subsequent fluorescence studies.

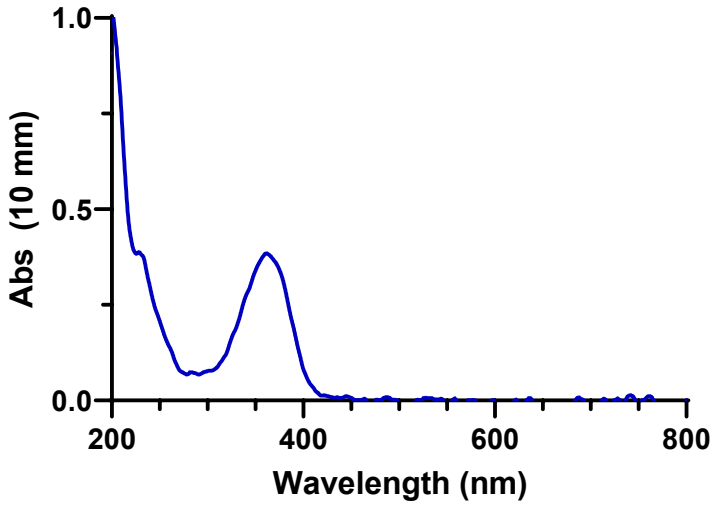

Figure 5-41. Electronic absorbance (10 mm path length) of **fluoroplatin** (0.03 M) in HBSS (pH = 7.4, no glucose). λmax = 363 nm.

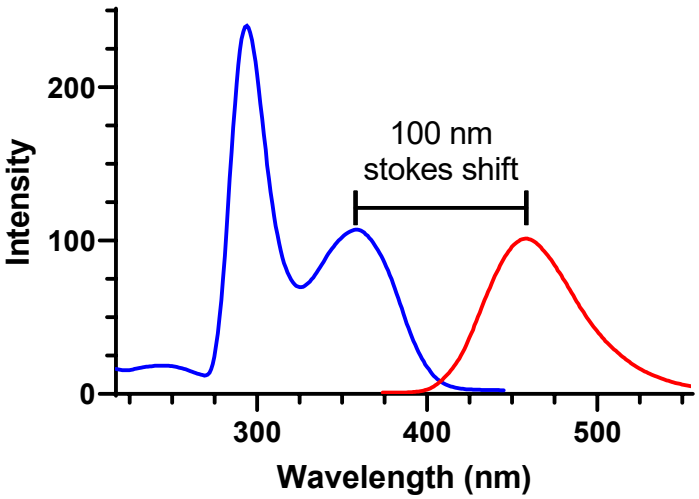

Figure 5-42. Fluorescence excitation and emission of **fluoroplatin** (2 mM) resulted in λ_{Ex} = 359 nm and λ_{Em} = 459 nm for a large stokes shift of 100 nm beneficial for the reduction of band overlap and background interference.

5.2.5 Model intracellular reduction reaction

1 was subject to a model reducing environment of 1 mM GSH in HBSS (**Scheme 2**). Fluorescence spectroscopy, RP-HPLC, and HRMS experiments were then done to describe the reduction products and time course.

Reduction of **1** tracked via RP-HPLC

A solution of 0.47 mM **1** and 1 mM GSH was made in 1 mL of 5% ACN/H_2O and adjusted to pH ~7.2 with 1 M NaOH. The solution was stirred at room temperature and aliquots were taken at 0, 1, and 3 hours for RP-HPLC analysis and reaction tracking. The diode array detector was set to a signal of 320 nm to track the fluorophore.

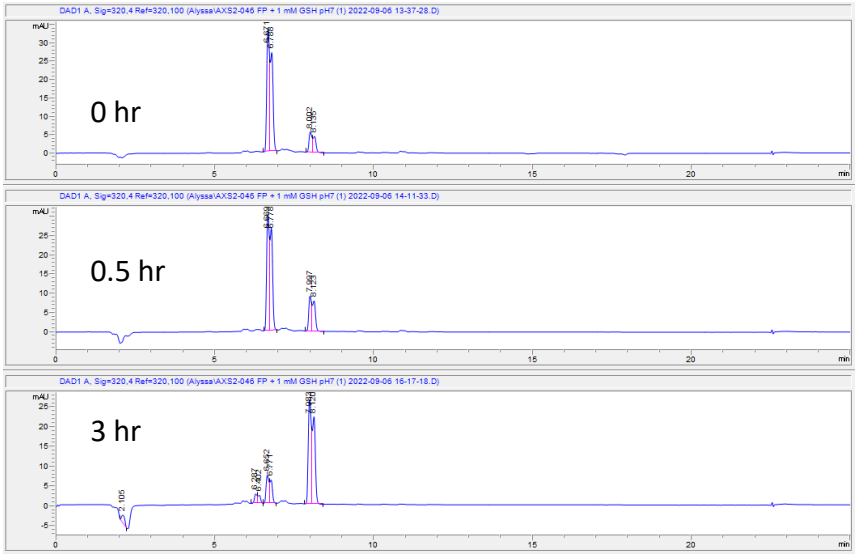

Figure 5-43. RP-HPLC tracking of reduction reaction progression. A mixture of 0.47 mM **fluoroplatin** and 1 mM GSH was made in 1 mL of 5% ACN/H2O and adjusted to pH ~7.2 with 1 M NaOH. The solution was stirred at room temperature and aliquots were taken periodically for RP-HPLC analysis and reaction tracking. The reduction product **2** was observed to form over the course of 3 h. Cisplatin cannot be tracked via RP-HPLC due to its lack of absorbance in detectable ranges.

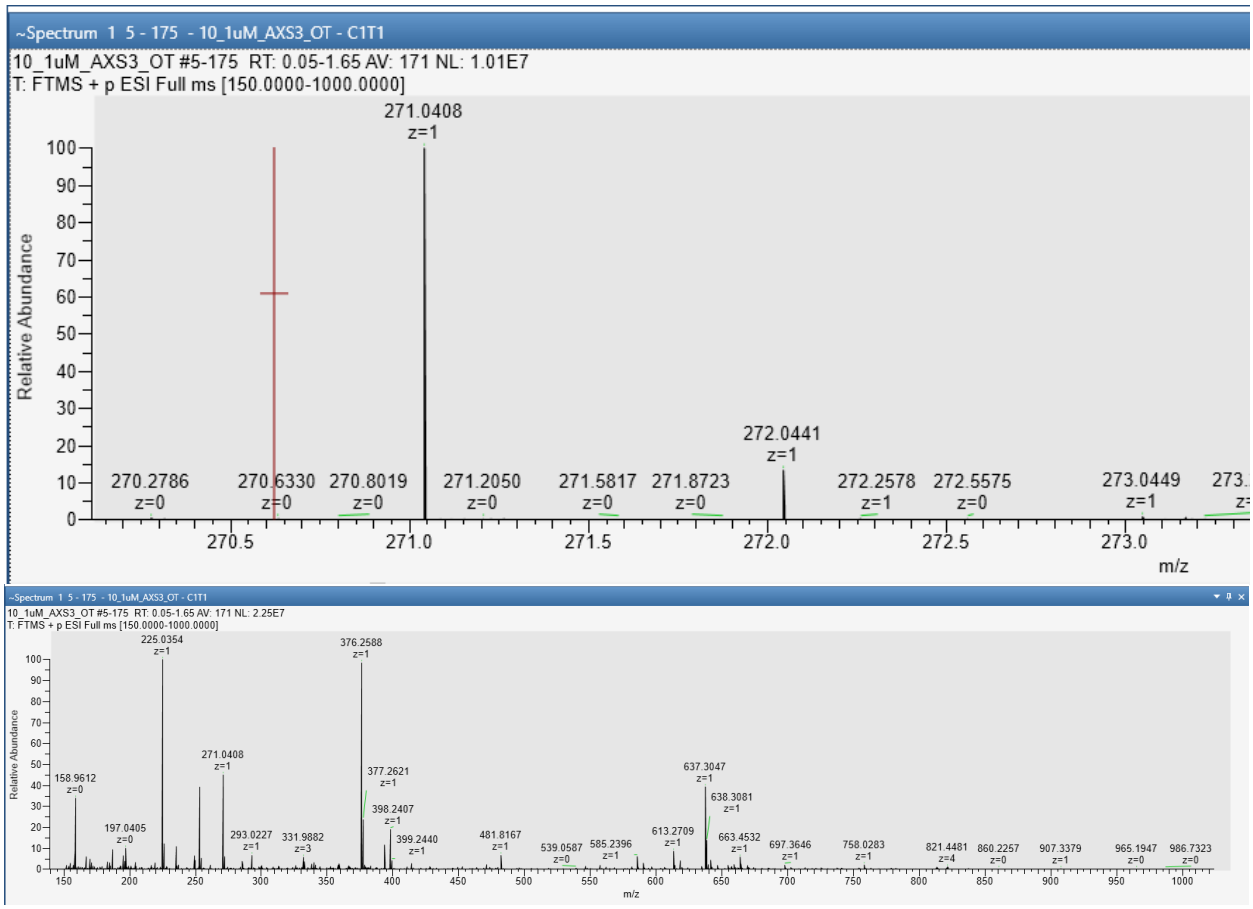

Figure 5-44. HRMS of **2** zoomed in (top) and full scan (bottom) showing the expected peak of $[M+H]^+$ = 271.0408 m/z. The sample was dissolved with 50% ACN with 0.1% formic acid to produce a 10 mM solution, serially diluted to 1 µM, and infused at 4 µL/min.

Reduction of **1** tracked via fluorescence excitation/emission.

Glutathione, typically at intracellular concentrations of 1-10 mM[117], was used at a concentration of 1 mM and combined with **1** (2 mM) in HBSS. Emission spectra were collected at 0, 1, and 3 hours after the addition of GSH from 367-567 nm with slit widths of 5 mm. The corresponding excitation spectra were then collected from 200-448 nm also with slit widths of 5 mm.

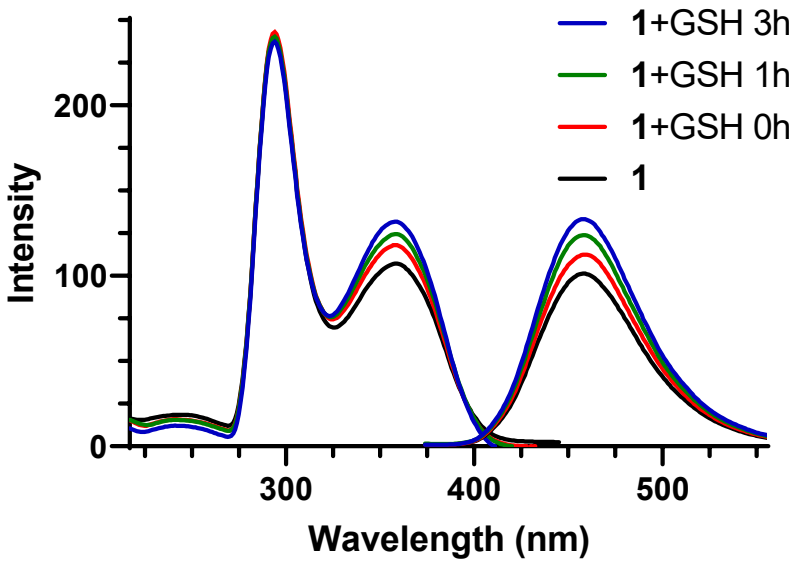

Figure 5-45. Fluorescence excitation and emission of **fluoroplatin** (2 mM) in HBSS (pH = 7.4, no glucose) with the addition of 1 mM GSH at 0, 1, and 3 h. Emission spectra were collected at an excitation wavelength of 363 nm and 5 mm slit widths.

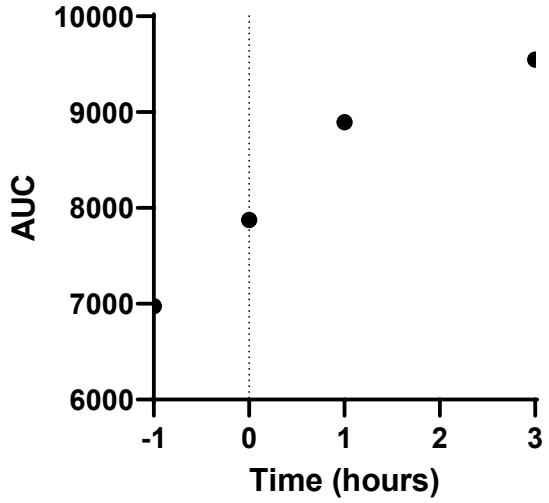

Figure 5-46. The Area Under the Curve (AUC) of **fluoroplatin** emission increased over time with 0 h marking the addition of GSH; this is consistent with reductive release of the fluorophore and the absence of fluorescent quenching by Pt.

5.2.6 Cellular uptake of **1**

Approximately 750,000 HEK-293 cells were seeded in an imaging dish and incubated for 24 hours at 37 °C with 5% CO_2 atmosphere. When ~70% confluency was achieved, the media was removed and replaced with fresh media containing 1 µM of **1**. The cells were incubated for 1 hour after which the media was aspirated and replaced with PBS containing the counterstain RedDot 1. The cells were incubated for an additional 5 minutes before imaging. 4',6-diamidino-2-phenylindole (DAPI) and Cyanine-5 (Cy-5) filter presets were used to detect **1** and RedDot 1, respectively. A z-stack was acquired to determine internalization of **1** at a 20 µm depth (0.21 µm interval, 97 slices).

5.2.7 Anti-proliferative activity of **1**

Approximately 5,000 HEK-293 cells per well were plated in a 96 well plate and allowed to adhere in phenol red-free DMEM with 15% FBS. Cisplatin or **1** was added to the wells to obtain final concentrations of 5-50 µM along with a drug-free control. The samples were incubated at 37 °C with 5% CO_2 atmosphere for 5 hours. The media was aspirated and replaced with fresh media with no drug and allowed to grow overnight. 10 µL of CCK-8 reagent was added to each well and incubated for another 2 hours after which the optical density was read on a microplate reader at 450 nm. All experiments were performed in parallel and in triplicate.

5.3 Chapter 4 Experimental

5.3.1 General methods and instrumentation

Dimethylformamide (DMF), dichloromethane (DCM), diethyl ether, trifluoroacetic acid (TFA), triisopropyl silane (TIPS), *N,N*'-diisopropylcarbodiimide (DIC), piperidine, NaCl, alpha-

cyano-4-hydroxy-cinnamic acid (CHCA), and HPLC grade acetonitrile (MeCN) were purchased from Sigma Aldrich (Milwaukee, WI, USA). Fmoc-protected amino acids, Oxyma Pure, and ProTide rink-amide resin were purchased from CEM (Matthews, NC, USA). Dithiothreitol (DTT) was purchased from MP Biomedicals, LLC (Solon, OH, USA).

Deionized water was prepared in-house and filtered through a Nalgene Rapid-Flow 0.2 µm PES vacuum filter prior to use. 50 mM HEPES solution was prepared by dissolving 11.915 HEPES free acid and 6.83 g NaCl in a total volume of 1 L of deionized water and adjusting the pH to 7.

Peptides were synthesized in-house on a microwave assisted CEM Liberty Blue peptide synthesizer and cleaved from the support resin using a CEM Razor. Reverse-phase high performance liquid chromatography (RP-HPLC) was performed on an Agilent 1100 Series instrument with an Agilent ZORBAX 300SB-C8 (5 µm, 9.4 x 250 mm), Agilent Eclipse XDB-C18 column (3.5 µm, 4.6 x 100 mm), or Agilent Eclipse XDB-C18 column (5 µm, 4.6 x 150 mm). MALDI-TOF MS was conducted on a Bruker microflex with an MSP 96 polished steel BC target and CHCA matrix. High resolution mass spectrometry (HRMS) was performed on a Thermo Orbitrap Fusion Lumos at the SUNY Upstate Proteomics & Mass Spectrometry Core Facility.

5.3.2 HPLC Methods

All HPLC analyses were done in reverse phase with a gradient system of 0.1% TFA in water (solvent A) and 0.1% TFA in MeCN (solvent B). The diode array detector was set to 280 nm and 360 nm to detect the peptides and Cbi, respectively. In the case a peptide did not have an aromatic residue to detect at 280 nm, 215 nm was used to detect peptide bonds.

Method A was used for peptide purification and developed on an Agilent ZORBAX 300SB-C8 column (5 µm, 9.4 x 250 mm) using the following gradient: 10%-75% ACN over 15 min, 95% ACN for 5 min, 10% ACN for 5 min.

Methods B-D were used for analytical studies. Method B was developed on an Eclipse Plus C18 column (3.5 µm, 4.6 x 100 mm) using the following gradient: 1-70% ACN for 15 min, 95% ACN for 5 min, 1% ACN for 5 min. Method C was developed on an Agilent Eclipse XDB-C18 column (5 µm, 4.6 x 150 mm) using the following gradient: 18% ACN for 5 min, 18-60% ACN for 5 min, 95% ACN for 2.5 min, 18% ACN for 2.5 min. Method D was developed on an Agilent Eclipse XDB-C18 column (5 µm, 4.6 x 150 mm) using the following gradient: 20% ACN for 5 min, 20-75% ACN for 5 min, 95% ACN for 2.5 min, 20% ACN for 2.5 min.

5.3.3 Peptide synthesis

Peptides were synthesized following solid-phase chemistry at a 0.025 mmol scale on rink amide resin on an automatic peptide synthesizer. Fmoc-protected amino acids were prepared at 0.2 M in DMF. The activator and activator base used for coupling were Oxyma Pure (0.25 M) and DIC (0.125 M), respectively. The deprotection reagent used between couplings was 20% piperidine in DMF.

After synthesis, the resin-bound peptides were transferred to the cleavage instrument with DCM, the DCM was removed under vacuum filtration, and the deprotection/cleavage solution was added (95% TFA, 2.5% TIPS, and 2.5% H_2O) and left to incubate for 40-45 min at 40°C. The peptides were precipitated with cold (-20°C) diethyl ether and centrifuged for 10 min at 4,000 rpm to obtain a crude pellet.

Purification was achieved by RP-HPLC using Method A. The peptide was then flash frozen with liquid nitrogen and lyophilized to a dry powder. Purity traces were obtained using Methods B-D and >90% purity was ensured before further experimentation.

5.3.4 Cbi synthesis

Cbi was prepared in-house as described by *Gryko et al*.,[20] however, it is commercially available from Sigma-Aldrich. Cyanocobalamin (100 mg, 0.074 mmol), NaCN (13 mg, 0.25 mmol), and EtOH (6.6 mL) were added to a microwave reaction vessel with a magnetic stir bar and sealed with a cap. The vessel was heated to 120 °C for 10 min using 300 W. The mixture was transferred to a flask using EtOH and reduced to minimal volume by rotary evaporation. The concentrated mixture was then loaded onto a normal phase flash chromatography cartridge and eluted using an isocratic method of MeOH in EtOAc (2:1 v:v) at a flow rate of 5 mL/min. The major violet fraction was isolated, dried by rotary evaporation, dissolved in iPrOH, and vacuum filtered through a celite plug to remove any excess cyanide and silica. The filtrate was then dried, redissolved in water, and lyophilized. ^{1}H NMR (400 MHz, D_2O) δ 5.891 (s, 1H), 3.907 (m, *J*=5.95 Hz, 1H), 3.839 (d, *J*=8.23, 1H), 3.748 (d, *J*=10.44, 1H), 3.654 (q, *J*=7.11, 2H), 3.572 (q, *J*=7.08 Hz, 1H), 3.404 (dd, *J*=7.00,4.78, 1H), 3.312-3.151 (3H, overlapped), 2.914-2.857 (m, 1H), 2.748-2.712 (m, 4H), 2.600-2.380 (6H, overlapped), 2.316-2.231 (14H, overlapped), 2.148-2.069 (m, 4H), 2.030-1.943 (m, 1H), 1.915 (s, 3H), 1.891-1.744 (m, 3H), 1.683 (s, 3H), 1.532 (s, 3H), 1.489 (s, 3H), 1.430 (s, 3H), 1.312 (s, 3H), 1.184 (t, *J*=7.12 Hz, 7H), 1.151 (d, *J*=6.36 Hz, 3H); UV−vis (H_2O) λ 276, 312, 367, 503, 539, 580 nm; MS (MALDI-TOF) calculated for $C_{48}H_{73}CoN_{11}O_8$ ($[M -2CN+H]^+$) 991.11, found 990.72; HPLC t_R values on method B: 1.839 and 2.105 min; method C: 1.989 and 2.837 ; and method D: 1.852 and 2.282.

5.3.5 Detailed Peptide Oxidation Reactions

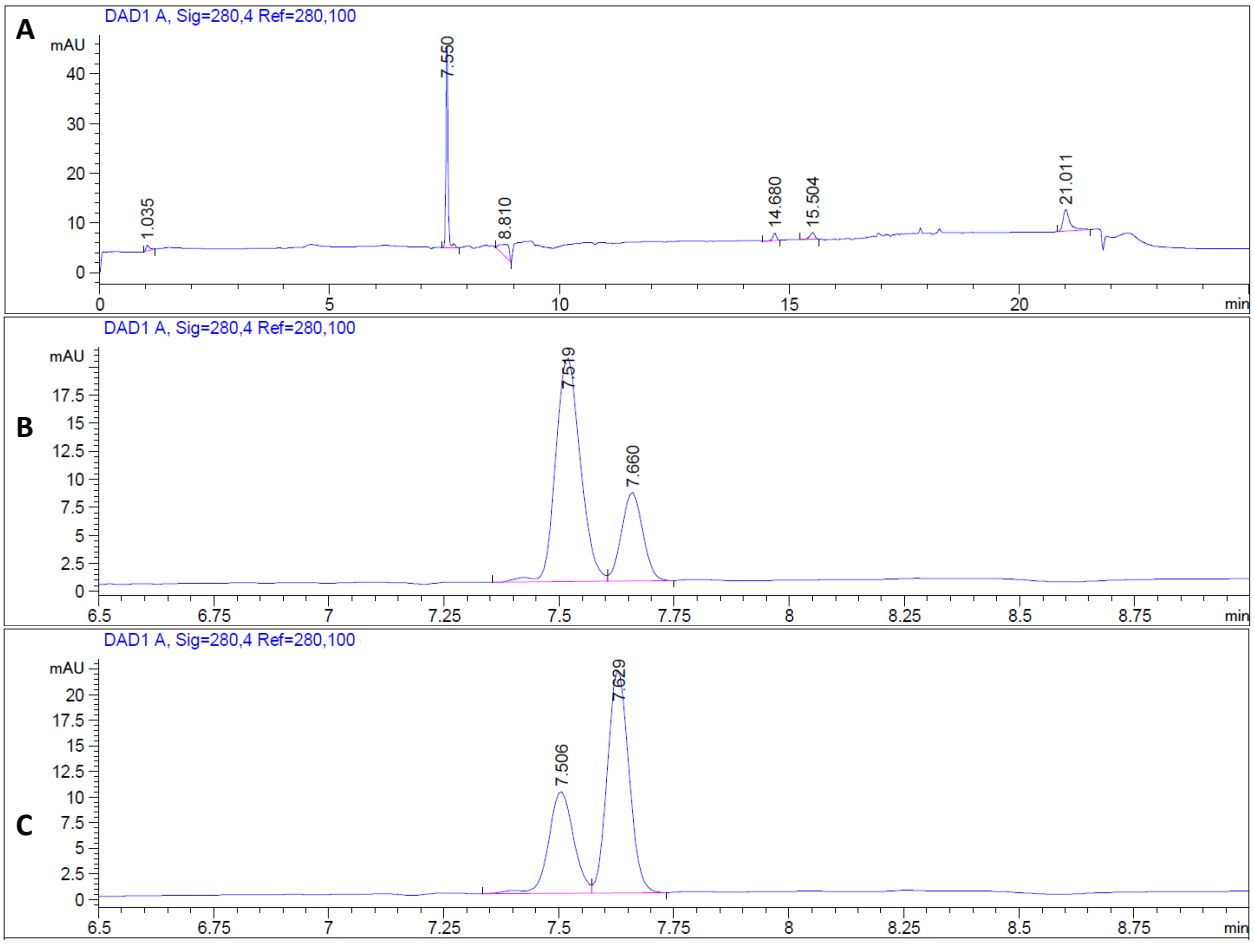

Figure 5-47. HPLC traces (280 nm) of **OT**: (A) a full range trace of oxidized **OT** with a retention time of 7.550 min, (B) a zoomed in trace of 1 mM **OT** treated with 10 mM of DTT upon initial mixing, and (C) a zoomed in trace of 1 mM **OT** treated with 10 mM of DTT after 25 min of mixing. The oxidized **OT** peak at 7.506 min shrinks and the reduced **OT** peak at 7.629 min grows in as the DTT reduces the **OT**.

A

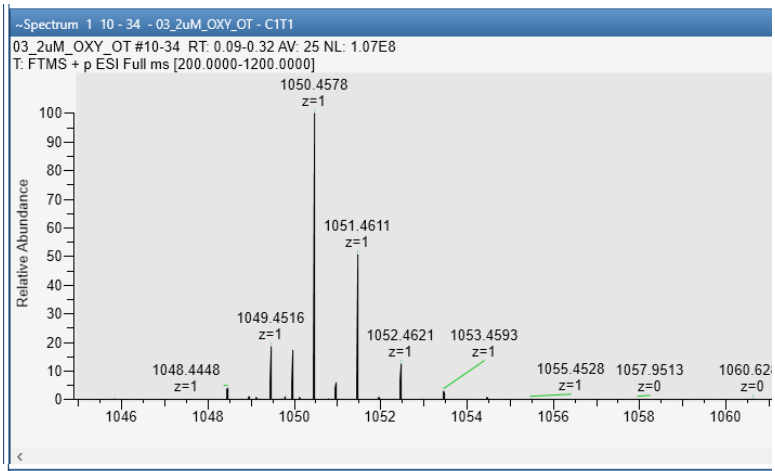
~Spectrum 1 10 - 34 - 03_2uM_OXY_OT - C1T1
03_2uM_OXY_OT #10-34 RT: 0.09-0.32 AV: 25 NL: 1.07E8
T: FTMS + p ESI Full ms [200.0000-1200.0000]
Relative Abundance
1050.4578 z=1
1051.4611 z=1
1049.4516 z=1
1052.4621 z=1
1053.4593 z=1
1048.4448 z=1
1055.4528 z=1
1057.9513 z=0
1060.62 z=0

B

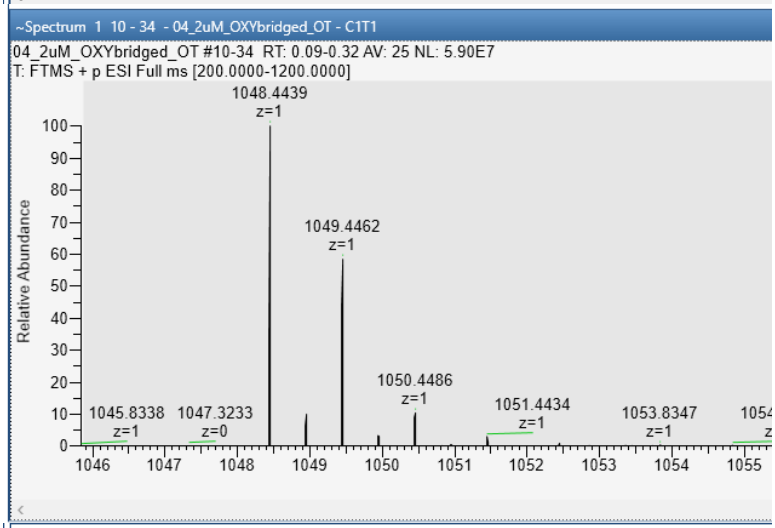
~Spectrum 1 10 - 34 - 04_2uM_OXYbridged_OT - C1T1
04_2uM_OXYbridged_OT #10-34 RT: 0.09-0.32 AV: 25 NL: 5.90E7
T: FTMS + p ESI Full ms [200.0000-1200.0000]
Relative Abundance
1048.4439 z=1
1049.4462 z=1
1050.4486 z=1
1045.8338 z=1
1047.3233 z=0
1051.4434 z=1
1053.8347 z=1

C

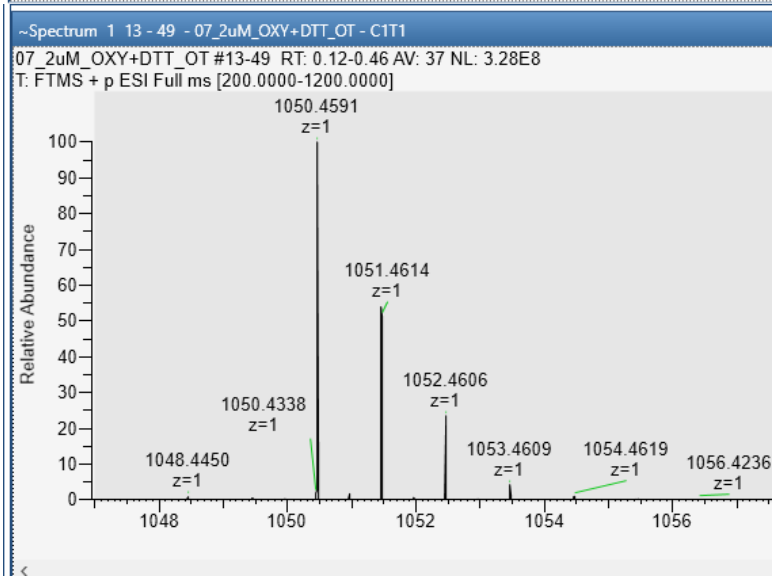
~Spectrum 1 13 - 49 - 07_2uM_OXY+DTT_OT - C1T1
07_2uM_OXY+DTT_OT #13-49 RT: 0.12-0.46 AV: 37 NL: 3.28E8
T: FTMS + p ESI Full ms [200.0000-1200.0000]
Relative Abundance
1050.4591 z=1
1051.4614 z=1
1052.4606 z=1
1050.4338 z=1
1048.4450 z=1
1053.4609 z=1
1054.4619 z=1
1056.4236 z=1

Figure 5-48. HRMS of (A) reduced **OT** with the expected mass of 1050 m/z, (B) oxidized **OT** with the expected mass of 1048 m/z, and (C) oxidized **OT** reacted with DTT with the expected mass of 1050 m/z.

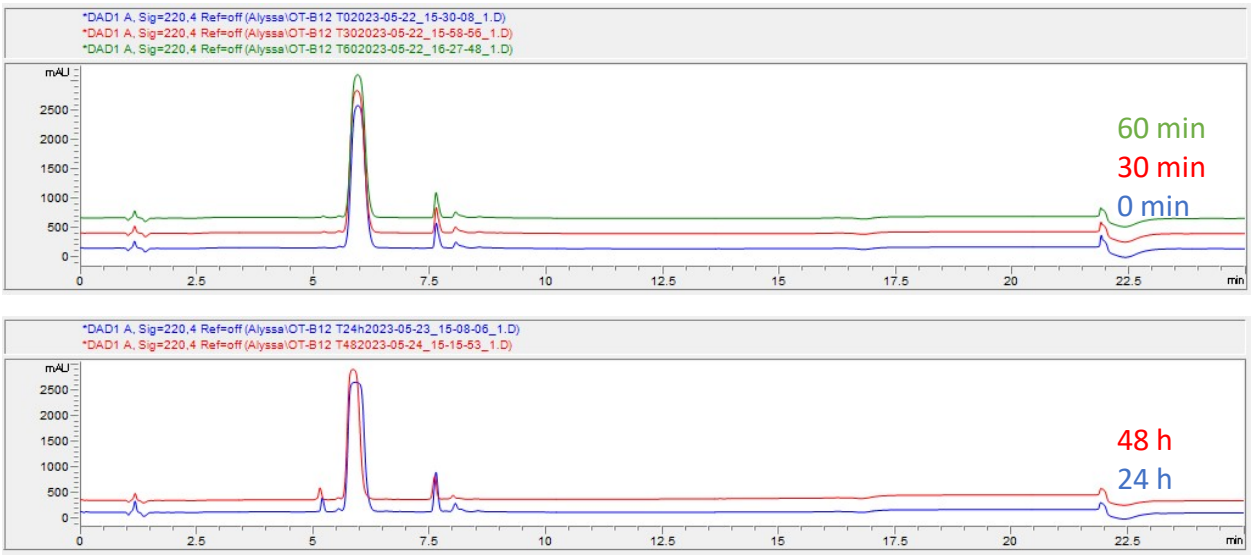

Figure 5-49. HPLC traces (280 nm) of **OT** reacted with B_{12} via method B over 48 hours. The large band at 6 min is B_{12} while OT was observed at ~7.63 min consistent with its reduced state. Side-products were detected at ~5.2 and ~8.0 min but their identities could not be confirmed.

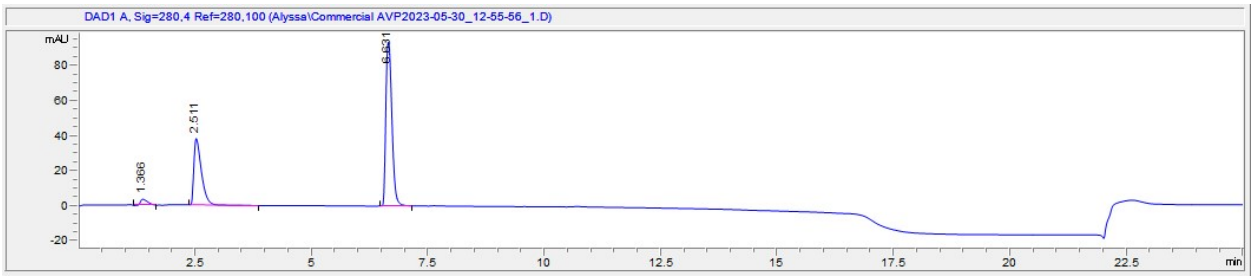

Figure 5-50. HPLC trace of **AVP** commercial standard showing the oxidized peptide retention time at 6.631 min on method B.

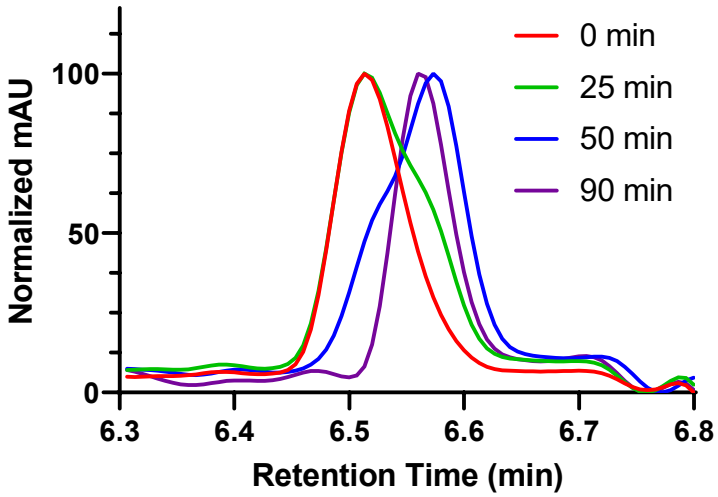

Figure 5-51. HPLC traces (280 nm) of **AVP** upon reaction with Cbi showing an elution time shift from 6.494 min to 6.527 min in 90 min on method B.

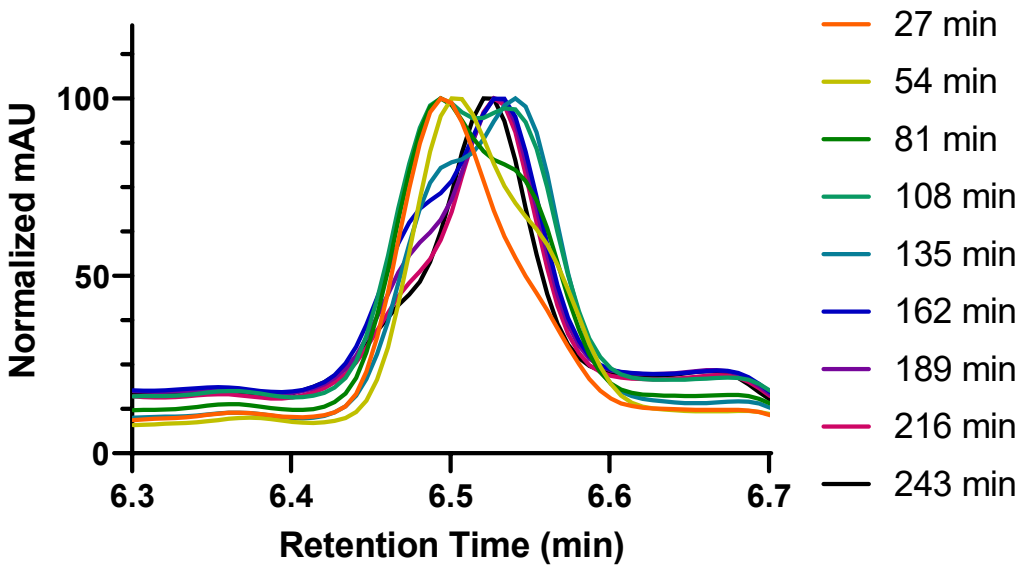

Figure 5-52. HPLC traces (280 nm) of **AVP** upon reaction with Cbi in degassed H_2O on method B. These experiments were performed in a 2 mL auto sampling vial with a septum cap at room temperature. The reaction progressed to completion after 4 hours possibly due to air entering the vial when the auto sampling needle punctures the septum; this reaction time is in opposition to 90 minutes when the reaction is open to air.

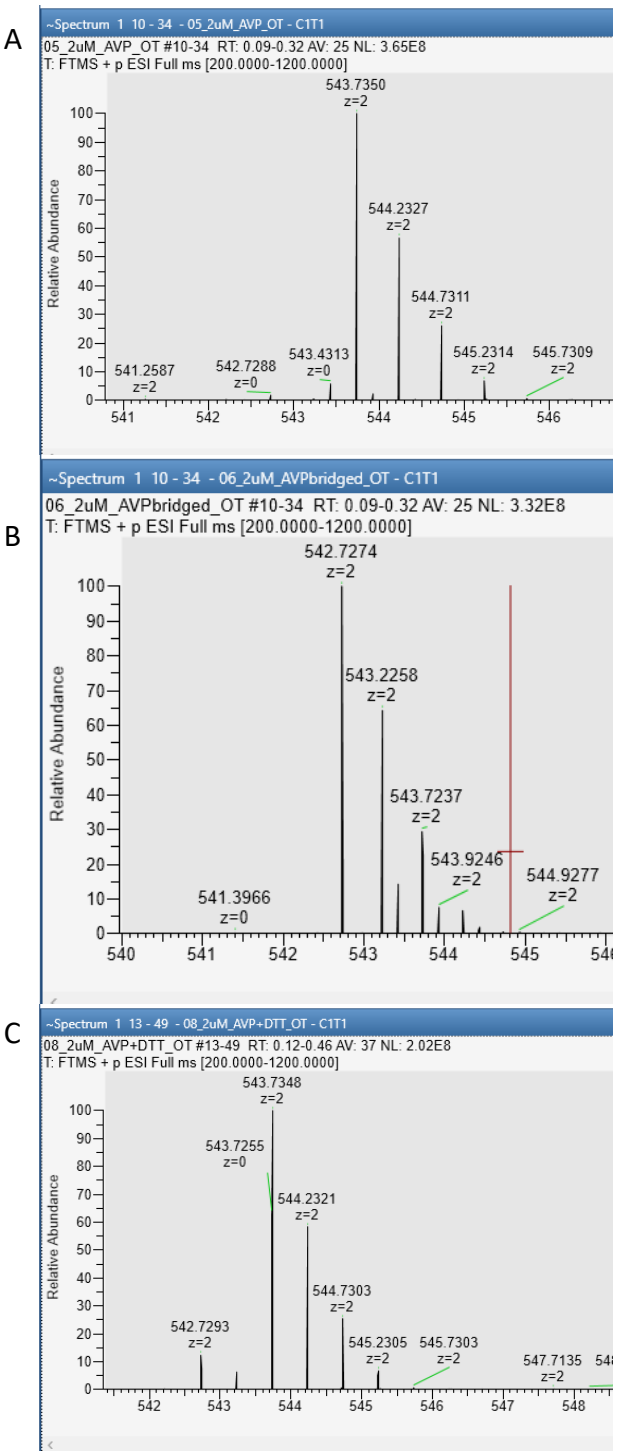

Figure 5-53. HRMS of (A) reduced **AVP** with the expected mass of 543 m/z (z=2, 1086 parent mass), (B) oxidized **AVP** with the expected mass of 542 m/z (z=2, 1084 parent mass), and (C) oxidized AVP reacted with DTT with the expected mass of 543 m/z (z=2, 1086 parent mass).

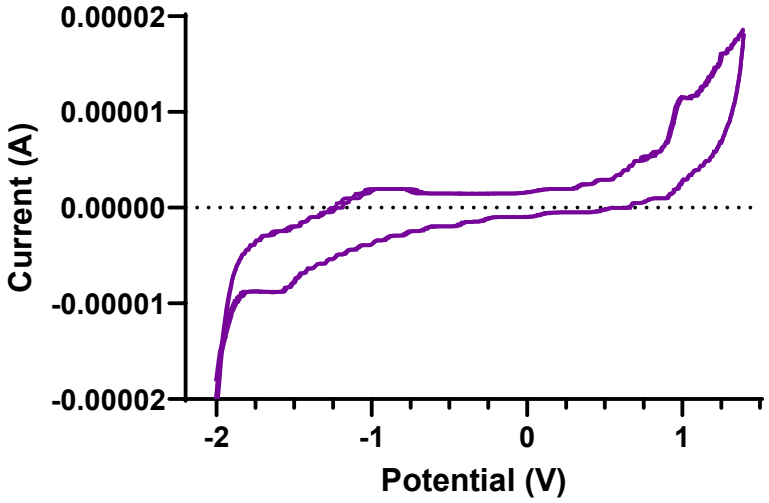

Figure 5-54. Cyclic Voltammogram of dicyanocobinamide (Cbi). Measurements were carried out in DMF at a scan rate of 100 mV s^{-1} with Fc/Fc^{+} employed as an internal standard and are reported vs. Fc/Fc^{+}.

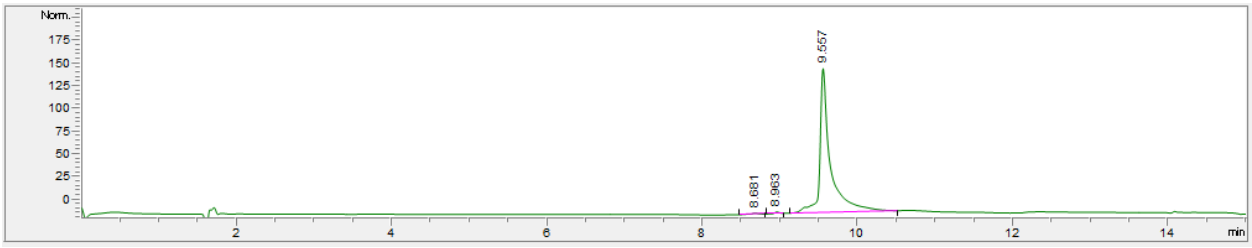

Figure 5-55. HPLC purity trace of **SST** showing an elution time of 9.557 min and purity of 98.9% on method C.

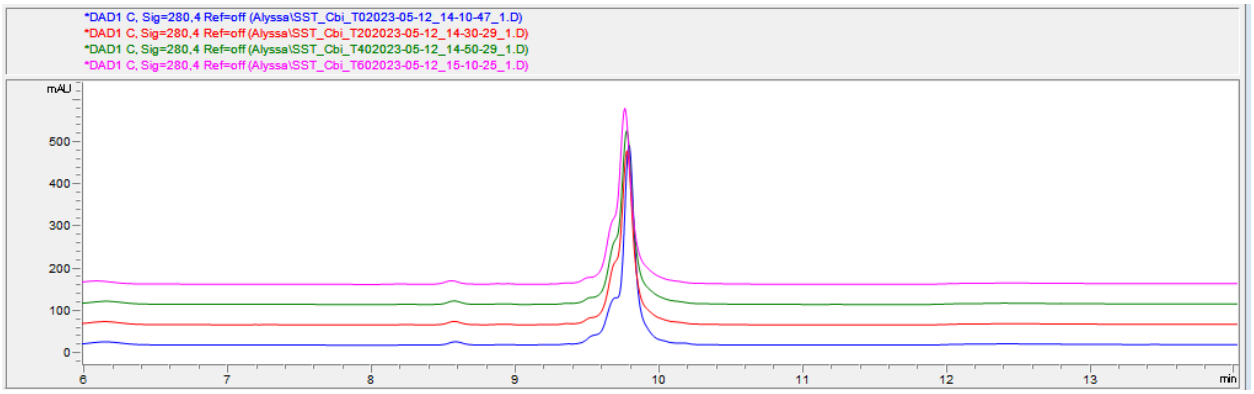

Figure 5-56. HPLC traces of **SST** oxidation with Cbi for 1 hour showing no shift in elution time over the course of oxidation on method C.

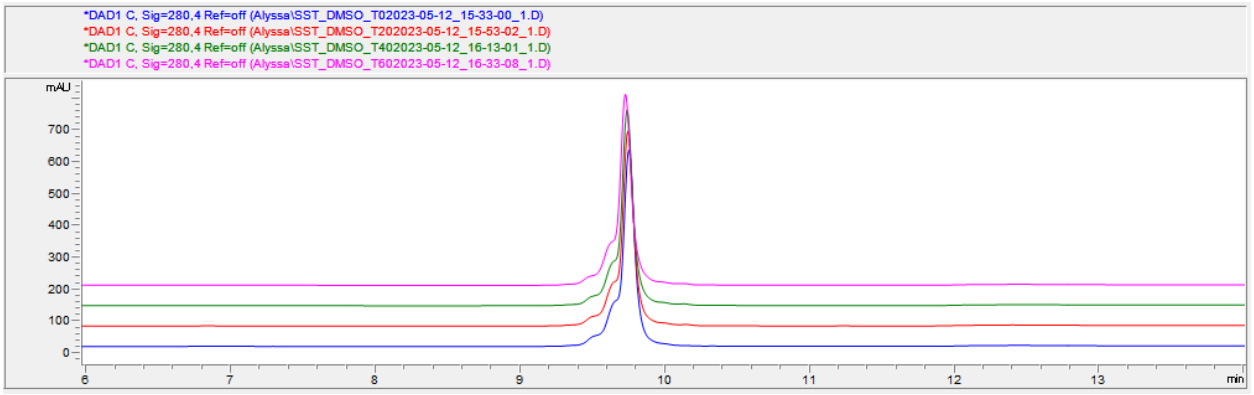

Figure 5-57. HPLC traces of **SST** oxidation with DMSO for 1 hour showing no shift in elution time over the course of oxidation on method C.

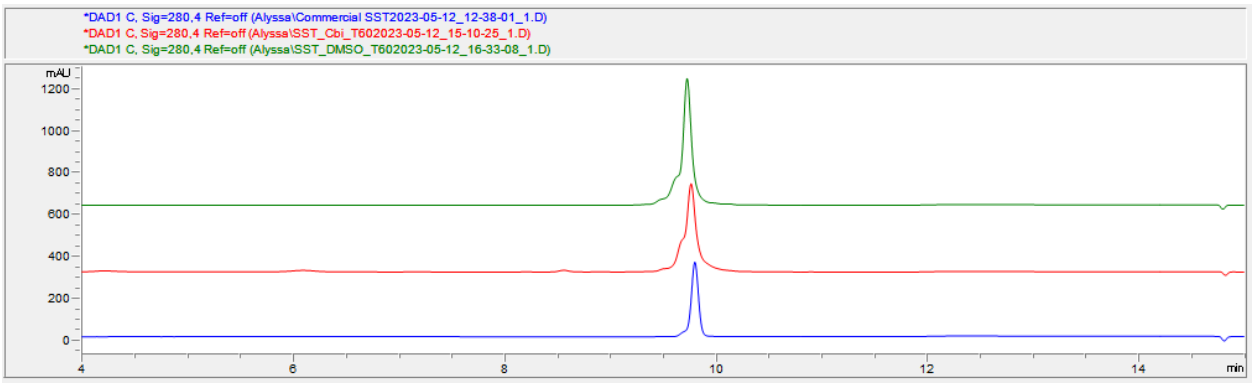

Figure 5-58. HPLC trace of **SST** reacted with Cbi or DMSO for 1 hour and a commercial **SST** standard all showing the same retention time shift of ~9.5 min on method C.

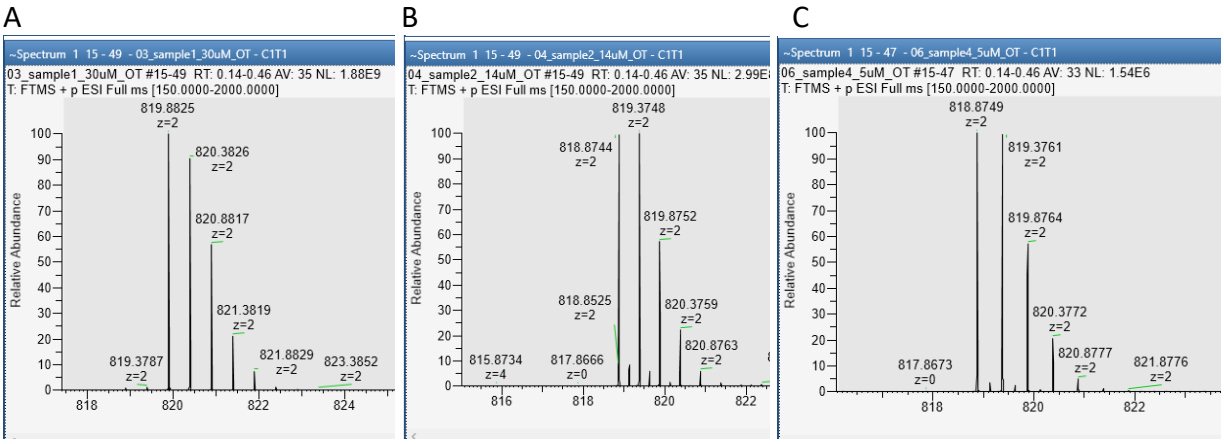

Figure 5-59. HRMS of (A) **SST** reduced with the expected mass of 819.8825 m/z (z=2, 1637.764 monoisotopic mass), (B) oxidized **SST** reacted with Cbi with 1 hour with the expected mass of 818.844 m/z (z=2, 1635.749 monoisotopic mass), and (C) **SST** oxidized with DMSO for 48 hours with the expected mass of 818.875 m/z (z=2, 1635.749 monoisotopic mass).

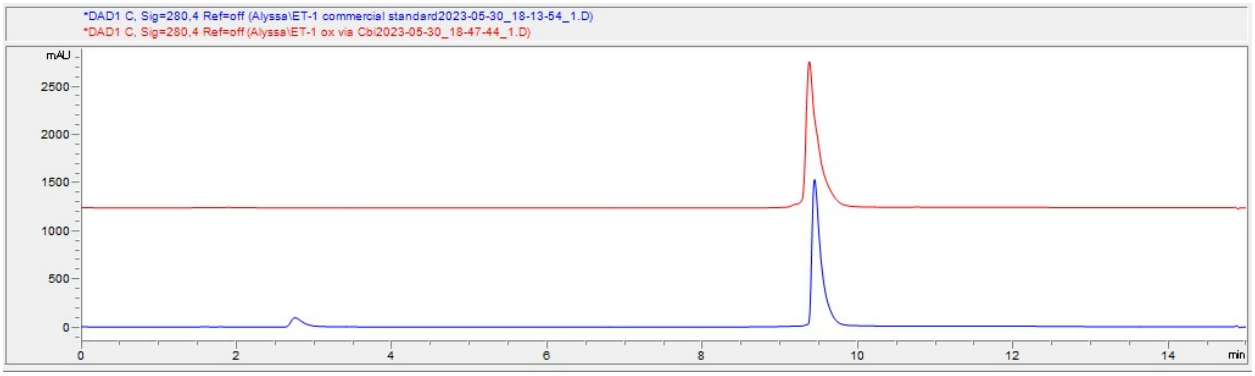

Figure 5-60. HPLC purity trace of **ET-1** reacted with Cbi for 1 hour and commercial standard on method D with elution times of 9.377 and 9.446 minutes, respectively.

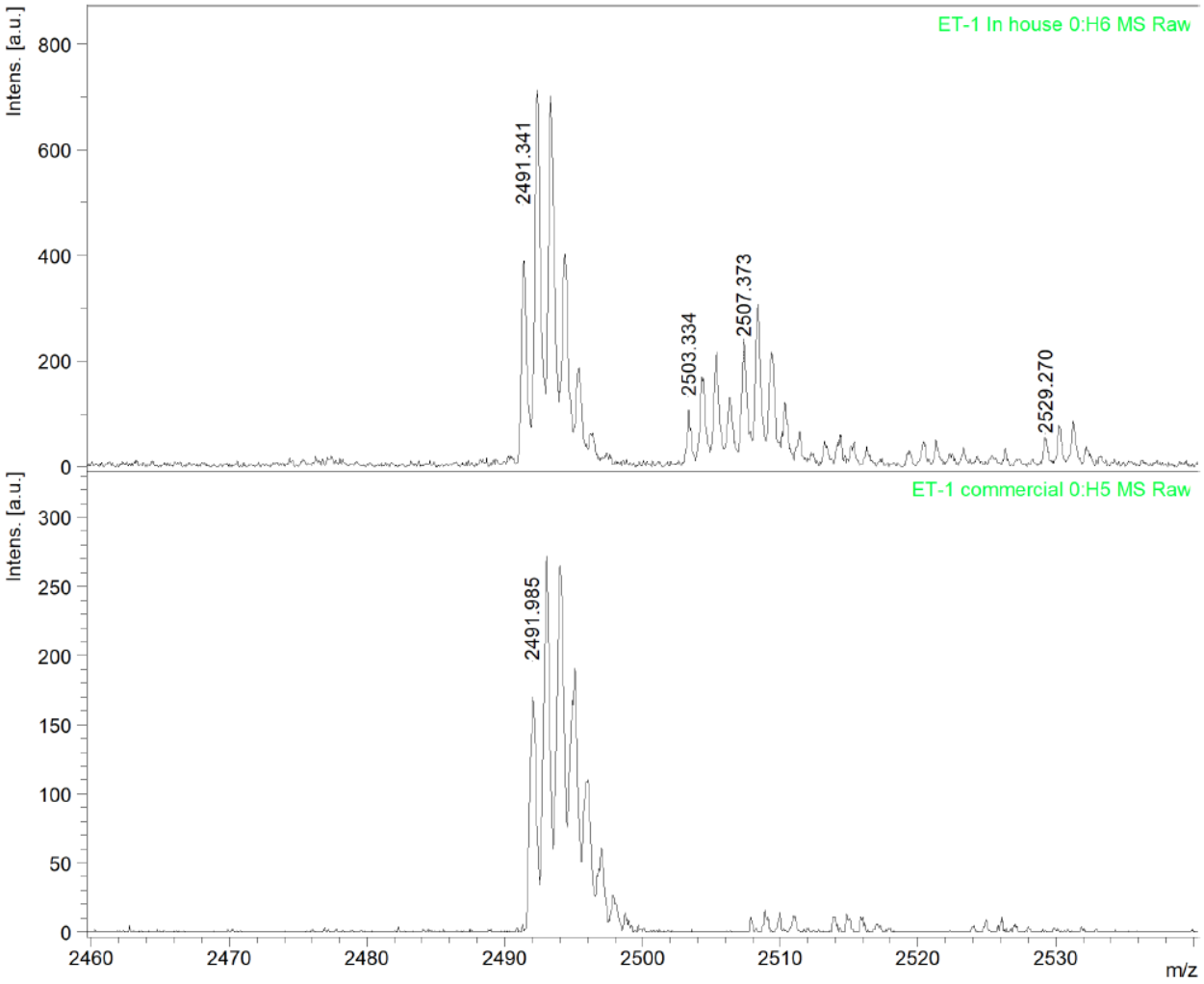

Figure 5-61. MALDI-ToF MS of (top) **ET-1** oxidized with Cbi after 1 hour and (bottom) commercial **ET-1**.

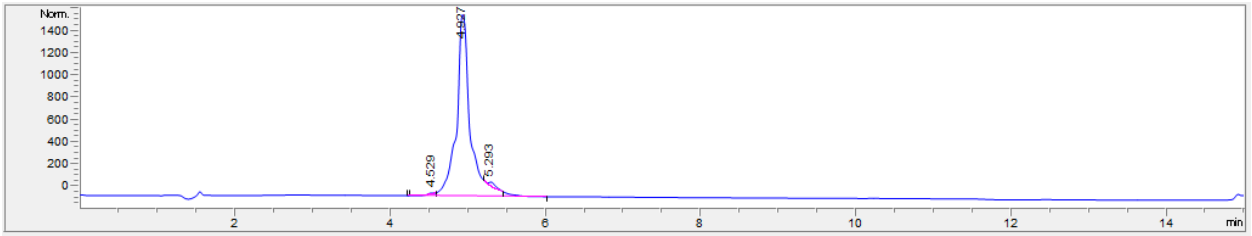

Figure 5-62. ***Tr*CART-1** HPLC purity trace with an elution time of 4.927 min and 98% purity on method C.

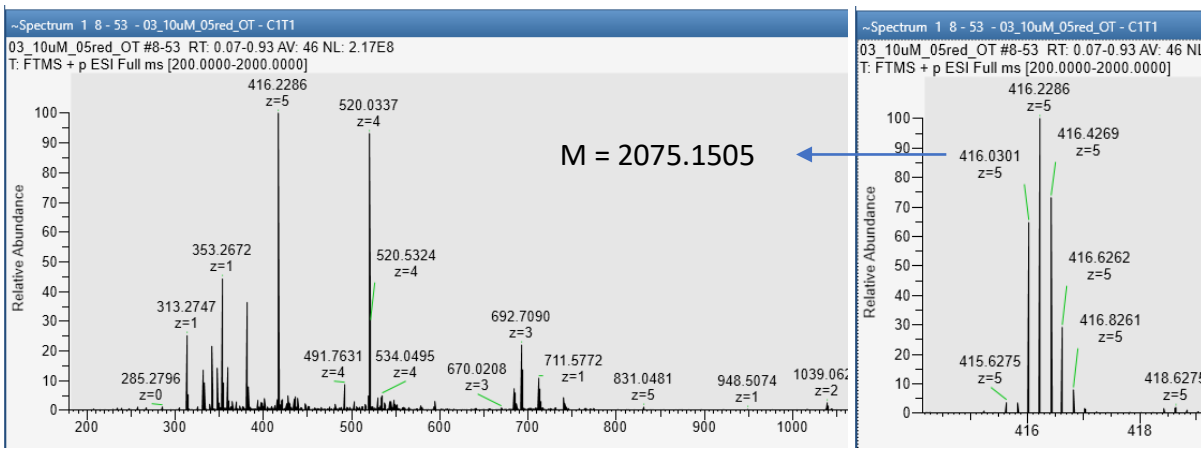

Figure 5-63. HRMS of reduced ***Tr*CART-1** full scan (left) and zoomed (right) with the appropriate mass of 2075.1505 (m/z 416.0301, z=5).

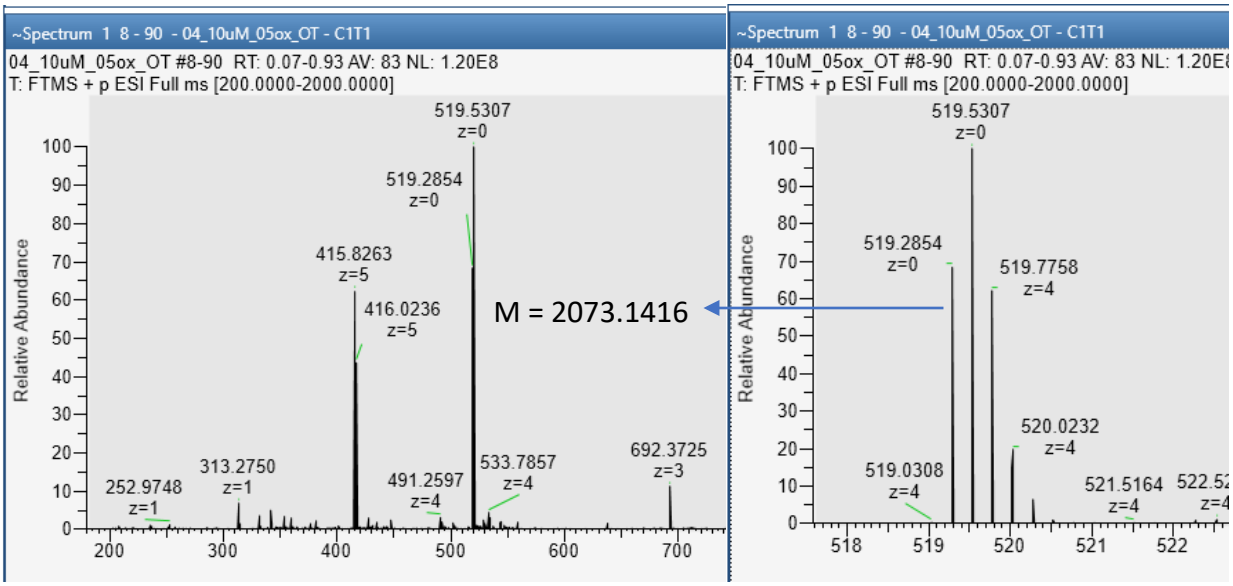

Figure 5-64. HRMS of oxidized ***Tr*CART-1** via Cbi (1hr) full scan (left) and zoomed (right) with the appropriate mass of 2073.1416 (m/z 519.2854, z=4).

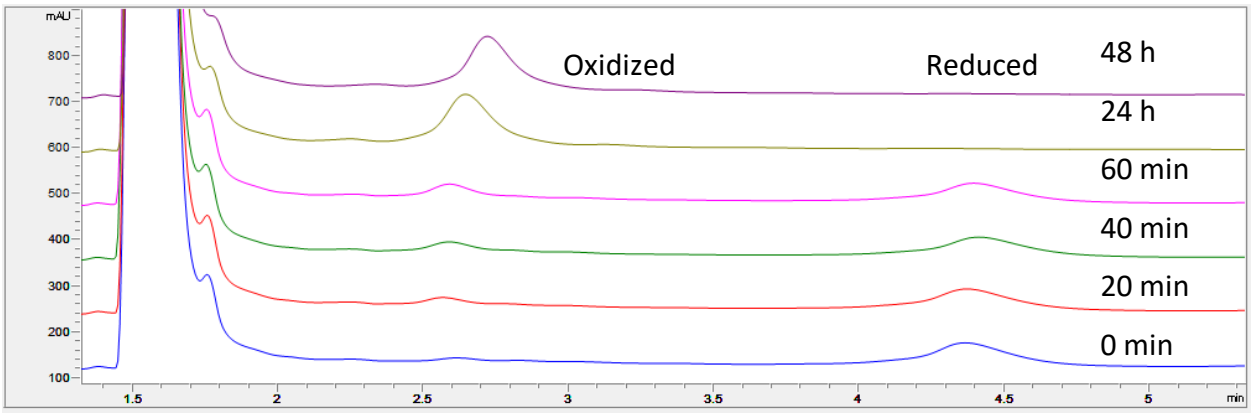

Figure 5-65. HPLC traces of ***Tr*CART-1** in 10% DMSO over 48 hours showing complete oxidation after 24 hours on method C.

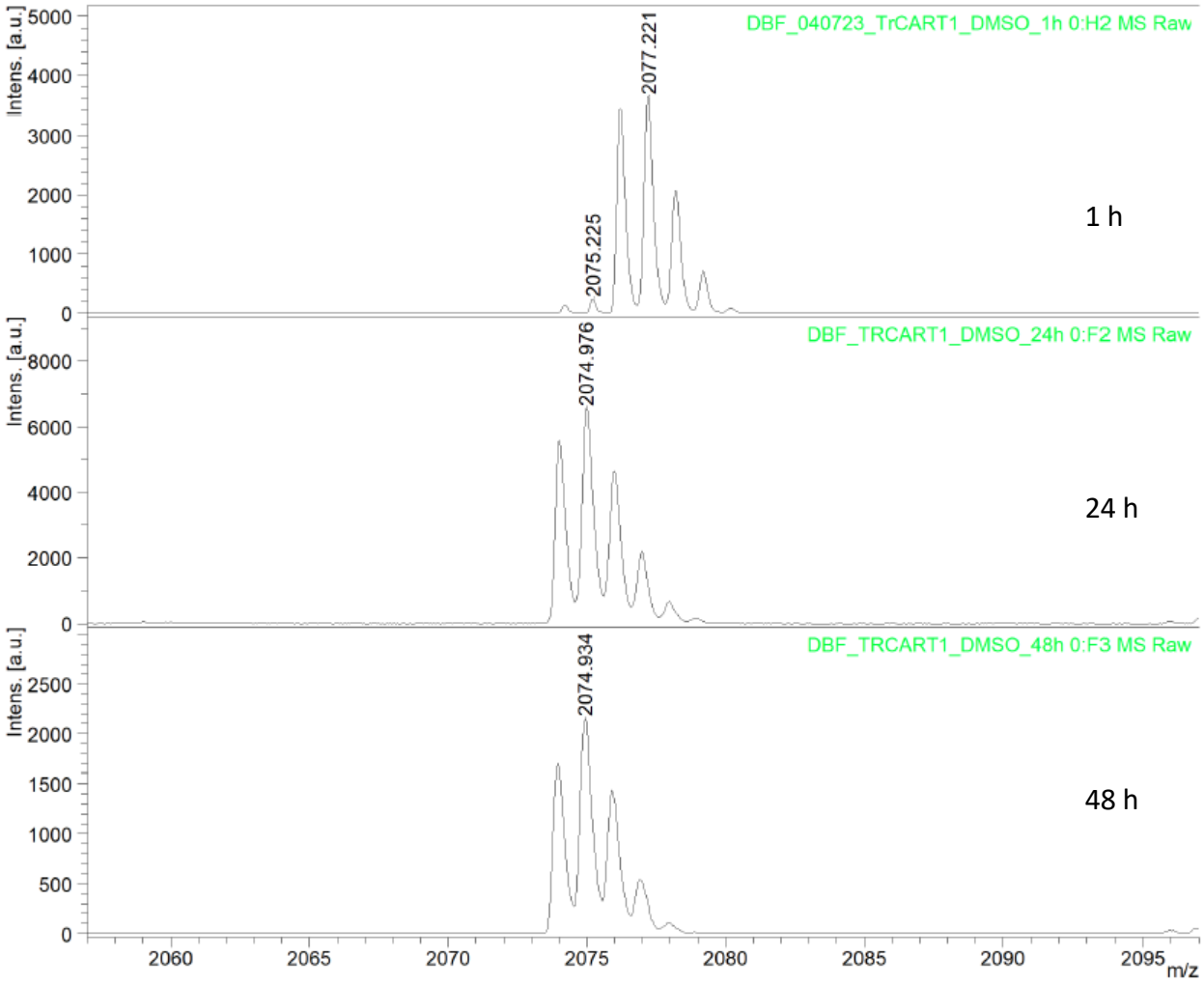

Figure 5-66. MALDI-ToF MS traces of ***Tr*CART-1** in 10% DMSO over 48 hours showing complete oxidation after 24 hours.

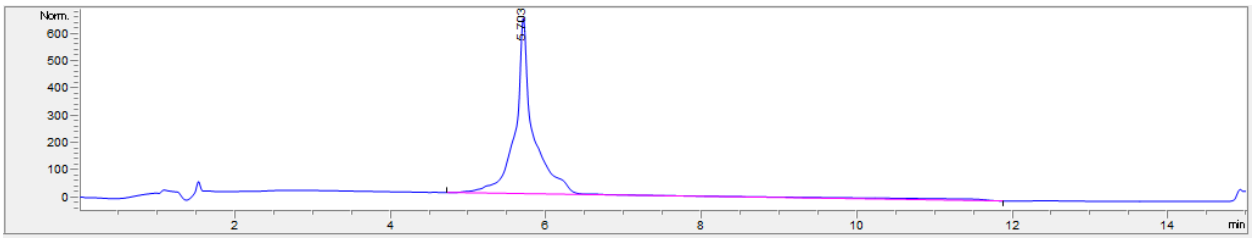

Figure 5-67. HPLC purity trace of ***Tr*CART-2** with an elution time of 5.703 min on method C.

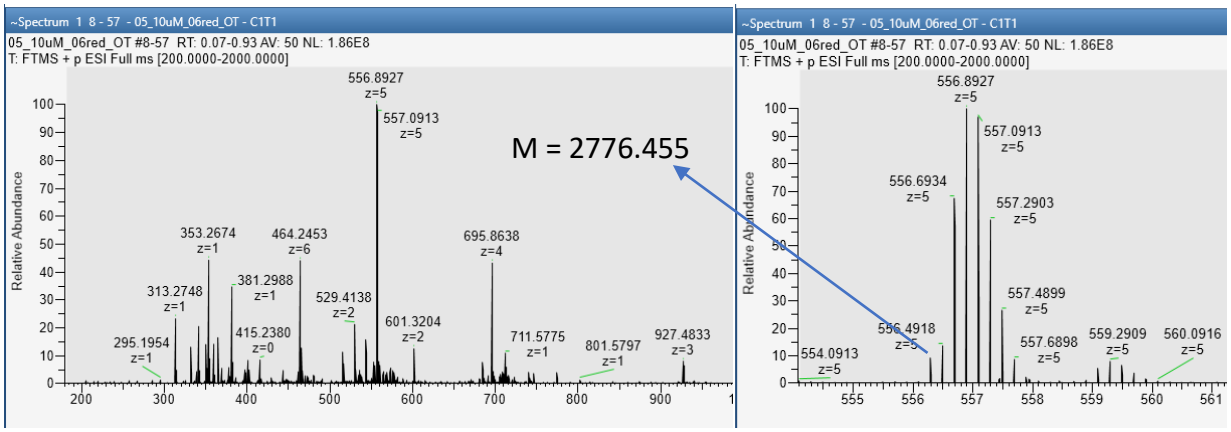

Figure 5-68. HRMS of reduced ***Tr*CART-2** full scan (left) and zoomed (right) with the appropriate mass of 2077.6455 (m/z 556.2910, z=5).

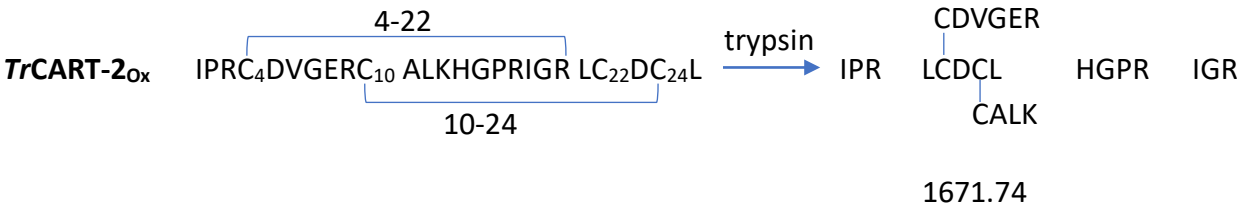

Figure 5-69. Predicted disulfide linkages and trypsin fragments of ***Tr*CART-2**.

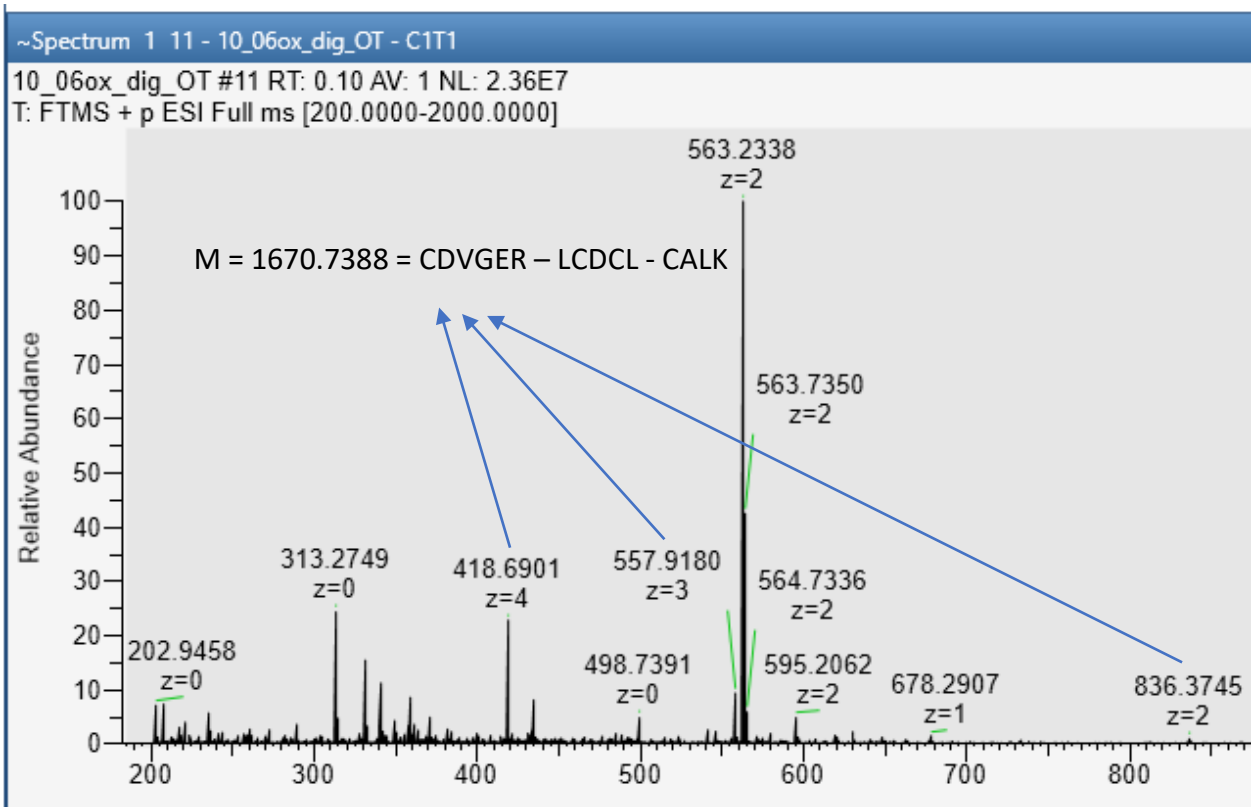

Figure 5-70. HRMS of Cbi oxidized and digested ***Tr*CART-2** showing the detection of ionized trypsin fragments. The smaller fragments were not observed.

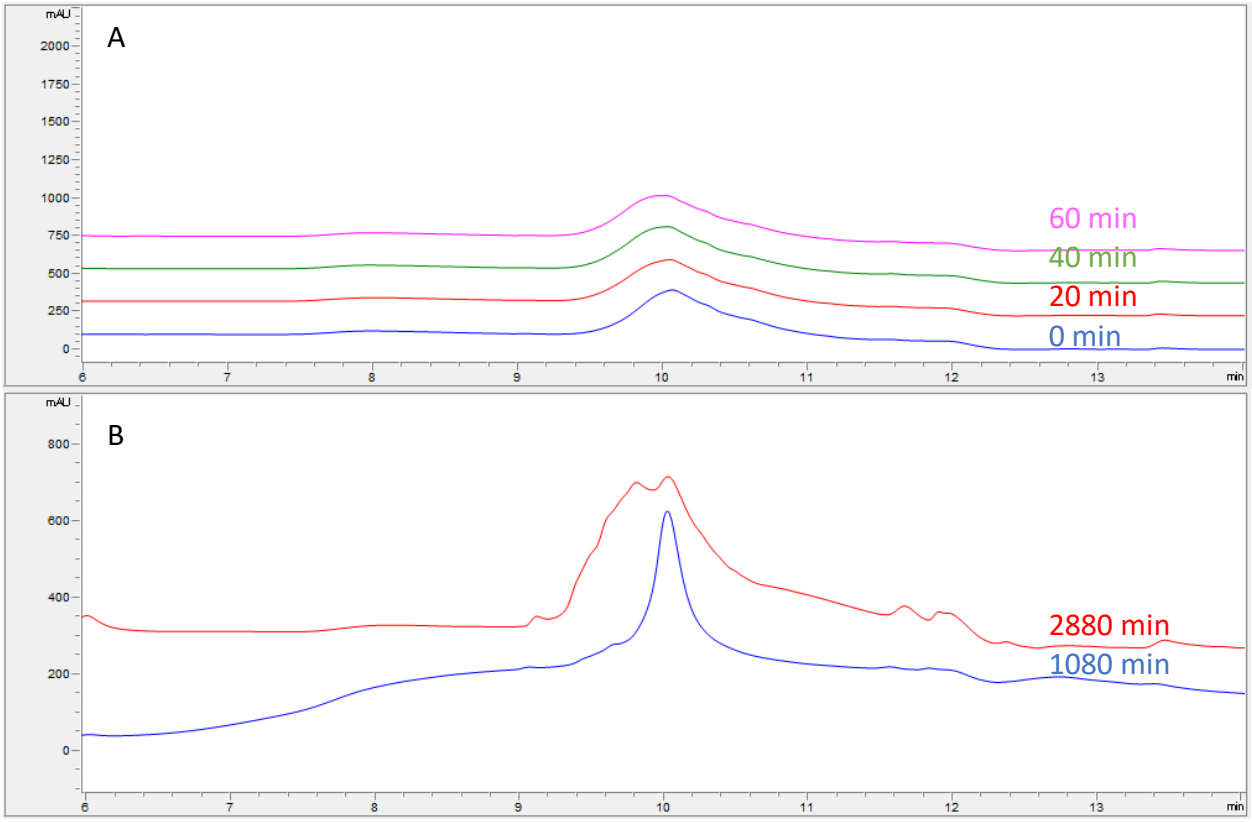

Figure 5-71. HPLC traces of ***Tr*CART-3** reacted with DMSO over the course of (A) 1 hour and (B) 46 hours. From 1 to 18 hours, no change in retention time was observed. At 48 hours, the HPLC profile was observed to change, however mixed products are suggested on method C.

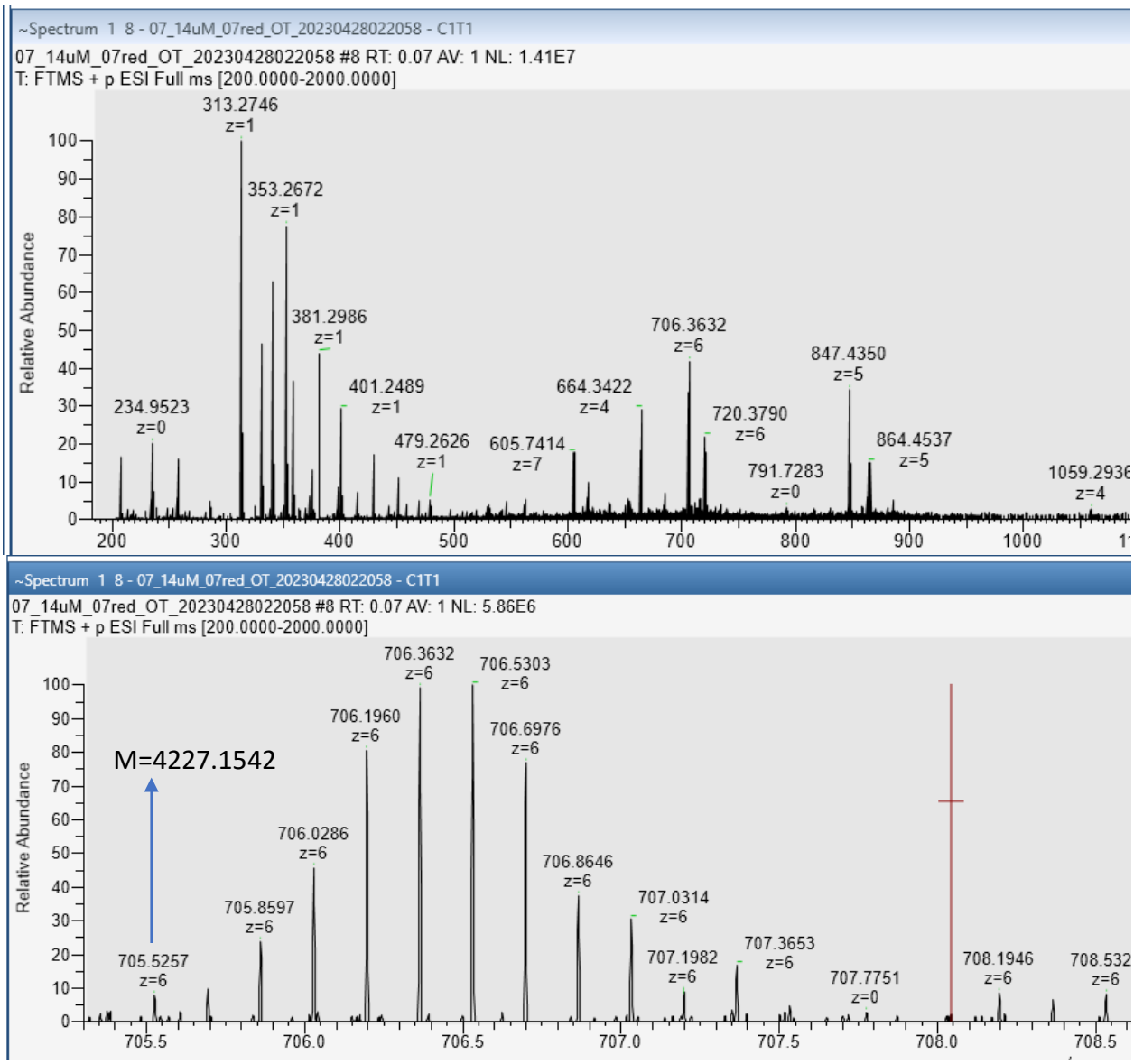

Figure 5-72. HRMS of reduced ***Tr*CART-3** full scan (top) and zoomed (bottom) with the appropriate mass of 4227.1542 (m/z 705.5257, z=6).

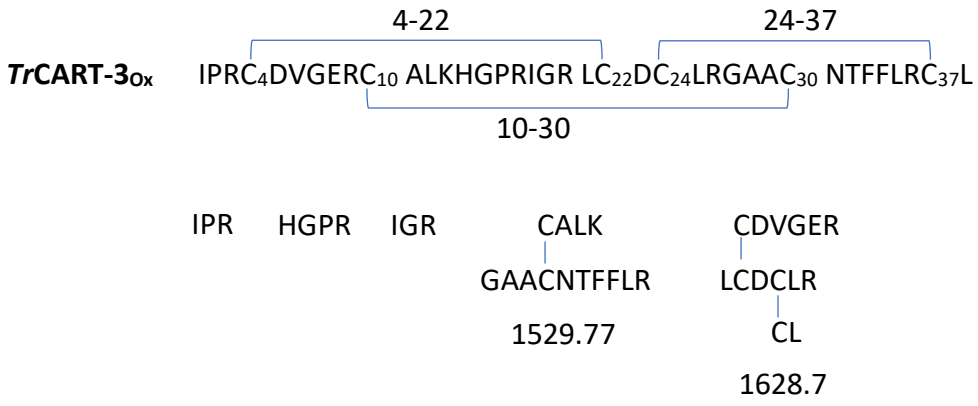

Figure 5-73. Predicted disulfide linkages and trypsin fragments of ***Tr*CART-3**.

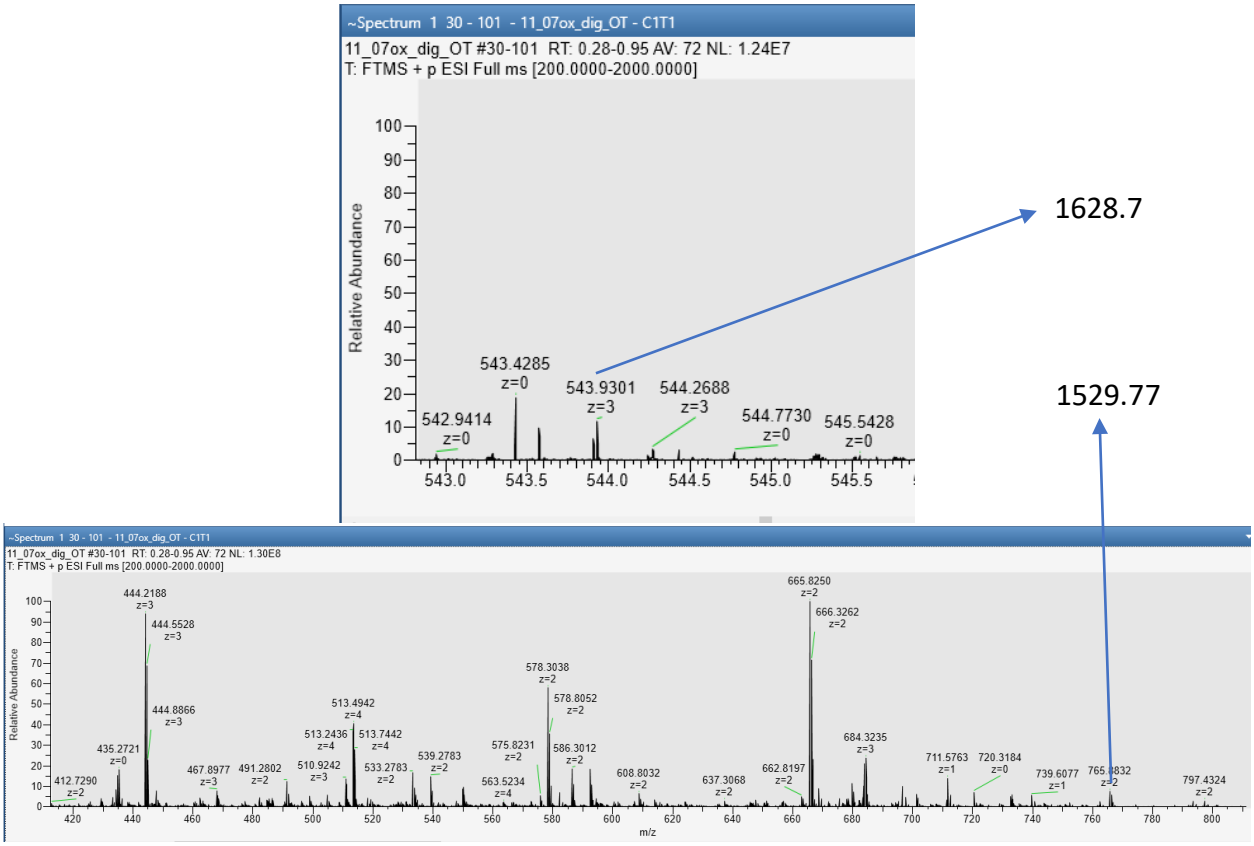

Figure 5-74. HRMS of Cbi oxidized and digested ***Tr*CART-3** showing the detection of ionized trypsin fragments. The Smaller fragments were not observed.

5.4 References

(112) Yarnell, J. E.; McCusker, C. E.; Leeds, A. J.; Breaux, J. M.; Castellano, F. N. Exposing the Excited-State Equilibrium in an Ir III Bichromophore: A Combined Time Resolved Spectroscopy and Computational Study. *Eur. J. Inorg. Chem.* **2016**, *2016* (12), 1808–1818. https://doi.org/10.1002/ejic.201600194.

(113) Yarnell, J. E.; Wells, K. A.; Palmer, J. R.; Breaux, J. M.; Castellano, F. N. Excited-State Triplet Equilibria in a Series of Re(I)-Naphthalimide Bichromophores. *J. Phys. Chem. B* **2019**, *123* (35), 7611–7627. https://doi.org/10.1021/acs.jpcb.9b05688.

(114) Kitchen, J. A.; Martinho, P. N.; Morgan, G. G.; Gunnlaugsson, T. Synthesis, Crystal Structure and EPR Spectroscopic Analysis of Novel Copper Complexes Formed from N-Pyridyl-4-Nitro-1,8-Naphthalimide Ligands. *J. Chem. Soc. Dalt. Trans.* **2014**, *43* (17), 6468–6479. https://doi.org/10.1039/c3dt53323a.

(115) Cotton, F. A.; Daniels, L. M. The Structure of Rhenium Pentacarbonyl Chloride, Re(CO)5Cl. *Acta Crystallogr. Sect. C Cryst. Struct. Commun.* **1983**, *39* (11), 1495–1496. https://doi.org/10.1107/S0108270183009014.

(116) Haddad, S. F.; Marshall, J. A.; Crosby, G. A.; Twamley, B. Fac -Tricarbonylchloro(1,10-Phenanthroline)Rhenium(I). *Acta Crystallogr. Sect. E Struct. Reports Online* **2002**, *58* (10), m559–m561. https://doi.org/10.1107/S1600536802016379.

(117) Meister, A. Glutathione Metabolism and Its Selective Modification. *J. Biol. Chem.* **1988**, *263* (33), 17205–17208. https://doi.org/10.1016/S0021-9258(19)77815-6.

(118) *CrysAlisPro*, version 171.41.94a; Rigaku Corporation: Oxford, UK, 2021.

(119) Sheldrick, G. M. *SHELXT*. *Acta. Crystallogr.* **2015**, *A71* (version 2018/2), 3–8.

(120) Sheldrick, G. M. *SHELXT*. *Acta. Crystallogr.* **2015**, *C71* (version 2018/3), 3–8.

(121) Case, D. R.; Spear, A.; Henwood, A. F.; Nanao, M.; Dampf, S.; Korter, T. M.; Gunnlaugsson, T.; Zubieta, J.; Doyle, R. P. [Re(CO) 3 (5-PAN)Cl], a Rhenium(i) Naphthalimide Complex for the Visible Light Photocatalytic Reduction of CO 2. *Dalt. Trans.* **2021**, *50* (10), 3479–3486. https://doi.org/10.1039/D0DT04116E.

(122) Groom, C. R.; Bruno, I. J.; Lightfoot, M. P.; Ward, S. C. *Crystallogr.* **2016**, *B72*, 171–179.

(123) Dolomanov, O. V.; Bourhis, L. J.; Gildea, R. J.; Howard, J. A. K.; Puschmann, H. *J. Appl. Cryst.* **2009**, *42* (version 1.3-ac4), 339–341.

Chapter 6. Appendix

Appendix A

X-ray crystallography data collection

A crystal (0.149 x 0.05 x 0.041 mm^3) was placed onto a thin glass optical fiber or a nylon loop and mounted on a Rigaku XtaLAB Synergy-S Dualflex diffractometer equipped with a HyPix-6000HE HPC area detector for data collection at 100.00(10) K. A preliminary set of cell constants and an orientation matrix were calculated from a small sampling of reflections.[118] A short pre-experiment was run, from which an optimal data collection strategy was determined. The full data collection was carried out using a Photon Jet (Cu) X-ray source with frame times of 0.07 and 0.30 seconds and a detector distance of 31.2 mm. Series of frames were collected in 0.50º steps in w at different *2q, k*, and *f* settings. After the intensity data were corrected for absorption, the final cell constants were calculated from the *xyz* centroids of 29783 strong reflections from the actual data collection after integration.[118] See **Table 6-1** for additional crystal and refinement information.

Structure solution and refinement

The structure was solved using SHELXT[119] and refined using SHELXL[120]. The space group *P*-1 was determined based on intensity statistics. Most or all non-hydrogen atoms were assigned from the solution. Full-matrix least squares / difference Fourier cycles were performed which located any remaining non-hydrogen atoms. All non-hydrogen atoms were refined with anisotropic displacement parameters. All hydrogen atoms were placed in ideal positions and

refined as riding atoms with relative isotropic displacement parameters. The final full matrix least squares refinement converged to $R1$ = 0.0488 (F^2, $I > 2s(I)$) and w$R2$ = 0.1249 (F^2, all data).

Structure description of [Re(CO)$_3$(1-(1,10)phenanthroline-5-(4-nitro-naphthalimide))X] (X=Cl or Br)

The asymmetric unit contains one Re complex and one toluene solvate molecule in general positions. The halido ligand site is modeled as a disorder of Br:Cl, 0.80:0.20. This disorder is due to combined batches of [Re(CO)$_3$(5-PAN)Cl] and [Re(CO)$_3$(5-PAN)Br] having been made with the starting materials Re(CO)$_5$Cl[121] or Re(CO)$_5$Br. Carbonyl ligand C3-O3, which is *trans* to the halido ligand site, is likely disordered with the halido ligand site, based on the appearance of the ellipsoids and the short C-O distance; however, this disorder was unable to be modeled due to the very small mass of its minor component. The Re-Br and Re-Cl distances were restrained toward the average values obtained from the Cambridge Structural Database[122] for terminal ligands on six coordinate Re centers. The toluene solvate molecule was modeled as disordered over two positions (0.52:0.48).

Structure manipulation and figure generation were performed using Olex2[123]. Unless noted otherwise all structural diagrams containing anisotropic displacement ellipsoids are drawn at the 50 % probability level.

Data collection, structure solution, and structure refinement were conducted at the X-ray Crystallographic Facility, B04 Hutchison Hall, Department of Chemistry, University of Rochester. The instrument was purchased with funding from NSF MRI program grant CHE-1725028.

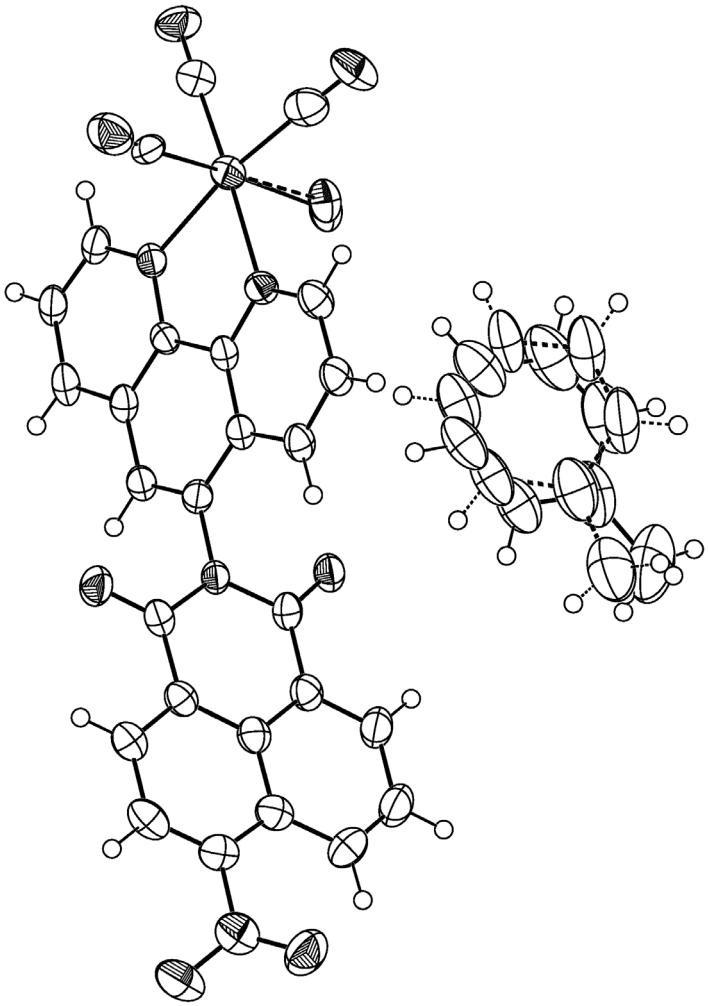

Figure 6-1. ORTEP diagram of mixed [$Re(CO)_3$(1-(1,10)phenanthroline-5-(4-nitro-naphthalimide))X] (X=Cl or Br) and a toluene molecule disordered over two positions (0.52:0.48). Anisotropic displacement ellipsoids are drawn at the 50 % probability level.

Table 6-1. Crystal data and structure refinement for syras01.

Identification code	syras01	
Empirical formula	C34 H20 Br0.80 Cl0.20 N4 O7 Re	
Formula weight	853.53	
Temperature	100.00(10) K	
Wavelength	1.54184 Å	
Crystal system	triclinic	
Space group	*P*-1	
Unit cell dimensions	*a* = 8.4778(2) Å	a = 107.983(2)°
	b = 13.3551(2) Å	b = 95.125(2)°
	c = 13.9955(3) Å	g = 96.9490(10)°
Volume	1482.59(5) $Å^3$	
Z	2	
Density (calculated)	1.912 Mg/m^3	
Absorption coefficient	9.949 mm^{-1}	
F(000)	829	
Crystal color, morphology	yellow, needle	
Crystal size	0.149 x 0.05 x 0.041 mm^3	
Theta range for data collection	3.350 to 77.951°	
Index ranges	-10 £ *h* £ 10, -16 £ *k* £ 16, -17 £ *l* £ 17	
Reflections collected	50161	
Independent reflections	6228 [*R*(int) = 0.0678]	
Observed reflections	5962	
Completeness to theta = 74.504°	99.8%	
Absorption correction	Multi-scan	
Max. and min. transmission	1.00000 and 0.54834	
Refinement method	Full-matrix least-squares on F^2	
Data / restraints / parameters	6228 / 202 / 494	
Goodness-of-fit on F^2	1.118	
Final *R* indices [*I*>2sigma(*I*)]	*R*1 = 0.0488, *wR*2 = 0.1235	
R indices (all data)	*R*1 = 0.0507, *wR*2 = 0.1249	
Largest diff. peak and hole	1.673 and -2.216 e.$Å^{-3}$	

Table 6-2. Atomic coordinates (x 10^4) and equivalent isotropic displacement parameters ($Å^2$x 10^3) for syras01. U_{eq} is defined as one third of the trace of the orthogonalized U_{ij} tensor.

	x	y	z	U_{eq}
Re1	3060(1)	2897(1)	6356(1)	36(1)
O1	3161(7)	5250(4)	7604(4)	58(1)
O2	257(6)	2321(5)	7419(4)	54(1)
O3	5449(7)	2675(5)	7973(5)	59(1)
O4	8985(6)	479(4)	3142(4)	48(1)
O5	5572(5)	2101(3)	1662(3)	37(1)
O6	13931(7)	456(4)	-528(5)	60(1)
O7	13365(7)	1984(5)	-563(5)	66(2)
N1	3090(6)	1315(4)	5288(4)	32(1)
N2	4876(6)	3144(4)	5412(4)	32(1)
N3	7322(5)	1354(4)	2444(4)	29(1)
N4	13160(7)	1206(5)	-271(5)	51(1)
C1	3126(8)	4373(6)	7151(6)	48(2)
C2	1306(9)	2533(6)	7040(5)	46(2)
C3	4730(9)	2747(5)	7434(5)	38(1)
C4	2190(7)	406(5)	5255(5)	35(1)
C5	2225(7)	-560(5)	4508(5)	38(1)
C6	3228(7)	-601(5)	3787(5)	38(1)
C7	4205(7)	338(4)	3799(5)	32(1)
C8	5296(7)	377(4)	3091(5)	32(1)
C9	6212(7)	1314(4)	3159(4)	31(1)
C10	6126(7)	2292(4)	3944(4)	30(1)
C11	7041(7)	3282(4)	4046(5)	34(1)
C12	6860(7)	4158(5)	4823(5)	39(1)
C13	5771(7)	4063(5)	5496(5)	39(1)
C14	5051(7)	2267(4)	4641(4)	29(1)
C15	4084(6)	1279(4)	4577(4)	29(1)
C16	8734(7)	913(4)	2510(5)	34(1)
C17	9848(7)	1003(4)	1785(5)	32(1)

C18	9476(7)	1474(4)	1032(5)	35(1)
C19	7986(7)	1861(5)	966(5)	35(1)
C20	6851(7)	1796(4)	1688(5)	33(1)
C21	11257(7)	598(5)	1819(5)	39(1)
C22	12326(7)	658(5)	1123(5)	43(2)
C23	11981(7)	1134(5)	425(5)	39(1)
C24	10542(7)	1553(5)	337(5)	38(1)
C25	10067(9)	2004(6)	-436(5)	47(2)
C26	8617(9)	2348(6)	-484(6)	49(2)
C27	7579(8)	2289(5)	222(5)	43(1)
Br1	987(4)	3007(2)	4910(2)	40(1)
Cl1	1110(40)	3110(30)	5080(20)	40(1)
C28	2370(40)	4851(19)	60(20)	132(10)
C29	2090(20)	4541(13)	1000(20)	82(5)
C30	790(30)	4805(18)	1540(20)	106(7)
C31	610(30)	4510(20)	2380(20)	96(5)
C32	1620(20)	3937(17)	2720(20)	73(5)
C33	2890(30)	3686(15)	2210(19)	63(5)
C34	3160(30)	3983(17)	1372(19)	67(4)
C28'	3540(30)	4781(18)	490(20)	121(10)
C29'	2710(20)	4621(12)	1328(19)	76(5)
C30'	1560(20)	5259(15)	1766(17)	89(6)
C31'	850(20)	5090(16)	2537(18)	81(5)
C32'	1150(20)	4285(12)	2882(19)	66(4)
C33'	2250(30)	3667(15)	2525(17)	65(5)
C34'	3020(30)	3816(17)	1758(19)	70(5)

Table 6-3. Bond lengths [Å] and angles [°] for syras01.

Re(1)-N(1)	2.184(5)	C(10)-C(11)	1.409(7)
Re(1)-N(2)	2.175(5)	C(10)-C(14)	1.399(8)
Re(1)-C(1)	1.933(8)	C(11)-H(11)	0.9500
Re(1)-C(2)	1.932(7)	C(11)-C(12)	1.365(9)
Re(1)-C(3)	2.048(8)	C(12)-H(12)	0.9500
Re(1)-Br(1)	2.6107(18)	C(12)-C(13)	1.398(9)
Re(1)-Cl(1)	2.427(17)	C(13)-H(13)	0.9500
O(1)-C(1)	1.142(9)	C(14)-C(15)	1.439(7)
O(2)-C(2)	1.127(8)	C(16)-C(17)	1.468(8)
O(3)-C(3)	0.963(8)	C(17)-C(18)	1.415(9)
O(4)-C(16)	1.216(7)	C(17)-C(21)	1.372(8)
O(5)-C(20)	1.205(7)	C(18)-C(19)	1.428(9)
O(6)-N(4)	1.240(8)	C(18)-C(24)	1.404(9)
O(7)-N(4)	1.227(8)	C(19)-C(20)	1.470(8)
N(1)-C(4)	1.339(7)	C(19)-C(27)	1.373(9)
N(1)-C(15)	1.354(7)	C(21)-H(21)	0.9500
N(2)-C(13)	1.329(8)	C(21)-C(22)	1.401(9)
N(2)-C(14)	1.360(7)	C(22)-H(22)	0.9500
N(3)-C(9)	1.443(7)	C(22)-C(23)	1.350(10)
N(3)-C(16)	1.404(7)	C(23)-C(24)	1.413(9)
N(3)-C(20)	1.412(7)	C(24)-C(25)	1.442(10)
N(4)-C(23)	1.472(9)	C(25)-H(25)	0.9500
C(4)-H(4)	0.9500	C(25)-C(26)	1.367(10)
C(4)-C(5)	1.392(9)	C(26)-H(26)	0.9500
C(5)-H(5)	0.9500	C(26)-C(27)	1.394(10)
C(5)-C(6)	1.370(9)	C(27)-H(27)	0.9500
C(6)-H(6)	0.9500	C(28)-H(28A)	0.9800
C(6)-C(7)	1.411(8)	C(28)-H(28B)	0.9800
C(7)-C(8)	1.423(8)	C(28)-H(28C)	0.9800
C(7)-C(15)	1.407(8)	C(28)-C(29)	1.53(4)
C(8)-H(8)	0.9500	C(29)-C(30)	1.41(3)
C(8)-C(9)	1.362(8)	C(29)-C(34)	1.40(2)
C(9)-C(10)	1.439(8)	C(30)-H(30)	0.9500

C(30)-C(31)	1.37(3)	C(2)-Re(1)-C(3)	92.2(3)
C(31)-H(31)	0.9500	C(2)-Re(1)-Br(1)	89.3(2)
C(31)-C(32)	1.36(3)	C(2)-Re(1)-Cl(1)	88.6(10)
C(32)-H(32)	0.9500	C(3)-Re(1)-N(1)	94.5(2)
C(32)-C(33)	1.37(3)	C(3)-Re(1)-N(2)	92.2(2)
C(33)-H(33)	0.9500	C(3)-Re(1)-Br(1)	176.92(18)
C(33)-C(34)	1.38(3)	C(3)-Re(1)-Cl(1)	178.8(9)
C(34)-H(34)	0.9500	C(4)-N(1)-Re(1)	126.3(4)
C(28')-H(28D)	0.9800	C(4)-N(1)-C(15)	118.2(5)
C(28')-H(28E)	0.9800	C(15)-N(1)-Re(1)	115.4(4)
C(28')-H(28F)	0.9800	C(13)-N(2)-Re(1)	126.5(4)
C(28')-C(29')	1.48(4)	C(13)-N(2)-C(14)	117.9(5)
C(29')-C(30')	1.42(2)	C(14)-N(2)-Re(1)	115.6(4)
C(29')-C(34')	1.42(2)	C(16)-N(3)-C(9)	118.8(5)
C(30')-H(30')	0.9500	C(16)-N(3)-C(20)	124.8(5)
C(30')-C(31')	1.35(3)	C(20)-N(3)-C(9)	116.3(5)
C(31')-H(31')	0.9500	O(6)-N(4)-C(23)	116.7(6)
C(31')-C(32')	1.35(2)	O(7)-N(4)-O(6)	122.7(7)
C(32')-H(32')	0.9500	O(7)-N(4)-C(23)	120.6(6)
C(32')-C(33')	1.35(2)	O(1)-C(1)-Re(1)	178.7(7)
C(33')-H(33')	0.9500	O(2)-C(2)-Re(1)	178.2(7)
C(33')-C(34')	1.36(3)	O(3)-C(3)-Re(1)	175.5(7)
C(34')-H(34')	0.9500	N(1)-C(4)-H(4)	118.9
N(1)-Re(1)-Br(1)	82.57(14)	N(1)-C(4)-C(5)	122.3(6)
N(1)-Re(1)-Cl(1)	86.2(8)	C(5)-C(4)-H(4)	118.9
N(2)-Re(1)-N(1)	75.28(18)	C(4)-C(5)-H(5)	120.1
N(2)-Re(1)-Br(1)	86.00(16)	C(6)-C(5)-C(4)	119.8(5)
N(2)-Re(1)-Cl(1)	87.1(10)	C(6)-C(5)-H(5)	120.1
C(1)-Re(1)-N(1)	171.9(2)	C(5)-C(6)-H(6)	120.1
C(1)-Re(1)-N(2)	97.6(2)	C(5)-C(6)-C(7)	119.7(6)
C(1)-Re(1)-C(3)	89.6(3)	C(7)-C(6)-H(6)	120.1
C(1)-Re(1)-Br(1)	93.1(2)	C(6)-C(7)-C(8)	124.0(6)
C(1)-Re(1)-Cl(1)	89.5(8)	C(15)-C(7)-C(6)	116.7(5)
C(2)-Re(1)-N(1)	98.4(2)	C(15)-C(7)-C(8)	119.3(5)
C(2)-Re(1)-N(2)	172.6(2)	C(7)-C(8)-H(8)	119.7
C(2)-Re(1)-C(1)	88.3(3)	C(9)-C(8)-C(7)	120.6(5)

C(9)-C(8)-H(8)	119.7	N(3)-C(20)-C(19)	116.8(5)
C(8)-C(9)-N(3)	120.7(5)	C(17)-C(21)-H(21)	119.7
C(8)-C(9)-C(10)	121.8(5)	C(17)-C(21)-C(22)	120.6(6)
C(10)-C(9)-N(3)	117.5(5)	C(22)-C(21)-H(21)	119.7
C(11)-C(10)-C(9)	124.1(5)	C(21)-C(22)-H(22)	120.1
C(14)-C(10)-C(9)	118.2(5)	C(23)-C(22)-C(21)	119.7(6)
C(14)-C(10)-C(11)	117.7(5)	C(23)-C(22)-H(22)	120.1
C(10)-C(11)-H(11)	120.6	C(22)-C(23)-N(4)	117.9(6)
C(12)-C(11)-C(10)	118.9(6)	C(22)-C(23)-C(24)	122.7(6)
C(12)-C(11)-H(11)	120.6	C(24)-C(23)-N(4)	119.4(6)
C(11)-C(12)-H(12)	120.0	C(18)-C(24)-C(23)	116.7(6)
C(11)-C(12)-C(13)	119.9(5)	C(18)-C(24)-C(25)	118.3(6)
C(13)-C(12)-H(12)	120.0	C(23)-C(24)-C(25)	124.9(6)
N(2)-C(13)-C(12)	122.7(6)	C(24)-C(25)-H(25)	119.7
N(2)-C(13)-H(13)	118.7	C(26)-C(25)-C(24)	120.5(6)
C(12)-C(13)-H(13)	118.7	C(26)-C(25)-H(25)	119.7
N(2)-C(14)-C(10)	123.0(5)	C(25)-C(26)-H(26)	119.6
N(2)-C(14)-C(15)	116.7(5)	C(25)-C(26)-C(27)	120.9(6)
C(10)-C(14)-C(15)	120.3(5)	C(27)-C(26)-H(26)	119.6
N(1)-C(15)-C(7)	123.3(5)	C(19)-C(27)-C(26)	120.3(6)
N(1)-C(15)-C(14)	116.8(5)	C(19)-C(27)-H(27)	119.9
C(7)-C(15)-C(14)	119.8(5)	C(26)-C(27)-H(27)	119.9
O(4)-C(16)-N(3)	120.2(5)	H(28A)-C(28)-H(28B)	109.5
O(4)-C(16)-C(17)	123.0(5)	H(28A)-C(28)-H(28C)	109.5
N(3)-C(16)-C(17)	116.7(5)	H(28B)-C(28)-H(28C)	109.5
C(18)-C(17)-C(16)	121.2(5)	C(29)-C(28)-H(28A)	109.5
C(21)-C(17)-C(16)	119.5(6)	C(29)-C(28)-H(28B)	109.5
C(21)-C(17)-C(18)	119.2(6)	C(29)-C(28)-H(28C)	109.5
C(17)-C(18)-C(19)	119.7(6)	C(30)-C(29)-C(28)	123(2)
C(24)-C(18)-C(17)	121.0(6)	C(34)-C(29)-C(28)	120(2)
C(24)-C(18)-C(19)	119.3(6)	C(34)-C(29)-C(30)	117(3)
C(18)-C(19)-C(20)	120.6(5)	C(29)-C(30)-H(30)	120.1
C(27)-C(19)-C(18)	120.6(6)	C(31)-C(30)-C(29)	120(2)
C(27)-C(19)-C(20)	118.8(6)	C(31)-C(30)-H(30)	120.1
O(5)-C(20)-N(3)	119.8(5)	C(30)-C(31)-H(31)	118.4
O(5)-C(20)-C(19)	123.4(5)	C(32)-C(31)-C(30)	123(2)

C(32)-C(31)-H(31)	118.4	C(30')-C(29')-C(34')	116(2)
C(31)-C(32)-H(32)	121.3	C(34')-C(29')-C(28')	121.6(17)
C(31)-C(32)-C(33)	117(3)	C(29')-C(30')-H(30')	119.7
C(33)-C(32)-H(32)	121.3	C(31')-C(30')-C(29')	120.7(17)
C(32)-C(33)-H(33)	118.9	C(31')-C(30')-H(30')	119.7
C(32)-C(33)-C(34)	122(2)	C(30')-C(31')-H(31')	119.6
C(34)-C(33)-H(33)	118.9	C(32')-C(31')-C(30')	120.7(18)
C(29)-C(34)-H(34)	119.8	C(32')-C(31')-H(31')	119.6
C(33)-C(34)-C(29)	120(2)	C(31')-C(32')-H(32')	119.1
C(33)-C(34)-H(34)	119.8	C(31')-C(32')-C(33')	122(2)
H(28D)-C(28')-H(28E)	109.5	C(33')-C(32')-H(32')	119.1
H(28D)-C(28')-H(28F)	109.5	C(32')-C(33')-H(33')	120.3
H(28E)-C(28')-H(28F)	109.5	C(32')-C(33')-C(34')	119.5(19)
C(29')-C(28')-H(28D)	109.5	C(34')-C(33')-H(33')	120.3
C(29')-C(28')-H(28E)	109.5	C(29')-C(34')-H(34')	119.3
C(29')-C(28')-H(28F)	109.5	C(33')-C(34')-C(29')	121.4(19)
C(30')-C(29')-C(28')	122.7(17)	C(33')-C(34')-H(34')	119.3

Table 6-4. Anisotropic displacement parameters ($Å^2 x\ 10^3$) for syras01. The anisotropic displacement factor exponent takes the form: $-2p^2[\ h^2\ a^{*2}U_{11} + ... + 2\ h\ k\ a^*\ b^*\ U_{12}]$

	U_{11}	U_{22}	U_{33}	U_{23}	U_{13}	U_{12}
Re1	34(1)	38(1)	40(1)	14(1)	10(1)	11(1)
O1	59(3)	42(3)	65(3)	-1(2)	16(3)	14(2)
O2	45(3)	70(3)	58(3)	30(3)	26(2)	12(2)
O3	47(3)	63(3)	69(4)	20(3)	18(3)	18(3)
O4	46(3)	58(3)	59(3)	37(2)	17(2)	23(2)
O5	36(2)	34(2)	46(2)	18(2)	6(2)	10(2)
O6	53(3)	46(3)	74(4)	3(3)	23(3)	8(2)
O7	60(3)	80(4)	82(4)	52(4)	27(3)	16(3)
N1	33(2)	29(2)	38(3)	14(2)	8(2)	9(2)
N2	29(2)	31(2)	38(3)	12(2)	9(2)	4(2)
N3	29(2)	28(2)	36(2)	15(2)	7(2)	8(2)
N4	43(3)	49(3)	56(4)	11(3)	7(3)	5(3)
C1	36(3)	64(5)	47(4)	19(3)	8(3)	11(3)
C2	52(4)	47(4)	44(4)	16(3)	14(3)	16(3)
C3	60(4)	32(3)	26(3)	11(2)	16(3)	9(3)
C4	28(3)	36(3)	52(3)	28(3)	9(2)	8(2)
C5	32(3)	35(3)	58(4)	28(3)	10(3)	9(2)
C6	35(3)	27(3)	56(4)	19(3)	4(3)	7(2)
C7	28(3)	29(3)	42(3)	17(2)	2(2)	7(2)
C8	33(3)	28(3)	37(3)	13(2)	5(2)	8(2)
C9	30(3)	31(3)	35(3)	15(2)	6(2)	6(2)
C10	30(3)	26(2)	37(3)	13(2)	4(2)	6(2)
C11	30(3)	27(3)	46(3)	14(2)	5(2)	3(2)
C12	39(3)	24(3)	52(4)	11(3)	11(3)	1(2)
C13	36(3)	29(3)	48(3)	8(3)	6(3)	3(2)
C14	30(3)	25(2)	36(3)	12(2)	4(2)	8(2)
C15	29(3)	26(2)	34(3)	11(2)	8(2)	9(2)
C16	33(3)	27(3)	42(3)	12(2)	5(2)	8(2)

C17	29(3)	28(3)	38(3)	8(2)	3(2)	4(2)
C18	39(3)	25(3)	38(3)	7(2)	4(2)	1(2)
C19	35(3)	28(3)	41(3)	11(2)	6(2)	3(2)
C20	35(3)	26(3)	40(3)	14(2)	4(2)	4(2)
C21	35(3)	35(3)	46(3)	10(3)	5(3)	9(2)
C22	27(3)	35(3)	57(4)	4(3)	5(3)	4(2)
C23	35(3)	36(3)	40(3)	7(3)	7(3)	-2(2)
C24	36(3)	33(3)	40(3)	7(2)	8(3)	1(2)
C25	48(4)	49(4)	48(4)	24(3)	11(3)	0(3)
C26	53(4)	49(4)	56(4)	33(3)	12(3)	9(3)
C27	45(3)	41(3)	53(4)	27(3)	10(3)	10(3)
Br1	36(1)	35(1)	50(1)	17(1)	-2(1)	7(1)
Cl1	36(1)	35(1)	50(1)	17(1)	-2(1)	7(1)
C28	180(30)	82(16)	150(20)	67(16)	5(18)	8(19)
C29	74(12)	52(9)	103(13)	13(9)	-23(9)	4(9)
C30	83(14)	73(15)	160(17)	35(14)	2(12)	26(11)
C31	53(9)	72(12)	156(13)	25(11)	10(9)	18(9)
C32	51(11)	44(11)	102(11)	-2(9)	2(8)	3(7)
C33	55(10)	40(8)	77(12)	-5(7)	-8(8)	12(7)
C34	58(8)	39(8)	86(12)	3(7)	-6(8)	4(6)
C28'	150(30)	74(14)	160(20)	50(15)	53(18)	43(16)
C29'	64(10)	45(8)	108(12)	17(8)	-9(8)	4(7)
C30'	75(13)	62(12)	157(16)	66(12)	23(11)	25(9)
C31'	43(8)	62(10)	160(14)	65(11)	16(9)	13(8)
C32'	43(9)	36(8)	119(11)	31(8)	-4(7)	5(6)
C33'	53(12)	39(7)	86(11)	5(8)	-19(7)	6(7)
C34'	67(9)	36(8)	93(14)	2(8)	-7(9)	12(7)

Table 6-5. Hydrogen coordinates (x 10^4) and isotropic displacement parameters (Å^2 x 10^3) for syras01.

	x	y	z	U(eq)
H4	1504	420	5758	42
H5	1556	-1188	4500	45
H6	3266	-1259	3280	46
H8	5387	-256	2566	39
H11	7771	3339	3582	41
H12	7472	4831	4907	46
H13	5667	4681	6035	47
H21	11510	276	2319	47
H22	13290	364	1143	51
H25	10768	2063	-916	56
H26	8312	2630	-1006	58
H27	6586	2547	188	52
H28A	1428	5124	-164	198
H28B	2544	4224	-488	198
H28C	3314	5404	217	198
H30	36	5186	1315	127
H31	-255	4715	2745	115
H32	1446	3721	3298	87
H33	3620	3292	2439	76
H34	4072	3810	1045	80
H28D	2810	4477	-152	181
H28E	4488	4427	439	181
H28F	3864	5546	615	181
H30'	1304	5810	1512	107
H31'	121	5543	2840	97
H32'	565	4149	3390	79
H33'	2488	3132	2809	78
H34'	3788	3373	1502	85

Table 6-6. Torsion angles [°] for syras01.

Re1-N1-C4-C5	176.3(4)	C8-C9-C10-C14	-0.8(8)
Re1-N1-C15-C7	-177.0(4)	C9-N3-C16-O4	2.2(8)
Re1-N1-C15-C14	3.0(6)	C9-N3-C16-C17	-178.2(5)
Re1-N2-C13-C12	-176.8(5)	C9-N3-C20-O5	-0.9(8)
Re1-N2-C14-C10	177.9(4)	C9-N3-C20-C19	178.9(5)
Re1-N2-C14-C15	-3.2(6)	C9-C10-C11-C12	-179.8(6)
O4-C16-C17-C18	177.2(6)	C9-C10-C14-N2	179.9(5)
O4-C16-C17-C21	-1.1(9)	C9-C10-C14-C15	1.0(8)
O6-N4-C23-C22	33.9(9)	C10-C11-C12-C13	-0.5(9)
O6-N4-C23-C24	-145.7(6)	C10-C14-C15-N1	179.1(5)
O7-N4-C23-C22	-145.3(7)	C10-C14-C15-C7	-1.0(8)
O7-N4-C23-C24	35.1(9)	C11-C10-C14-N2	-1.1(8)
N1-C4-C5-C6	1.2(9)	C11-C10-C14-C15	-179.9(5)
N2-C14-C15-N1	0.1(8)	C11-C12-C13-N2	-0.4(10)
N2-C14-C15-C7	-179.9(5)	C13-N2-C14-C10	0.2(9)
N3-C9-C10-C11	0.8(8)	C13-N2-C14-C15	179.1(5)
N3-C9-C10-C14	179.8(5)	C14-N2-C13-C12	0.5(9)
N3-C16-C17-C18	-2.4(8)	C14-C10-C11-C12	1.2(9)
N3-C16-C17-C21	179.3(5)	C15-N1-C4-C5	-1.2(9)
N4-C23-C24-C18	-179.1(5)	C15-C7-C8-C9	-0.3(8)
N4-C23-C24-C25	4.0(9)	C16-N3-C9-C8	-72.7(7)
C4-N1-C15-C7	0.8(8)	C16-N3-C9-C10	106.8(6)
C4-N1-C15-C14	-179.2(5)	C16-N3-C20-O5	175.9(5)
C4-C5-C6-C7	-0.7(9)	C16-N3-C20-C19	-4.4(8)
C5-C6-C7-C8	179.3(6)	C16-C17-C18-C19	-0.7(8)
C5-C6-C7-C15	0.3(8)	C16-C17-C18-C24	-179.7(5)
C6-C7-C8-C9	-179.3(6)	C16-C17-C21-C22	178.9(5)
C6-C7-C15-N1	-0.3(8)	C17-C18-C19-C20	1.4(8)
C6-C7-C15-C14	179.7(5)	C17-C18-C19-C27	-177.9(6)
C7-C8-C9-N3	179.8(5)	C17-C18-C24-C23	0.5(8)
C7-C8-C9-C10	0.4(9)	C17-C18-C24-C25	177.6(6)
C8-C7-C15-N1	-179.5(5)	C17-C21-C22-C23	1.2(9)
C8-C7-C15-C14	0.5(8)	C18-C17-C21-C22	0.5(9)
C8-C9-C10-C11	-179.8(6)	C18-C19-C20-O5	-179.3(6)

C18-C19-C20-N3	0.9(8)	C25-C26-C27-C19	-1.5(11)
C18-C19-C27-C26	0.3(10)	C27-C19-C20-O5	0.0(9)
C18-C24-C25-C26	0.2(10)	C27-C19-C20-N3	-179.7(5)
C19-C18-C24-C23	-178.5(5)	C28-C29-C30-C31	-179.5(10)
C19-C18-C24-C25	-1.4(9)	C28-C29-C34-C33	-178.8(12)
C20-N3-C9-C8	104.3(6)	C29-C30-C31-C32	-2(2)
C20-N3-C9-C10	-76.3(6)	C30-C29-C34-C33	2.0(19)
C20-N3-C16-O4	-174.5(6)	C30-C31-C32-C33	2(3)
C20-N3-C16-C17	5.1(8)	C31-C32-C33-C34	-1(3)
C20-C19-C27-C26	-179.0(6)	C32-C33-C34-C29	-2(3)
C21-C17-C18-C19	177.6(6)	C34-C29-C30-C31	-0.4(14)
C21-C17-C18-C24	-1.4(8)	C28'-C29'-C30'-C31'	-179.5(10)
C21-C22-C23-N4	178.2(6)	C28'-C29'-C34'-C33'	-179.6(12)
C21-C22-C23-C24	-2.2(9)	C29'-C30'-C31'-C32'	-3(2)
C22-C23-C24-C18	1.3(9)	C30'-C29'-C34'-C33'	1.0(18)
C22-C23-C24-C25	-175.6(6)	C30'-C31'-C32'-C33'	5(3)
C23-C24-C25-C26	177.1(7)	C31'-C32'-C33'-C34'	-4(3)
C24-C18-C19-C20	-179.5(5)	C32'-C33'-C34'-C29'	1(2)
C24-C18-C19-C27	1.2(9)	C34'-C29'-C30'-C31'	-0.1(14)
C24-C25-C26-C27	1.2(11)		

Alyssa Spear

ASPEAR01@SYR.EDU |ORCID iD # 0000-0001-6549-8311

Self-motivated and dedicated researcher studying small molecule metal catalysts for CO_2 reduction and oxidative synthesis of peptide disulfide bonds . Experienced in synthetic chemistry, solid-phase peptide synthesis and biochemical characterization.

EDUCATION

Syracuse University, Syracuse, NY 2019-present
PhD. Candidate in Chemistry
Advisors: Professor Robert Doyle, Professor Jon Zubieta

Syracuse University, Syracuse, NY 2021
Master of Philosophy in Chemistry

Baldwin Wallace University, Berea, OH 2015-2019
Bachelor of Science with Honors in Neuroscience and Chemistry,
Summa Cum Laude
Honors Thesis: Synthesis, characterization, and contrast of novel tricarbonyl rhenium (I) octahedral complexes for fluoroscopic esophagography

RESEARCH EXPERIENCE

Graduate Research Assistant, Syracuse University, Syracuse, NY 2019-present

- Conducted primary research in the fields of small molecule transition metal catalysis in CO_2 reduction and peptide disulfide bond formation, Pt(IV) pro-drugs for the study of cisplatin transcriptomics, and the development of peptide drugs for stroke treatment

Research Technician, Syracuse University, Syracuse NY 2019

- Completed a summer position in the lab of Dr. Ivan Korendovych in the field of small peptide catalysis

Undergraduate Research Assistant, Baldwin Wallace University, Berea, OH 2017—2019
Advisor: Dr. Sarah Binkley, Assistant Professor of Chemistry

- Conducted primary research by synthesizing and characterizing rhenium(I)diaqua-tricarbonyl(N-acetyl-*d*-glucosamine)bromide as a contrast agent for applications in the visualization of the GI tract via fluoroscopy

Undergraduate Research Assistant, Baldwin Wallace University, Berea, OH 2016—2017
Advisor: Dr. Clare Mathes, Associate Professor of Psychology

- Assisted in studies of the behavioral pharmacology of gustation; tasks included operating gustometers, chemical preparation, and immunohistochemical preparation and processing of rat brain tissue

SKILLSET

Laboratory
Synthesis and preparation of inorganic molecules, fluorescent compounds and peptides, crystallization, air-free manipulations (Schlenk line), mammalian cell culture, live-cell imaging, confocal laser scanning microscopy, photocatalysis, HPLC, flash chromatography, MALDI-TOF MS, LC-ESI-MS, NMR spectroscopy, FT-IR, GC, UV-vis spectroscopy, fluorescence spectroscopy

Technical
GraphPad Prism, Bruker TopSpin, PyMol, FIJI, ZEN Blue

PUBLICATIONS

- **Spear, A**.; Borner, T.; Tran, S.; Ryan, K.; Najjar, N.R.; Milliken, B.T.; Hayes, M.R.; De Jonghe, B.C.; Doyle, R.P. Synthesis, Characterization, and Imaging of Fluoroplatin: a Pro-drug for Fluorescence Detection of Aquated Cisplatin. *Manuscript in progress* **2023**
- **Spear, A**.; Orativski, O.; Tran, S.; Zubieta, J.A.; Doyle, R.P. Rapid, green peptide disulfide bridge formation in water using dicyanocobinamide. *Submitted* **2023**
- **Spear, A**.; Schuarca, R. L.; Bond, J. Q.; Korter, T. M.; Zubieta, J.; Doyle, R. P. Photocatalytic Turnover of CO_2 under Visible Light by [Re(CO)$_3$(1-(1,10) Phenanthroline-5-(4-Nitro-Naphthalimide))Cl] in Tandem with the Sacrificial Donor BIH. *RSC Adv.* **2022**, *12* (9), 5080–5084. https://doi.org/10.1039/D1RA08261B.
    - **RSC Advances February & March 2022 HOT Article**
- Case, D. R.*; **Spear, A**.*; Henwood, A. F.; Nanao, M.; Dampf, S.; Korter, T. M.; Gunnlaugsson, T.; Zubieta, J.; Doyle, R. P. [Re(CO)$_3$(5-PAN)Cl], a Rhenium(I) Naphthalimide Complex for the Visible Light Photocatalytic Reduction of CO_2. *Dalt. Trans.* **2021**, *50* (10), 3479–3486. https://doi.org/10.1039/D0DT04116E.

* Designates that the authors contributed equally to the project

MEETING PRESENTATIONS

- **Spear, A.**; Zubieta, J.A.; Doyle, R.P. Photocatalytic turnover of CO_2 under visible light by [Re(CO)$_3$(1-(1,10) phenanthroline-5-(4-nitro-naphthalimide))Cl] in tandem with a sacrificial donor, oral and poster presentation, 2022 Fall ACS Meeting and Expo, Chicago, Illinois
- **Spear, A.**; Zubieta, J.A.; Doyle, R.P. Photocatalytic turnover of CO_2 under visible light by [Re(CO)$_3$(1-(1,10) phenanthroline-5-(4-nitro-naphthalimide))Cl] in tandem with a sacrificial

donor, poster presentation, 29th Annual Chemistry Graduate Student Symposium, University of Buffalo, Buffalo, NY

- **Spear, A.**; Binkley, S. Synthesis, characterization, and contrast of novel tricarbonyl rhenium (I) octahedral complexes for fluoroscopic esophagography, poster presentation, 2019 ACS Meeting and Expo, Orlando, Florida
- **Spear, A.***; Bowers, R.*; Garrison, B.*; Hartswick, D.*; Renker, L.*; Sant, E.*; Sluzala, Z.*; Woller, P.*; Mathes, C.M. NRO259: BW Brain Fair – Creating Neural Connections, poster presentation, 2018 Society for Neuroscience National Conference, San Diego, California

* Designates that the authors contributed equally to the project

AWARDS & HONORS

Scholarships and Awards

- CATL-ChemCatBio Graduate Student Travel Award, CATL division of the ACS 2022
- Dept. of Chemistry Graduate Student Travel Award, Syracuse University 2022
- GSO Professional, Academic, and Creative Work Grant, Syracuse University 2022
- Outstanding Senior in Chemistry Award, Baldwin Wallace University 2019
- Outstanding Teaching Assistant Award, Baldwin Wallace University 2019
- Mark Gorman Scholarship, Baldwin Wallace University 2018
- Dr. Sardari L. and Sunita Arora Scholarship, Baldwin Wallace University 2017—2018
- CRC Press Freshmen Chemistry Achievement Award, Baldwin Wallace Uni. 2016
- Chemistry Department Memorial Scholarship, Baldwin Wallace University 2016
- BW Presidential Scholarship, Baldwin Wallace University 2015 – 2019
- Choose Ohio FIRST STEM Scholarship 2015 – 2019
- Ohio College Opportunity Grant 2015—2018

Honors

- Dayton C. Miller Honors Society, Baldwin Wallace University 2017
- Nu Rho Psi inductee, Baldwin Wallace University 2017
- Ratcliffe Student Fellows, Center for Innovation and Growth, Berea, OH 2016—2017

PROFESSIONAL EXPERIENCE AND TEACHING

Symposium Presider

- Invited to preside for the General Catalysis symposium at ACS Fall 2022 2022

Teaching Assistant (TA)

Syracuse University, Syracuse, NY 2022—2023, 2020—2021

- Graduate TA of Metals in Medicine (Spring 2023)
- Graduate TA of Gen. Chemistry Lecture I (Honors/Major)(Fall 2022)
- Graduate TA of Gen. Chemistry Lecture recitations II (Spring 2021)
- Graduate TA of Gen. Chemistry Lab I (Fall 2020)

Baldwin Wallace University, Berea, OH 2016—2019

- TA of General Chemistry Lab I & II (Fall 2016, Spring 2017)
- TA of Organic Chemistry Lab (Fall 2017)
- TA of Inorganic Chemistry Lab (Spring 2018, 2019)
- TA of Quantitative Analysis Lab (Fall 2019)

Chemistry Stockroom Manager 2016 – 2019

- Performed routine lab and chemical stockroom maintenance and up-keep
- Prepared reagents and refined procedures for undergraduate level laboratory courses
- Managed chemical inventory and waste
- Supervised stockroom assistants

Supplemental Instructor/ CLRA Certified Tutor 2016 – 2019

- Provided tutoring services at a CLRA certified program
- Prepared weekly lesson plans and held sessions to aid comprehension of lecture materials
- Collaborated with faculty and students to maximize success in the course

Husbandry Assistant 2016 – 2017

- Provided care for laboratory animals (rats) in accordance with USDA and PHS regulations

FELLOWSHIPS

Chemistry Department Fellowship, Syracuse University 2019-2023